

https://dspace.org/

Search for an A boson decaying to Zh, within the fully hadronic final state, in pp collision data recorded at s = 8 TeV with the ATLAS experiment

Hamity, Guillermo Nicolas

2015-05-21
http://hdl.handle.net/10539/18517

Downloaded from a DSpace repository. https://dspace.org/

Search for an A boson decaying to Zh, within the fully hadronic $\ell\ell\tau\tau$ final state, in pp collision data recorded at $\sqrt{s} = 8$ TeV with the ATLAS experiment



Guillermo Nicolas Hamity

Thesis presented in fulfilment of the requirements for the degree of

Master of Science in Physics

at the University of the Witwatersrand

School of Physics,
University of the Witwatersrand,
PO Box Wits, Johannesburg, 2050, South Africa

Supervised by Prof. Trevor Vickey

May 21, 2015

Abstract

A search for the pseudoscalar A boson, which is predicted by in many models with an extended Higgs sector, gives a gateway to searches for physics beyond the Standard Model (SM). This thesis presents the results of a search for gluon-fusion produced A in the decay to Zh, with a final state of two electrons or muons and two τ leptons, in 20.3 fb^{-1}of proton-proton collision data at $\sqrt{s}$ = 8 TeV. Each tau lepton is allowed to dacay either leptonically, τ_{lep}, or hadronically,τ_{had}, giving rise to three final states, $\tau_{lep}\tau_{lep}$, $\tau_{lep}\tau_{had}$ and $\tau_{had}\tau_{had}$. Focus is placed on the methodology and results of the fully hadronic channel. No evidence for the existence of an A boson is found in the scanned range of $220 \leq m_A \leq 1000$ GeV and 95% CL upper limits are placed on the gluon-fusion cross section times branching ratio, $\sigma \times \mathrm{BR}(A \rightarrow Zh) \times \mathrm{BR}(h \rightarrow \ell\ell\tau\tau)$. The results are combined with a complementing $A \rightarrow Zh$ search, where $h \rightarrow b\bar{b}$, and interpreted in view of two-Higgs-Doublet-Models (2HDMs), where exclusion limits are placed on large sections of phasepace.

Acknowledgements

I would like to acknowledge the generous contributions from the National Research Foundation (NRF) and SA-CERN for providing funding for my studies, as well as making it possible to attend CERN, and various conferences, providing me with an invaluable and rewarding experience. I would also like to acknowledge The University of the Witwatersrand and the Physics department and its staff for providing the facilities to complete this thesis.

I would like to thank the analysis team with which I worked at CERN for incorporating me into a very exciting analysis, as well as providing insight, support and suggestions at every step of my work. I would like to mention in particular Allison McCarn, Pedro De Bruin, Marco Rescigno and Nikolaos Rompotis for their support.

I also thank the past and current members of the Tau Working Group for their support. I make special mention of Attilio Andreazza, Felix Friedrich, Lidija Radovanovic, Michel Janus, Stefania Xella and Will Davey. A special thanks goes to Kieran Bristow for his patience when teaching me the ropes.

I have to extend my gratitude to my college and friend German Carrillo-Montoya. He has responded to an onslaught of questions and correspondence with regards to my work, and this thesis would have not been possible without his dedicated support. I also acknowledge that he prepares the best cheese fondue in all of Geneva.

" At first it will be like trying to drink water from a fire hydrant." a loosely quoted analogy from my supervisor Trevor Vickey at the beginning of my research. A huge thanks is extended to him for his support during my research, in particular for displaying confidence in me and my work, and for allowing me to function quite independently. This gesture continued to inspire resolve. A special thanks for dealing with numerous administrative nuisances when organizing funding and trips abroad, the likes of which I wish upon no human being.

Finally I have to thank my family for their continual support. Monica for going beyond the call of duty by housing her 26 year old son, and my father Guillermo who truly made all of this possible. A special thanks to my partner Giselle for having put up with the uncertainties of 'academic' life, as well as the countless quarter-life crises that come along with it.

Dedicated to my father.

Decleration

I, the undersigned, hereby declare that the work contained in this thesis is my own original work and that I have not previously in its entirety or in part submitted it at any university for a degree.

Signature ..........

Guillermo Nicolas Hamity

Date: May 21, 2015

Contents

1 Introduction **5**
- 1.1 The Standard Model . . . 5
- 1.2 The Higgs mechanism . . . 6
- 1.3 The discovery of a Higgs Boson . . . 7
- 1.4 Looking beyond the Standard Model at two-Higgs-doublet models . . . 8
- 1.5 Motivation for a search of the pseudoscalar Higgs boson . . . 10

2 The ATLAS Experiment **20**
- 2.1 CERN and the Large Hadron Collider . . . 20
- 2.2 The ATLAS detector . . . 21
  - 2.2.1 Magnet System . . . 22
  - 2.2.2 Inner Detector . . . 23
  - 2.2.3 Calorimeters . . . 25
  - 2.2.4 Muon Spectrometer . . . 26
  - 2.2.5 Trigger System . . . 27
  - 2.2.6 Overview of object reconstruction . . . 28
- 2.3 The ATLAS computing model . . . 28
  - 2.3.1 The computing grid . . . 29
  - 2.3.2 The ATHENA framework . . . 30
  - 2.3.3 Simulated data and Monte Carlo production . . . 32
  - 2.3.4 Software development for Run-II . . . 33
  - 2.3.5 Physics Validation . . . 33
- 2.4 Tau lepton reconstruction in ATLAS . . . 34
  - 2.4.1 Tau characteristics . . . 35
  - 2.4.2 Tau reconstruction . . . 35
  - 2.4.3 Tau background discrimination . . . 37
  - 2.4.4 Di-tau mass reconstruction with the Missing Mass Calculator . . . 39

3 Physics validation and tau leptons **40**
- 3.1 Tau validation for ATHENA 17 . . . 41
- 3.2 Tau validation for ATHENA 19 . . . 44
  - 3.2.1 The TauDQA package . . . 44
  - 3.2.2 Truth matching of tau leptons . . . 45
  - 3.2.3 Example validation with ATHENA 19 . . . 46

4 The A $\rightarrow$Zh $\rightarrow \ell\ell\ \tau\tau$ analysis **51**
- 4.1 Monte Carlo and data samples . . . 52
  - 4.1.1 Signal MC samples . . . 52
  - 4.1.2 Background MC samples . . . 53
  - 4.1.3 Data samples . . . 53
- 4.2 Object Selection . . . 53
  - 4.2.1 Electrons . . . 54
  - 4.2.2 Muons . . . 55
  - 4.2.3 Jets . . . 55
  - 4.2.4 Taus . . . 55
  - 4.2.5 Missing transverse energy . . . 55
  - 4.2.6 Di-tau reconstruction . . . 55

4.2.7 Scaled A mass reconstruction 55
4.3 Event pre-selection 56
4.4 Event Selection 57
4.5 Optimization Study 59
4.6 Data-driven background predictions 62
4.7 Systematic uncertainties 67
4.7.1 Experimental and theoretical MC systematics 67
4.7.2 Data-driven systematics 70
4.8 Results 71

5 Conclusions **79**

1 Introduction

1.1 The Standard Model

The Standard Model (SM) is a quantum field theory which explains the fundamental constituents of matter and their respective interactions, described extensively in Reference [1]. The SM entails electromagnetic (EM), weak and strong interactions of subatomic particles. It is based on a local symmetry group $SU_3^C \times SU_2^L \times U_1^{Y^2}$, where C, L and Y correspond to the quantum numbers: colour, weak-isospin and weak-hypercharge, corresponding to the strong, and electromagnetic interactions, respectively. Although it is not a complete theory of fundamental interactions, since it does not incorporate the full theory of gravitation, it provides the most complete understanding of fundamental sub-atomic particles to date.

In the SM the fundamental particles are classified as either half-spin (fermions) or integer-spin (bosons) particles. The first category, the fermions, consists of 12 distinct elementary particles of spin $\frac{1}{2}$. Fermions are the constituents of matter in the universe and are further divided into two sets of particles, quarks and leptons. The quarks are characterized into six different flavours: up (u), down (d), charm (c), strange (s), top (t) and bottom (b). Each quark is attributed with a set of quantum numbers: charge (either $\frac{2}{3}$ or $-\frac{1}{3}$), weak-isospin, weak-hypercharge and a quantum number associated with the strong interaction, colour (red, green or blue or their anti-counterparts). The quarks experience strong and electroweak interactions since they have colour, charge and weak isospin. The colour charges allows for the existence of compound groups of quarks, known as hadrons, which may have the same quantum numbers and which are otherwise impossible due to the Pauli exclusion principle. The quarks will always form sets of colour neutral combinations. Quarks therefore cannot exist in isolation and are always found in these colour-neutral hadrons. The quarks exist in hadrons of quark anti-quark pairs (mesons) or three quark groups (baryons).

The remaining six fermions are called leptons. They consist of -1 charge and neutral particles and are divided into three generations, corresponding to particles in different generations having similar properties, but different mass. The first generation consists of the the -1 charge electron (e) and it's respective neutral partner, the electron neutrino (ν_e). The second generation is comprised of the muon (μ) and muon neutrino (ν_μ), and the third generation of the tau (τ) and tau neutrino (ν_τ). Leptons do not contain colour and are therefore exempt from undergoing strong interactions. They have quantum numbers associated with weak-hypercharge and weak-isospin. Although all leptons undergo weak interactions, the neutrinos are neutral and do not experience EM interactions. Neutrinos have tiny masses and where assumed to be massless until recently. Each lepton has a corresponding anti-particle, with identical mass and spin, but inverted internal quantum numbers. These are the positron, anti-muon and anti-tau, and it is not yet know if the neutrino is it's own anti particle.

Interactions between fermions occur through the exchange of bosons, known as a mediation. The bosons carry integer-spin and are the propagators of the fundamental forces in the SM. These are described by three forces: EM, weak and strong forces. The strong force is responsible for quark-quark, and subsequently inter-nuclear interactions. The most familiar boson is the massless photon (γ) which dictates EM interactions and corresponds to the gauge group $U_1^{Y^2}$. The interactions between fermions via the exchange of photons is understood by a quantum field theory known as Quantum Electrodynamics (QED). Predictions of QED agree with experiment with an accuracy of $\approx 10^{-12}$ [2], making it an extremely accurate theory. The weak force, which is responsible for beta decay, is carried by the massive Z^0 and $W^\pm$ particles, the latter being charged and therefore also interacting electromagnetically. These three bosons correspond to the gauge group SU_2^L (2^2-1 gauge generators). The EM and weak forces where unified by Glashow, Salam, and Weinberg into an electroweak theory of particle interactions, laying a foundation

for unified theories [3]. The strong force is described by the quantum field theory of Quantum Chromodynamics (QCD). There are eight massless coloured bosons ($3^2 - 1$) which couple to the SU_2^C colour charge. The strong force bosons are referred to as gluons, so named due to their role in the binding of hadrons. The eight gluons are denoted as g_i, where $i = 1, ..., 8$. The gluons are massless, but unlike the photon, their effects are only felt in the limited ranges inside a hadron.

The three gauge theories, QCD, QED and electroweak theory, which comprise the SM are required to have gauge invariance. Preserving this symmetry requires the gauge bosons to be massless. While the gluons and photon fit this criteria, the Z^0 and $W^{\pm}$ are massive gauge bosons. The Higgs mechanism is the final piece of the SM and introduces an additional scalar field, known as the Higgs field, with respective quanta, known as the Higgs boson (H). The Higgs boson is attributed to giving all fundamental particles in the universe their respective mass[1].

1.2 The Higgs mechanism

The gauge theories from which the SM arises describe infinite range forces, *i.e.* massless mediators, such as photons and gluons. However, the weak force mediators, the Z^0 and $W^{\pm}$, are massive particles. Moreover, in the unperturbed theory, fermions are massless. The mechanism which gives rise to the introduction of masses in the SM was developed by R. Brout, F. Englert, G. Guralnik, C. R. Hagen, T. Kibble and P. Higgs [4, 5, 6]. The mechanism is a spontaneous symmetry breaking phenomena which introduces a new scalar field known as the Higgs field. One unique property of the Higgs field, that sets it apart from the other force fields in the SM, is that it has a non-zero vacuum expectation value. This is visualized in the 'wine-bottle potential' shown in Figure 1, where the real and imaginary parts of the complex field ϕ are shown on the x- and y-axis. The complex field $\phi(\mathbf{r}, t)$ can be represented as a combination of two real fields, $\phi_1(\mathbf{r}, t)$ and $\phi_2(\mathbf{r}, t)$:

$$\phi(\mathbf{r}, t) = \phi_1(\mathbf{r}, t) + i\phi_2(\mathbf{r}, t), \tag{1}$$

where the potential energy density of the field is given by:

$$V(\phi(\mathbf{r}, t)) = \mu^2|\phi(\mathbf{r}, t)|^2 + \lambda|\phi(\mathbf{r}, t)|^4, \tag{2}$$

and μ and λ are real values. Since interactions in the Higgs field are invariant, one can represent a field transformation as:

$$\phi(\mathbf{r}, t) \rightarrow \phi(\mathbf{r}, t)e^{i\theta}, \tag{3}$$

where ϕ is an arbitrary phase parameter. The minima to the potential are considered for two cases where $\mu^2 > 0$ or $\mu^2 < 0$. The former corresponds to the case where the potential has a unique minimum at $\phi(\mathbf{r}, t) = 0$. This is analogous to Figure 1 where a particle sits at the pinnacle of the potential. For this case gauge invariance is conserved and a gauge boson is assumed to be massless. Such is the case for the photon. For the latter case the potential minimum is described as:

$$\phi(\mathbf{r}, t) = \phi_0 = (-\frac{\mu^2}{2\lambda})^{1/2}e^{i\theta}, \tag{4}$$

which anogolous to a particle sitting in a circle located at the bottom of Figure 1. For this case Equation 3 is not gauge invariant. This phenomena is known as spontaneous symmetry breaking and gives masses to the heavy gauge bosons, including the Higgs boson.

[1]Only 3% of a hadrons mass is attributed to the constituent quark masses, while the other 97% of the mass in the visible (not including dark matter) universe is due to the work done on the system to configure the quarks in a manner in which they do not interact [1].

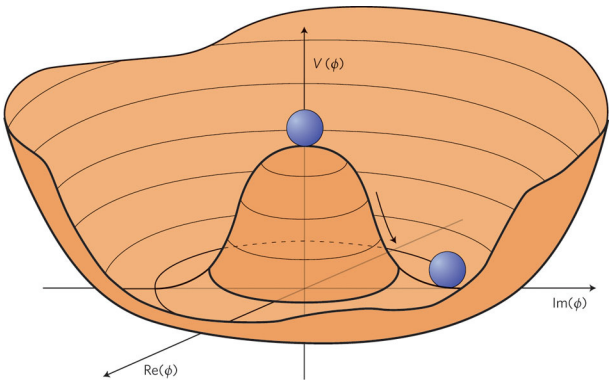


Figure 1: The wine-bottle potential analogous to the Higgs field allowing spontaneous symmetry breaking [7].

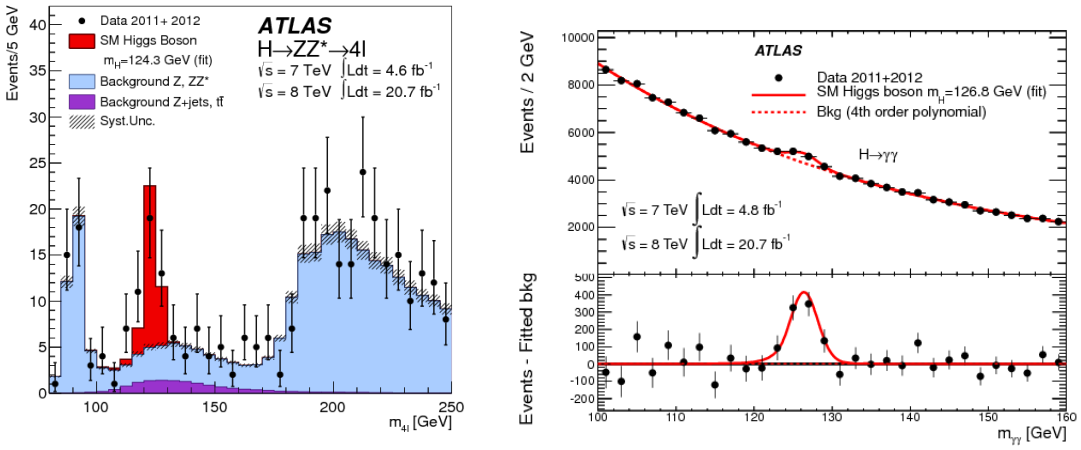
1.3 The discovery of a Higgs Boson

In the current SM formulation the Higgs boson is an isospin doublet. The precise mass of the Higgs boson, m_h, is however not predicted by the model and must be determined experimentally. The CDF and DØ experiments at the Fermilab Tevatron [8], as well as experiments the Large Electron-Positron Collider (LEP), had previously searched for the Higgs boson [9]. Although they found no direct evidence of a Higgs boson, they where able to place 95% confidence limits to exclude the regions of m_h where,

$$100 \ < m_h < 103 \text{ GeV and } 147 \ < m_h < 180 \text{ GeV}. \tag{5}$$

The region encompassing 125 GeV was not excluded since the combined limits at the Tevatron experiments had revealed an excess in this region. One of the main objectives of the Large Hadron Collider (LHC) at CERN, Geneva is to search for the Higgs particle using two large experiments, A Toroidal LHC Apparatus (ATLAS) and Compact Muon Solenoid (CMS), at unprecedented center of mass energies [10, 11]. The most sensitive channels at the LHC in the search for the Higgs boson with a mass in this range, in no particular order, are [12] gamma-gamma ($H \to \gamma\gamma$), four lepton ($H \to ZZ^{(*)} \to 4\ell$ ($\ell = e, \mu$)), $H \to WW^{(*)} \to \ell\nu\ell\nu$, di-tau ($H \to \tau^-\tau^+$), and $b\bar{b}$ ($H \to b\bar{b}$).

In 2012 a new boson was discovered with a mass of around 125 GeV, independently by both ATLAS and CMS at the LHC [12, 13]. Later combinations of the different analyses at higher luminosity revealed the boson to be a Higgs-like boson by both experiments [14, 15]. Figure 2 shows the distribution of the invariant mass of selected candidates compared to background expectation of the 4ℓ and $\gamma\gamma$ analysis with ATLAS. This shows a significant deviation from the background expectation at approximately 125 GeV, leading to the particle's discovery. Spin-parity measurements at both CMS and ATLAS have revealed evidence for the spin-0 and even charge parity nature of the SM Higgs boson [16, 17]. Combined coupling fits of the measured production and decay rates within the framework of the SM have found no significant deviation from the SM expectations within systematic uncertainties. These include meassurements of the Higgs boson Yukawa couplings to fermions, most recently meassured in the $H \to \tau\tau$ decays [18]. These results strongly suggest that the newly-discovered particle is indeed a Higgs boson.



(a) (b)

Figure 2: The distribution of the (a) four-lepton, and (b) di-photon invariant mass for the selected candidates compared to the background expectation for the combined $\sqrt{s} = 8$ TeV and $\sqrt{s} = 7$ TeV data sets from the ATLAS experiment [14].

1.4 Looking beyond the Standard Model at two-Higgs-doublet models

The SM described in Section 1.1 has thus far shown no known phenomenological inconsistencies and is considered to be void of mathematical weakness. There are however certain ambiguities that suggest that the SM may be a low energy limit of some larger underlying gauge theory. The problems with the SM are not phenomenological, but arise rather from the complexity and ambiguity of it's derivation. For one, the SM is a combination of three different, seemingly independent, interactions: electromagnetic, strong and weak. This is illustrated by the fact that the gauge group $G_g = SU_3^c \times SU_2 \times U_1$ is a direct product of three factors with different gauge coupling constants. Furthermore, there is no underlying reason as to why there is a parity violation in weak interactions, which is not present in strong interactions. There are also no underlying explanations for the repetition of fermionic families, a replica of the age-old question *"Why does the muon exist?"*, or the un-quantification of electric charge in quarks [19]. In addition, the most basic SM lacks any formal incorporation of the gravitational force, an explanation for the imbalance of matter over anti-matter, or a candidate for dark matter.

Finding answers to these questions has steered theoretical physics into searching for candidates for an underlying theory to the SM. Particularly promising candidates are the Grand Unified Theories (GUTs), in which the electromagnetic, weak and strong interactions are each a subset to an underlying gauge theory, with a single coupling constant [19]. In GUTs one usually finds new symmetry generators which relate the colour quantum numbers from SU_3^c, to flavour quantum numbers from $SU_2 \times U_1$. Quarks, anti-quarks, leptons and anti-leptons are then related by the new symmetries of an underlying group. The new symmetry generators bring with them an associated array of vector bosons carrying the colour and flavour quantum numbers. Unfortunately these vector bosons are not experimentally observable at present proton-proton collisions as they have predicted masses in the order of 10^{14} GeV. A verbose account of various GUTs is given by Langacker [19].

In the formulation of the SM, the simplest scalar structure has been assumed, a single SU_2 doublet. When considering that the fermionic structure is complex, with multiple families and family mixing, and that the scalar sector (or Higgs sector) has not been rigorously probed as of yet, there is no evidence to

assume that the Higgs sector should be as such. There is an interesting piece of evidence revealing a constraint on the Higgs sector stemming from the parameter ρ, defied as,

$$\rho \equiv \frac{m_W}{m_Z cos\theta_W}, \tag{6}$$

where m_W and m_Z are the masses for the Z and $W^{\pm}$ bosons, and θ_W is the mixing angle of the $W^{\pm}$ bosons. Experimentally it has been observed that $\rho \approx 1$ [20]. The most elementary extensions of the Higgs sector still satisfying this constraint (up to tree level) are by the addition of SU_2 doublets or singlets [21]. One of the simplest extensions of the Higgs field is therefore the addition of a single scalar doublet, which gives rise to a collection of models collectively known as two-Higgs-Doublet-Models (2HDMs). Motivations to 2HDMs include supersymmetric [22, 23, 24, 25, 26], axion [27], and baryogenesis [28] models, the later of which generates the required baryon asymmetry of the known universe.

In general, 2HDMs are very rich theories, with the most general scalar potentials including 14 parameters, and potentially having Charge Parity (CP)-conserving, CP-violating and charge-violating minima. For the subsequent study a handful of simplifying assumptions have been made. Firstly, CP is conserved in the Higgs sector, allowing one to distinguish between scalar and pseudoscalar bosons. Secondly, we have assumed that CP is not spontaneously broken, and furthermore, that all quadratic terms in the doublets are eliminated by discrete symmetries in the potential. In general these assumptions may be relaxed, a consideration made in the latter chapters of Ref. [21]. The Higgs field comprises of a simple non-trivial group called $\mathcal{Z}_2$ with elements Φ_1 and Φ_2. The most general gauge invariant scalar potential that includes two Higgs doublets, Φ_1 and Φ_2, as well as our aforementioned assumptions, is given by:

$$V(\Phi_1, \Phi_2) = m_{11}^2 \Phi_1^\dagger \Phi_1 + m_{22}^2 \Phi_2^\dagger \Phi_2 - (m_{12}^2 \Phi_1^\dagger \Phi_2 + \text{h.c}) + \frac{1}{2}\lambda_1 (\Phi_1^\dagger \Phi_1)^2 + \frac{1}{2}\lambda_2 (\Phi_2^\dagger \Phi_2)^2 + \lambda_3 (\Phi_1^\dagger \Phi_1)(\Phi_2^\dagger \Phi_2)$$

$$+\lambda_4 (\Phi_1^\dagger \Phi_2)(\Phi_2^\dagger \Phi_1) + \{\frac{1}{2}\lambda_5 (\Phi_1^\dagger \Phi_2)^2 + \text{h.c}\}. \tag{7}$$

After electroweak symmetry breaking, and assuming non-zero vacuum expectation values for both doublets, we are left with eight fields. Three of these are absorbed by, and give mass to, the $W^{\pm}$ and Z bosons. The remaining five give rise to physical Higgs bosons: two CP-even bosons, h and H, with notation such that $m_h < m_H$, one pseudoscalar A, and two charged scalar particles $H^{\pm}$. The initial phasespace of 14 parameters has now been reduced to just eight degrees of freedom. These are attributed to: the masses of the bosons, m_h, m_H, m_A, $m_H^{\pm}$; the ratio of the vacuum expectation values,

$$\tan\beta \equiv \frac{\upsilon_2}{\upsilon_1}, \tag{8}$$

where υ_1 and υ_2 are the non-zero vacuum expectation values of Φ_1 and Φ_2 respectively; the mixing angle between the CP-even bosons, α; and the m_{12}^2 potential parameter. The phases of both doublets may always be chosen in such a way as to force υ_1 and υ_2 to be positive, hence one can restrict the angle β to be $0 < \beta < \frac{\pi}{2}$. In the subsequent study we have chosen as a convention that the angle α is such that $sin(\beta - \alpha) \geq 0$. Both β and α are phenomenologically significant as they determine the interactions of various Higgs fields with the vector bosons and fermions.

	Type-I	Type-II
ξ_h^u	$\sin(\beta-\alpha)+\cos(\beta-\alpha)/\tan\beta$	$\sin(\beta-\alpha)+\cos(\beta-\alpha)/\tan\beta$
ξ_h^d	$\sin(\beta-\alpha)+\cos(\beta-\alpha)/\tan\beta$	$\sin(\beta-\alpha)-\tan\beta\cos(\beta-\alpha)$
ξ_h^ℓ	$\sin(\beta-\alpha)+\cos(\beta-\alpha)/\tan\beta$	$\sin(\beta-\alpha)-\tan\beta\cos(\beta-\alpha)$
ξ_H^u	$\cos(\beta-\alpha)-\sin(\beta-\alpha)/\tan\beta$	$\cos(\beta-\alpha)-\sin(\beta-\alpha)/\tan\beta$
ξ_H^d	$\cos(\beta-\alpha)-\sin(\beta-\alpha)/\tan\beta$	$\cos(\beta-\alpha)+\tan\beta\sin(\beta-\alpha)$
ξ_H^ℓ	$\cos(\beta-\alpha)-\sin(\beta-\alpha)/\tan\beta$	$\cos(\beta-\alpha)+\tan\beta\sin(\beta-\alpha)$
ξ_A^u	$1/\tan\beta$	$1/\tan\beta$
ξ_A^d	$-1/\tan\beta$	$\tan\beta$
ξ_A^ℓ	$-1/\tan\beta$	$\tan\beta$

Table 1: Yukawa coupling coefficients of the neutral bosons of the Type-I and Type-II 2HDM for up-type quarks (u), down-type quarks (d) and charged leptons (ℓ). These coefficients are defined such that the Yukawa Lagrangian terms are $-(m_\mathrm{f}/v)\bar{f}f\phi$ and $i(m_\mathrm{f}/v)\bar{f}\gamma_5 fA$ where $f = u, d, \ell$ and $\phi = h, H$ [29].

An earnest reader will have noticed that there has been no direct mention on the exact form of the discrete symmetry breaking used, which was utilized earlier to eliminate the tree-level Yukawa coupling terms leading to Equation 7. This is precisely because the form of the symmetry breaking affixes an additional freedom to 2HDMs. One can, for example, choose a $\mathcal{Z}_2$ symmetry of $\Phi_1 \to -\Phi_1$. This is considered to be a Type-I 2HDM. Furthermore, a Type-II 2HDM has a $\mathcal{Z}_2$ symmetry of $\Phi_1 \to -\Phi_1$ and $d_R \to -d_R$, where d_R refers to right-handed down-type fermions. In layman's terms this translates to all fermions, barring neutrinos, coupling only to Φ_2 in Type-I 2HDMs; in Type-II 2HDMs you have up-type right-handed fermions coupled to Φ_2 and down-type right-handed fermions coupled to Φ_1. The Lepton-specific (Type-III) model is a third type of 2HDM similar to Type-I except that the leptons couple to Φ_1 instead of Φ_2. The Flipped (Type-IV) model is similar to Type-II apart from the fact that the leptons couple to Φ_2, instead of Φ_1. For every 2HDM considered in this study the coupling of the h boson to vector bosons is the same as the SM coupling times $\sin(\beta-\alpha)$; coupling of the H boson to vector bosons is the same as the SM coupling times $\cos(\beta-\alpha)$; for the A boson these couplings vanish. The couplings of Type-I and Type-II 2HDMs are shown in Table 1.

In order to conclude on a phenomenological point we consider the fact that these 2HDMs will approach the SM at a SM-like limit, where $\cos(\beta-\alpha) \to 0$, opening a gateway to experimental inquisition of the SM. However, the assumptions imposed on the 2HDMs here need to be considered alongside any succeeding experimental methodology and subsequent observation. Furthermore, additional restrictions on the models will be visited and motivated in the subsequent Section 1.5. These include assumptions made on the masses of the five Higgs bosons stemming from 2HDMs, as well as a choice of the m_{12}^2 parameter. In retrospect, the subsequent study will be fairly localized in the vast phasespace provided by 2HDMs, but serves as a useful tool in the search for Beyond Standard Model (BSM) physics.

1.5 Motivation for a search of the pseudoscalar Higgs boson

Due to it's high search sensitivity, particularly from the increased branching fractions of the MSSM Higgs bosons to τ leptons at large $\tan\beta$, the flagship search for a pseudoscalar A boson is through the di-tau decay channel, $A \to \tau\tau$. This search is also important in searches for Supersymmetry (SUSY) in the context of Minimal Supersymmetric Standard Models (MSSMs) which contain two-Higgs-Doublets [21]. In a search for the neutral Higgs boson of the MSSM in the $A \to \tau\tau$ channel, 95% CL (Confidence Level) upper limits are placed on the phasespace of various MSSM scenarios [30]. One such scenario is the the MSSM m_h^{max} scenerio, where the mass m_h is maximised for every chosen value of the MSSM parameter

space. Figure 3 shows the results interpreted in the MSSM m_h^{max} scenerio, where the $h/H/A \to \tau\tau$ decays have been excluded in regions of the ($\tan\beta$, m_A) plane at 95% CL. Areas above the observed limits are excluded. The contours of constant m_H and m_h for the m_h^{max} scenerio are also shown. If one assumes that $m_h = 125$ GeV, with a 3 GeV uncertainty, only the area within the $m_h = 122$ GeV and $m_h = 128$ GeV contours are allowed. This translates to the MSSM m_h^{max} scenerio being excluded for all $\tan\beta$ values where $m_A < 165$ GeV, and for all m_A values where $\tan\beta < 4$ or $\tan\beta > 10$. Upper limits are also placed on the cross section times branching ratio of a model independant scalar boson, ϕ, decaying to $\tau\tau$ produced by both gluon-fusion and b-associated production, as a function of m_ϕ. Ranging from the low $m_\phi = 90$ GeV to $m_\phi = 1$ TeV range, the limits on $\sigma \times \text{BR}(\phi \to \tau\tau)$ are 29 pb to 7.4 fb and 6.4 pb to 7.2 fb for gluon-fusion and b-associated production, respectively. Although these limits show the high sensitivity of the $A \to \tau\tau$ search, Figure 3 shows that the search lacks sensitivity at low $\tan\beta$. Therefore a search in the $A \to Zh$ channel, which is sensative at low $\tan\beta$, compliments the $A \to \tau\tau$ search.

Another important motivation for the search of the A boson predicted by 2HDMs lies within a sensitivity study of various BSM physics scenarios at high luminosity, specifically speaking, at 300 fb^{-1}and 3000 fb^{-1}of pp data at $\sqrt{s} = 14$ TeV using the ATLAS detector [29]. The constituent sensitivity studies include the heavy Higgs boson, with di-muon ($H \to \mu^+\mu^-$) and four lepton ($H \to ZZ^{'} \to \ell^+\ell^-\ell^+\ell^-$) final states, and a sensitivity study of the gluon-fusion produced A boson, which decays to Zh, where $Z \to \ell^+\ell^-$ and $h \to b^+b^-$. For the latter scenerio reported sensitivities of cross sections times branching ratios are from 5 to 0.07 fb for an A mass in the range of 220-900 GeV, at an integrated luminosiy of 3000 fb^{-1} [29]. The results for 300 fb^{-1}are about 3 to 4 times larger with respect to the upper limit. Figure 4 shows the quoted confidence level upper limits for the $A \to Zh$ study [29].

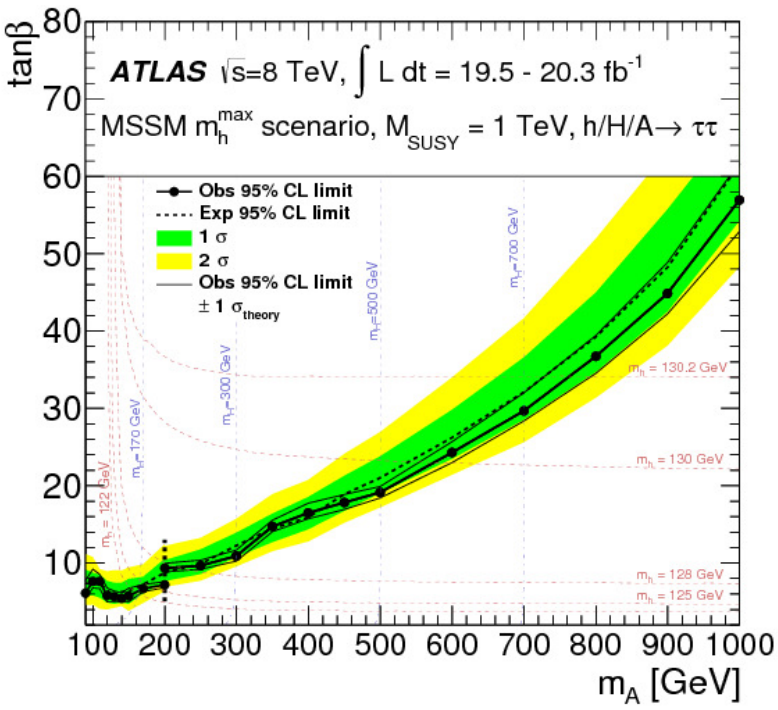


Figure 3: Expected and observed 95% CL upper limits from the $h/H/A \rightarrow \tau\tau$ analysis on $\tan\beta$ as a function of m_A for the MSSM $m_h^{\max}$ scenerio. The vertical dashed line at 200 GeV is the transition point between low and high mass searches, where the limits from each search meet. Contour lines of constant m_h and m_H are shown in red and blue, respectivaly. The regions above the lines are excluded [30].

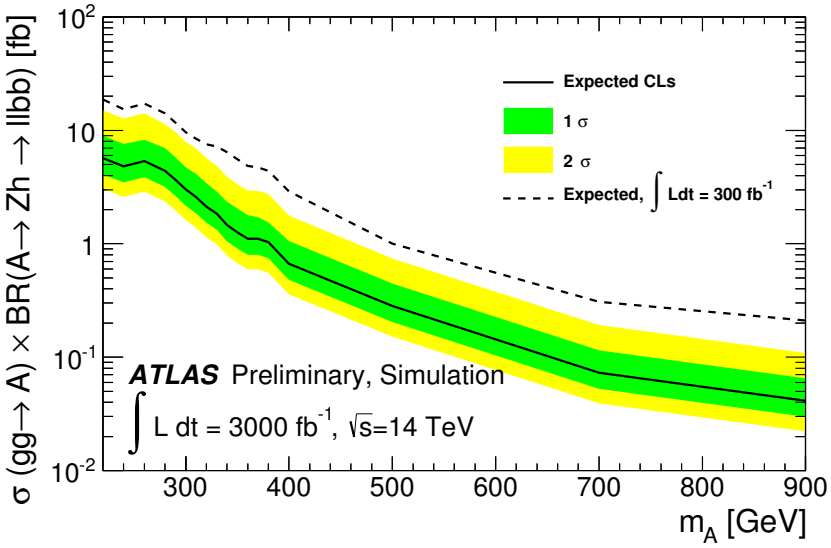
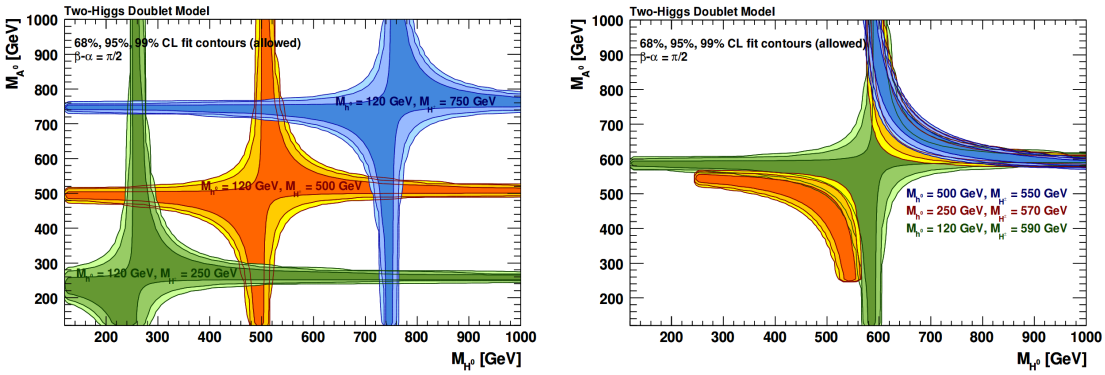


Figure 4: Expected 95% confidence level upper limits for an integrated luminosity of 300 fb (dashed line) and 3000 fb (solid line) on the gluon-fusion production cross section of a CP-odd Higgs boson A times its decay branching ratio to $A \rightarrow Zh \rightarrow \ell\ell bb$ are presented as a function of the A boson mass, m_A [29].

This section relies heavily on the description of the sensitivity study mentioned above, which provides the foundation for the subsequent $A \to Zh \to \ell\ell\tau\tau$ analysis. The first assumption made is that the newly discovered Higgs boson, described in Section 1.3, is actually the lighter one of the CP-even Higgs bosons predicted by 2HDMs. Subsequently $m_h = 125$ GeV, and the degrees of freedom are reduced by one parameter. Another assumption made in Ref. [29] which has been adopted by our study is that $m_A = m_H = m_{\mathrm{H}^\pm}$. This is motivated by Figure 5(a), which shows the restrictions on the Higgs boson masses in 2HDMs in the (m_h, m_A) plane when fixed choices of $\beta - \alpha = \frac{\pi}{2}$ and $m_h = 120$ GeV have been made, and m_H is allowed to vary [31]. The Higgs mass here was chosen as 120 GeV since the SM fit to electroweak precision data found the Higgs boson mass to be 120^{+12}_{-5} GeV. It is shown in Figure 5(a) that similar values of m_H, m_A and $m_{\mathrm{H}^\pm}$ are preferred when fixing m_h and $\beta - \alpha$. Figure 5(b) shows the same restrictions on the (m_H, m_A) plane, but when m_h and $m_{\mathrm{H}^\pm}$ have been allowed to vary. The restrictions on m_H and m_A become more stringent as m_h increases, limiting the freedom they have to adopt any value. However, this plays no effect for our choice of $m_h = 125$ GeV which is close enough to 120 GeV for the mass splitting to be disfavoured. Finally, the potential parameter which softly breaks $\mathcal{Z}_2$ symmetry is chosen as $m^2_{12} = m^2_A \tan\beta/(1 + \tan^2\beta)$ [29]. Following these assumptions, the remaining free parameters are m_A, $\tan\beta$, and $\cos(\beta - \alpha)$ which we know is close to 1 at the SM-limit [29].



(a) (b)

Figure 5: Constraints in the 2HDM. 68%, 95% and 99% CL allowed fit contours in the (m_h, m_A) plane for $\beta - \alpha = \frac{\pi}{2}$, (a) as derived from the fit of $M_h = 120$ GeV and $M_{\mathrm{H}} = 250$, 500 and 750 GeV, and (b) for $M_h = 120$, 250, 500 GeV and $M_{\mathrm{H}^\pm} = 550$, 570 and 590 GeV [31].

Production of a heavy CP-odd particle A, predicted by 2HDMs, is primarily through gluon-fusion, or to a lesser degree, through b-associated production at high values of $\tan\beta$. Feynman diagrams of both the gluon-fusion and b-associated production of the A boson are shown in Figure 6. The production of heavy quarks in high-energy processes, such as b-associated production, is generally described in QCD by the so called four-flavour or five-flavour schemes [32]. In the former scheme NLO calculations are only available for processes where b-quarks appear in the final state. These final states are considered to be massive, making computations more complicated. The latter scheme lends itself to calculations where b-quarks are included in the initial state. These calculations are simpler than the four-flavour counterparts since large initial state logarithms can be added into the b parton distribution function (PDF). For a Type-I 2HDM, and the parameter space considered for this study, the contribution from b-associated production is less than 3% that of gluon-fusion [29]. However, for a Type-II 2HDM the A boson b-associated production increases in terms of $\tan\beta$, where for $\tan\beta = 2$ the ratio of b-associated production is less than 4% that of gluon-fusion, whereas it is $\approx 25\%$ at $\tan\beta = 3$ [29]. For both Type-II and Flipped models, the b-associated production dominates over gluon-fusion for $\tan\beta \gtrsim 10$. In this study we are mainly concerned with the production of A bosons through gluon-fusion, due to the clear dominance it

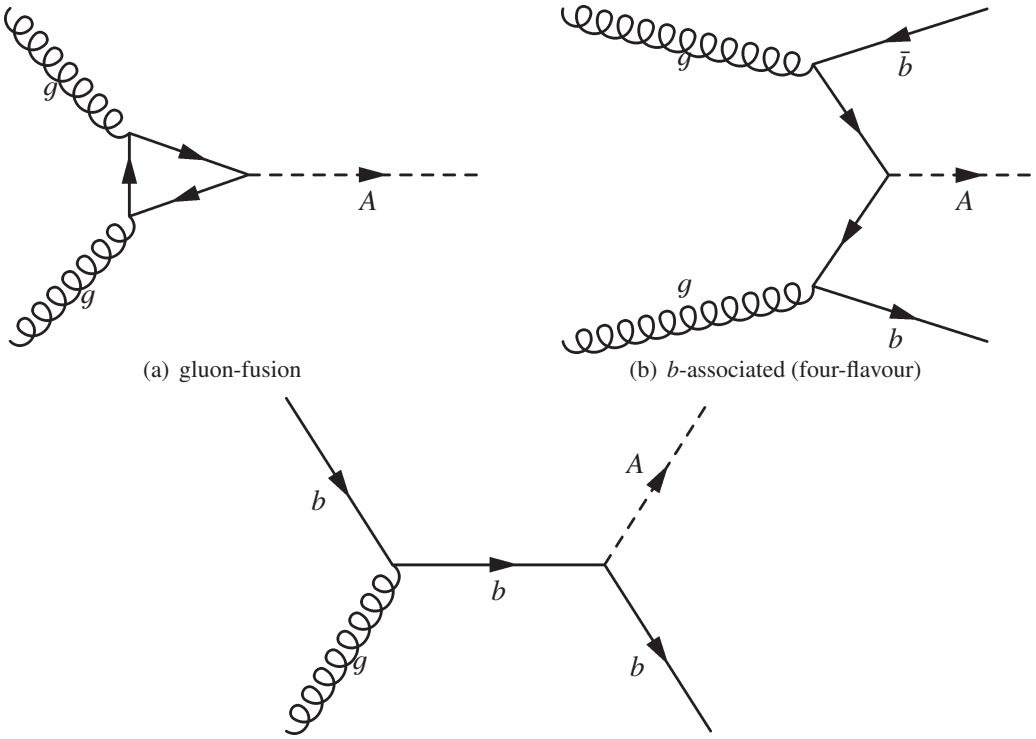
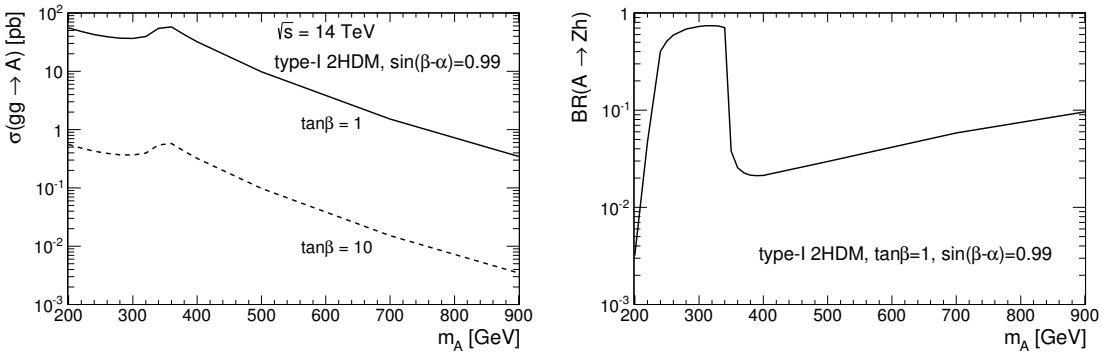


Figure 6: Feynman diagrams for (a) gluon-fusion and b-associated production in the (b) four-flavour and (c) five-flavour schemes of the neutral A boson.

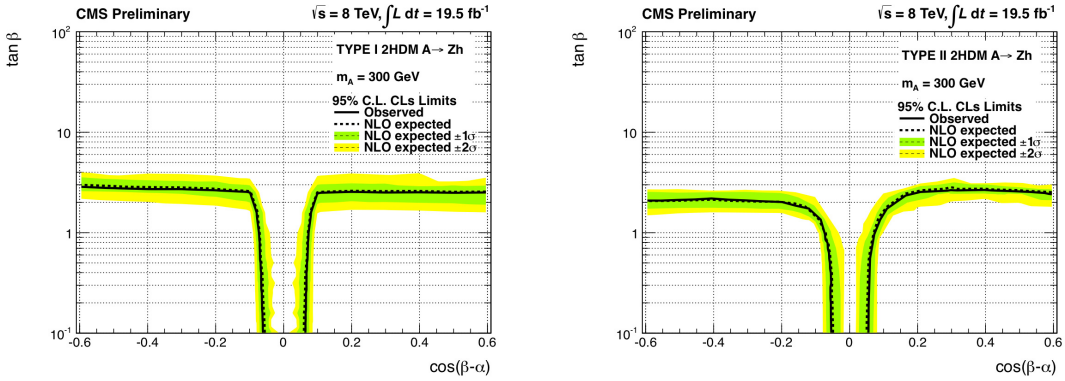
has over A boson production when compared to other processes. The gluon-fusion cross-sections of A for a Type-I 2HDM at 14 TeV pp collisions, calculated with SusHi 1.1.0 [33], are shown in Figure 7(a) as a function of m_A. Generally speaking the A decaying to a Z boson and a light SM-like Higgs h ($A \to Zh$) is the dominant decay mode of A in any 2HDM when the mass of the A is less than two times the mass of the top-quark ($m_h + m_Z < m_A < 2m_t$). At masses of $m_A > 2m_t$ the branching ratio BR($A \to Zh$) drops drastically, as seen in Figure 7(b), due to the exposed $t\bar{t}$ kinematic region.

By setting upper limits on the cross section times decay branching ratio of a specific final state of the $A \to Zh$ channel, as done in Figure 4, we are able to search for the existence of the A boson and subsequent traces of BSM physics. As a bi-product of these studies one is able to exclude the existence of 2HDMs from certain areas of the m_A, $\tan\beta$, and $\cos(\beta - \alpha)$ phasespace if no sufficient excess above the upper limits is observed. An example of this can be seen in a CMS experiment in which significant portions of parameter space from 2HDMs is excluded when searching in the $H \to hh$ and $A \to Zh$ channels using a 19.5 fb^{-1}data sample at 8 TeV pp collisions [34]. The range of m_A probed is from 260 GeV to 360 GeV. Figure 8 show the areas of which Type-I and Type-II 2HDMs are excluded in the ($\tan\beta$, $\cos(\beta - \alpha)$) plane for a fixed choice of $m_A = 300$ GeV. The areas encapsulated by the black solid lines have been excluded. The newest search from CMS looks for the gluon-fusion and b-associated produced pseudoscalar boson in the $A \to Zh \to \ell\ell b\bar{b}$ channel, based on 19.7 fb^{-1}of proton-proton collisions at $\sqrt{s} = 8$ TeV [35]. Model independent 95% CL upper limits where placed on the $\sigma\times$BR($A \to Zh \to \ell\ell b\bar{b}$) in an A mass range of $2m_{top} \leq m_A \leq 600$ GeV at a fixed A width Γ_A, as well as for varying widths at fixed m_A. Figure 9 shows limits on $\sigma \times$ BR($A \to Zh \to \ell\ell b\bar{b}$) as a function of Γ_A and m_A. Interpretations of the the limits are cast as exclusion regions in the ($\tan\beta$, $\cos(\beta - \alpha)$) plane for Type-I and Type-II 2HDMs assuming $m_A = 300$ GeV in Figure 10.



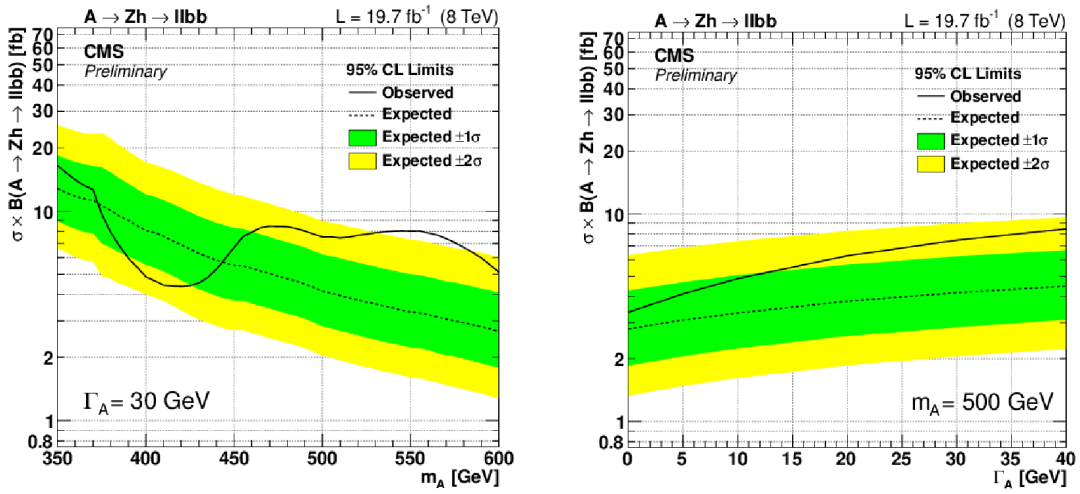
(a) (b)

Figure 7: The gluon-fusion (a) production cross section and (b) branching ratio BR($A \to Zh$) for a Type-I 2HDM pseudoscalar boson A as a function of m_A, where $\sin(\beta - \alpha) = 0.99$ [29].



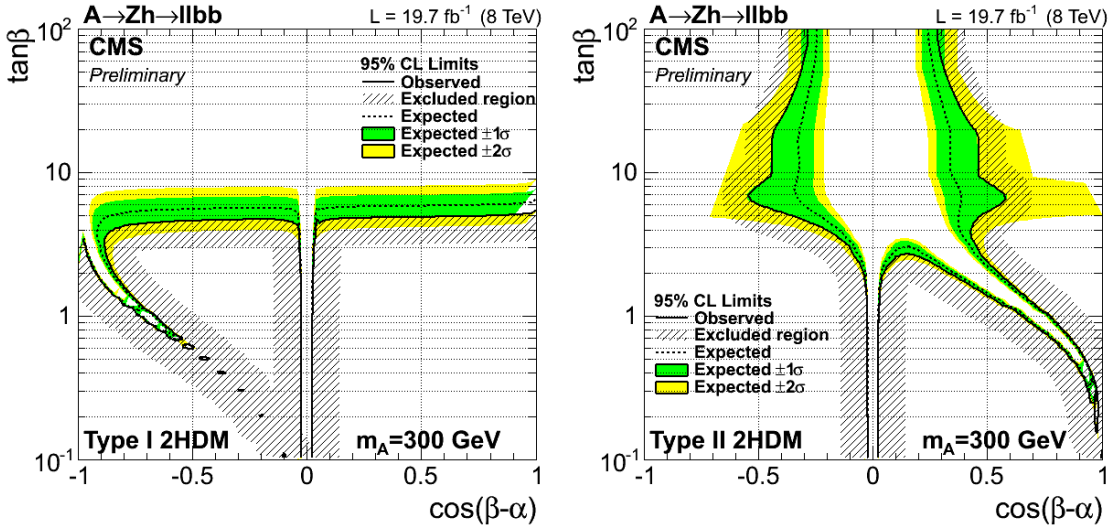
(a) (b)

Figure 8: Observed and expected limits on A of mass 300 GeV in the ($\tan\beta$, $\cos(\beta - \alpha)$) plane for (a) Type-I and (b) Type-II 2HDMs [34].



(a) (b)

Figure 9: Observed and expected 95% CL upper limits on $\sigma \times \mathrm{BR}(A \to Zh \to \ell\ell b\bar{b})$ for (a) varying Γ_A at $m_A = 500$ GeV, and (b) varying m_A at 30 GeV $\Gamma_A = 30$ [35].



(a) (b)

Figure 10: Observed and expected 95% CL limits on A of mass 300 GeV in the $(\tan\beta, \cos(\beta-\alpha))$ plane for (a) Type-I and (b) Type-II 2HDMs [35].

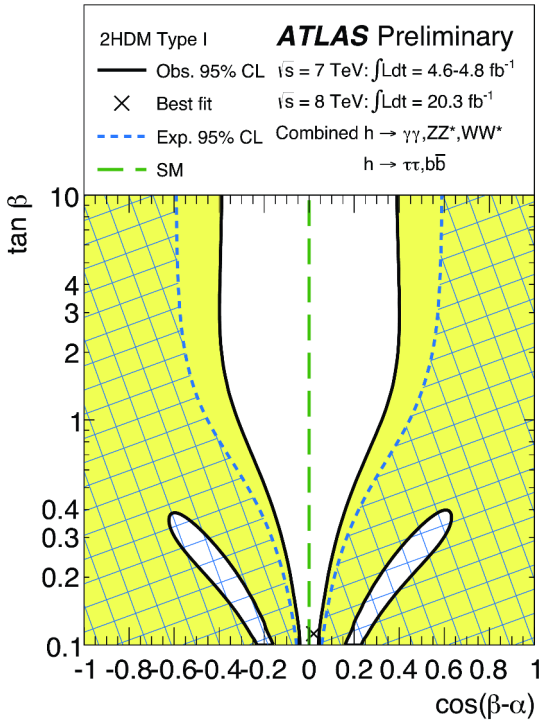
In addition to the limits placed by the direct search in Ref. [34], indirect exclusion limits have been placed on 2HDMs in the $(\tan\beta, \cos(\beta-\alpha))$ plane by interpreting the observed couplings of the discovered Higgs boson to other particles [36]. In this study the ratio of the expected 2HDM couplings to the SM case are cast as functions of β and α. The couplings of a SM Higgs boson to other SM particles would differ from the coupling of the light h boson predicted by 2HDMs depending on the values of β and α considered. The ratio of the predicted coupling scale factors of the 2HDM h boson to vector bosons, up-type and down-type quarks, and leptons to the predicted SM Higgs couplings is shown for the four 2HDM types in Table 2. The study assumes $m_A = 125$ GeV, and that the Higgs boson has the same production modes

predicted by the SM. The ($\tan\beta$, $\cos(\beta-\alpha)$) phasespace is scanned, and where the meassured Higgs couplings disagree with the 2HDM predictions, at 95% CL or greater, areas of the ($\tan\beta$, $\cos(\beta-\alpha)$) plane are excluded. Figure 11 shows the the results from likelihood fits to the measured rates of Higgs boson production and decay. Regions of the ($\tan\beta$, $\cos(\beta-\alpha)$) plane for the four 2HDM types are excluded at a 95% confidence level for $m_A = 300$ GeV.

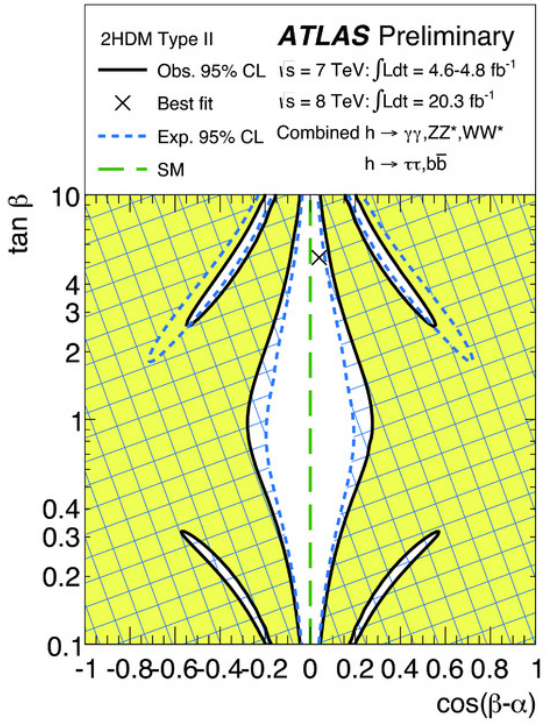
Coupling scale factor	Type-I	Type-II	Type-III	Type-IV
κ_V	$\sin(\beta-\alpha)$	$\sin(\beta-\alpha)$	$\sin(\beta-\alpha)$	$\sin(\beta-\alpha)$
κ_u	$\cos(\beta)/\sin(\alpha)$	$\cos(\beta)/\sin(\alpha)$	$\cos(\beta)/\sin(\alpha)$	$\cos(\beta)/\sin(\alpha)$
κ_d	$\cos(\beta)/\sin(\alpha)$	$-\sin(\alpha)/\cos(\beta)$	$\cos(\beta)/\sin(\alpha)$	$-\sin(\alpha)/\cos(\beta)$
κ_ℓ	$\cos(\beta)/\sin(\alpha)$	$-\sin(\alpha)/\cos(\beta)$	$-\sin(\alpha)/\cos(\beta)$	$-\sin(\alpha)/\cos(\beta)$

Table 2: The predicted coupling scale factor of the light 2HDM h boson to vector bosons (κ_V), up-type quarks (κ_u), down-type quark (κ_d), and leptons (κ_ℓ) expressed as ratios to the corresponding predicted SM Higgs couplings for the different 2HDM types [36].

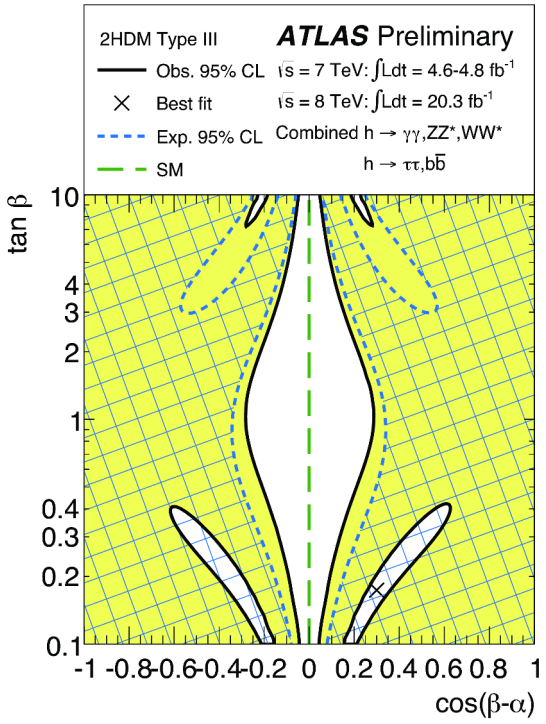
For the subsequent analysis it is assumed that the mass of the A boson is within the range of 220 GeV ($\approx m_h + m_Z$) and 1000 GeV. Since the study is assuming that the 2HDMs approach the SM-limit, values of $\cos(\beta-\alpha)$ close to 0 are chosen. Decay branching ratios are calculated with the publicly available package, 2HDMC [37], while the cross sections are calculated using SusHi [33], for varying $\tan\beta$ values. The cross sections and branching ratios at various scenarios for Type-I and Type-II 2HDMs are summarized in Tables 3–4. The branching ratios of the light CP-even boson h at 125 GeV to $\tau\bar{\tau}$ are also quoted. The final state considered is the Z boson decaying to a di-lepton pair ($Z \to \ell^+\ell^-$, where $\ell \neq \tau$) and the h boson decays to a di-tau pair ($h \to \tau^+\tau^-$). Due to the initial objective of combining the results into a single $\tau\tau$ analysis, many of the results featured in this thesis are of the combined hadronic and leptonic final states. This thesis will focus on providing a complete description of the fully hadronic, $\tau_{had}\tau_{had}$, final state analysis, but will also make brief mention of the methodology and results from the leptonic cases, $\tau_{lep}\tau_{had}$ and $\tau_{lep}\tau_{lep}$.



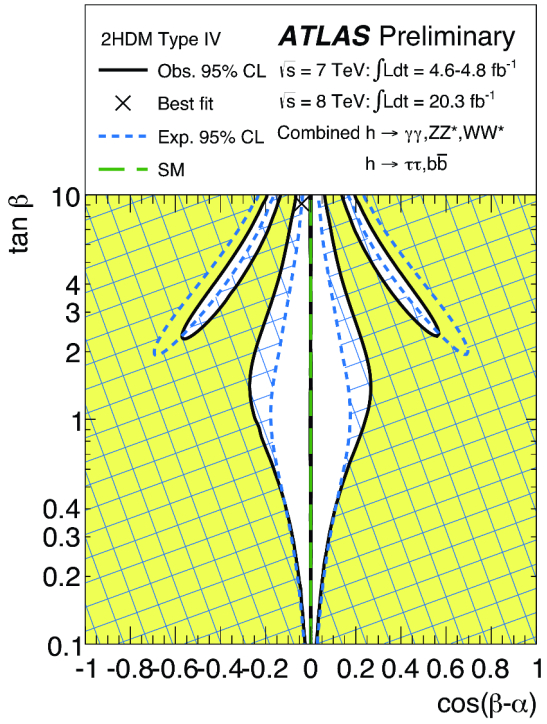
(a) Type-I



(b) Type-II



(c) Lepton-specific



(d) Flipped

Figure 11: Constrains in the $(\cos(\beta-\alpha), \tan\beta)$ plane of (a) Type-I, (b) Type-II, (c) lepton-specific, and (d) flipped 2HDM models set by measurements of the Higgs couplings to other particles. The light shaded and hashed regions indicate the observed and expected exclusions contours respectively [36].

m_{A} [GeV]	$\sin(\beta-\alpha)$	$\cos(\beta-\alpha)$	$\sigma(gg \to A)$ [pb]	BR($A \to Zh$)	BR($h \to \tau\tau$)
			Type-I and $\tan\beta$=1		
260	0.999	0.045	6.0135	0.11660	0.06079
300	0.999	0.045	4.7897	0.17915	0.06079
340	0.999	0.045	4.4484	0.04540	0.06079
360	0.999	0.045	4.8650	0.00158	0.06079
500	0.999	0.045	1.7543	0.00260	0.06079
800	0.999	0.045	0.1281	0.00755	0.06079
1000	0.999	0.045	0.0291	0.01235	0.06079
			Type-I and $\tan\beta$=10		
260	0.999	0.045	3.0258	0.92957	0.05978
300	0.999	0.045	2.4124	0.95619	0.05978
340	0.999	0.045	2.2424	0.82626	0.05978
360	0.999	0.045	2.4535	0.13629	0.05978
500	0.999	0.045	0.8855	0.20695	0.05978
800	0.999	0.045	0.0647	0.43190	0.05978
1000	0.999	0.045	0.0147	0.55573	0.05978
			Type-I and $\tan\beta$=1		
260	0.600	0.800	2.6938	0.97688	0.07293
300	0.600	0.800	2.1493	0.98589	0.07293
340	0.600	0.800	1.9991	0.93837	0.07293
360	0.600	0.800	2.1880	0.33563	0.07293
500	0.600	0.800	0.7903	0.45518	0.07293
800	0.600	0.800	0.0578	0.70879	0.07293
1000	0.600	0.800	0.0131	0.80019	0.07293
			Type-I and $\tan\beta$=10		
260	0.600	0.800	1.3624	0.99976	0.06282
300	0.600	0.800	1.0866	0.99986	0.06283
340	0.600	0.800	1.0103	0.99934	0.06283
360	0.600	0.800	1.1056	0.98059	0.06283
500	0.600	0.800	0.3992	0.98817	0.06283
800	0.600	0.800	0.0292	0.99591	0.06283
1000	0.600	0.800	0.0066	0.99751	0.06283

Table 3: Cross-section times branching ratio for gluon-fusion produced A boson production, decaying via Zh to $ll\tau\tau$ final state for 2HDM Type-I. For more details see the text.

m_A [GeV]	$\sin(\beta-\alpha)$	$\cos(\beta-\alpha)$	$\sigma(gg \to A)$ [pb]	BR($A \to Zh$)	BR($h \to \tau\tau$)
			Type-II and $\tan\beta$=1		
260	0.999	0.045	6.0135	0.11915	0.05714
300	0.999	0.045	4.7897	0.18208	0.05714
340	0.999	0.045	4.4484	0.04556	0.05713
360	0.999	0.045	4.8650	0.00158	0.05713
500	0.999	0.045	1.7543	0.00260	0.05713
800	0.999	0.045	0.1281	0.00754	0.05713
1000	0.999	0.045	0.0291	0.01235	0.05713
			Type-II and $\tan\beta$=10		
260	0.999	0.045	3.0258	0.00363	0.03358
300	0.999	0.045	2.4124	0.00962	0.03358
340	0.999	0.045	2.2424	0.01728	0.03358
360	0.999	0.045	2.4535	0.01912	0.03358
500	0.999	0.045	0.8855	0.04951	0.03358
800	0.999	0.045	0.0647	0.14487	0.03358
1000	0.999	0.045	0.0147	0.22088	0.03358
			Type-II and $\tan\beta$=1		
260	0.600	0.800	2.6938	0.97743	0.00702
300	0.600	0.800	2.1493	0.98616	0.00702
340	0.600	0.800	1.9991	0.93859	0.00702
360	0.600	0.800	2.1880	0.33565	0.00702
500	0.600	0.800	0.7903	0.45518	0.00702
800	0.600	0.800	0.0578	0.70879	0.00702
1000	0.600	0.800	0.0131	0.80019	0.00702
			Type-II and $\tan\beta$=10		
260	0.600	0.800	1.3624	0.53851	0.08955
300	0.600	0.800	1.0866	0.75673	0.08955
340	0.600	0.800	1.0103	0.84919	0.08955
360	0.600	0.800	1.1056	0.86189	0.08955
500	0.600	0.800	0.3992	0.94343	0.08955
800	0.600	0.800	0.0292	0.98190	0.08955
1000	0.600	0.800	0.0066	0.98910	0.08955

Table 4: Cross-section times branching ratio for gluon-fusion produced A boson production, decaying via Zh to $ll\tau\tau$ final state for 2HDM Type-II. For more details see the text.

2 The ATLAS Experiment

2.1 CERN and the Large Hadron Collider

The LHC [38] is currently the largest man-made particle accelerator, capable of proton-proton (pp), and heavy ion (lead-proton (Pb-p) and lead-lead (Pb-Pb)) collisions. It has a circumference of 27 km, a design center-of-mass energy of 14 TeV, and peak instantaneous luminosity of 10^{34} cm^{-2}s^{-1} for pp collisions. Beam crossings are 25 ns apart at design luminosity and there are on average 25 interactions per crossing. The first round of data taking (Run-I) of pp collisions begun in early 2010, and continued up until the first long shutdown period in February 2013, with a few shorter shutdowns to allow for lead-ion collisions, and to facilitate the festive seasons. During this time the LHC was able to reach a

center-of-mass energy of 8 TeV per beam, making it the worlds highest-energy particle accelerator. The LHC has been in its first long shutdown to facilitate upgrades in the accelerator complex and detectors in order to allow for the larger center-of-mass energy expected in the second run of operations beginning early 2015 (Run-II).

Seven detectors have been constructed at the LHC to look at different physical processes. There are two general purpose detectors, ATLAS and the CMS, whose roles are to search for the Higgs boson and shed light on topics like dark matter, supersymmetry, top-quark physics, beauty physics, *etc.*. A Large Ion Collider Experiment (ALICE) detector [39] studies a form of matter called quark-gluon-plasma that existed shortly after the Big Bang, while the LHCb detector [40] is used to investigate the reasons behind the "lack" of antimatter in the universe. The last three, TOTEM [41], MoEDAL [42] and LHCf [43] are smaller, sharing the interaction points of the other larger experiments, and look at more specific processes.

2.2 The ATLAS detector

The ATLAS experiment is one of the two general-purpose detectors at the LHC. It was designed to accommodate a wide spectrum of different physics signatures and explore processes stemming from the TeV mass scale, where groundbreaking discoveries are expected. The focus of ATLAS is to search for and measure SM and BSM physics processes, amongst which are searches for supersymmetry and exotic processes, including black hole production [44]; and until recently to search for the elusive Higgs boson, which was discovered in 2012 by ATLAS [12] and CMS [13].

ATLAS is intended to detect primary interactions and then reconstruct them for analysis. In order to identify the diverse range of particles which are produced at the interaction point, ATLAS is comprised of different detector sections and provides a large acceptance covering a vast spatial range. The original design of the detector enhanced certain criteria which where crucial for the experiment's success. The first stage in detection is the tracking of charged particles, which has to be effective at high luminosity to attain high momentum lepton measurements, as well as full event reconstruction at low p_T. Triggering and measurements of particles needs to be effective at low p_T ranges. ATLAS requires good EM calorimetry in order to identify and measure electrons and photons effectively. Hadronic calorimetry is required for accurate jet and event energy measurements. Unlike most charged particles, muons aren't stopped by the calorimeters, and their identification is done using the outer muon chambers providing a system for high precision muon momentum measurements. Momentum measurements are done with the help of a configuration of magnets based on an inner superconducting solenoid surrounding the inner detector cavity, and eight large superconducting toroidal magnets outside the calorimeters. Neutrinos are not detected by either the calorimeters nor the muon chambers and escape the ATLAS detector. They carry an energy that is therefore not detectable by ATLAS. The neutrinos are therefore accounted for by the total Missing Transverse Energy (MET) of the event, denoted E_T^{miss}. A cross-sectional view of the ATLAS detector is shown in Figure 12.

The ATLAS detector is a multi-purpose particle detector with approximately forward-backward symmetric cylindrical geometry. This section presents a brief overview of the ATLAS experiment as described by reference [46]. ATLAS uses a right handed coordinate system with the origin at the interaction point. The z-axis is along the beam pipe, x-axis points towards the center of the LHC ring and the y-axis points up. Polar coordinates (r, ϕ) are used in the transverse plane, ϕ being the azimuthal angle around the beam pipe. The pseudorapidity η is defined as

$$\eta = -\ln(\tan(\theta/2)), \tag{9}$$

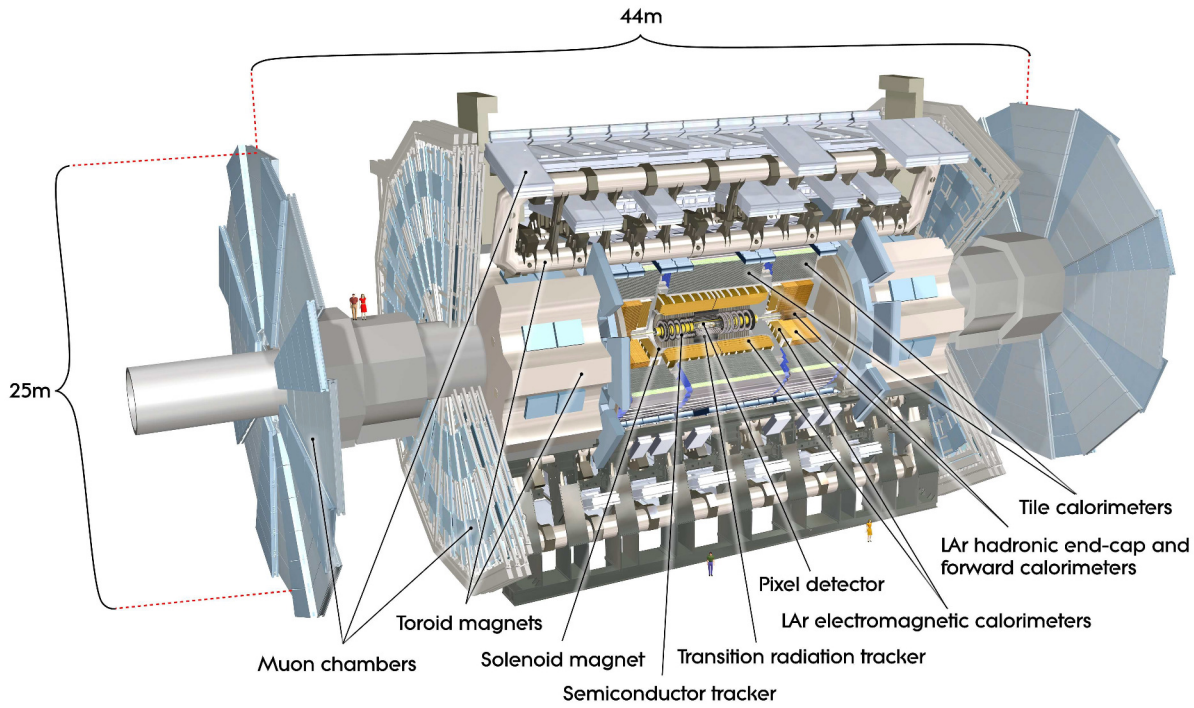


Figure 12: Cut-away view of the ATLAS detector. The dimensions of the detector are 25 m in height and 44 m in length. The overall weight of the detector is approximately 7000 tonnes [45].

where θ is the angle between the particle momentum 3-vector and the beam axis. The Inner Detector (ID) covers $|\eta| < 2.5$ and consists of silicon pixels, silicon micro-strips and a transition radiation tracker. The ID is surrounded by a superconducting solenoid providing a 2 T magnetic field. Surrounding the ID are two calorimeters, the inner EM and the outer hadron calorimeters. The EM calorimeter measures the energy and the position of EM showers within $|\eta| < 3.2$ as well as hadronic showers in the end-cap ($1.5 < |\eta| < 3.2$) and forward ($3.1 < |\eta| < 4.9$) regions. The hadronic calorimeter measures hadronic showers in the central region ($|\eta| < 1.7$). The muon spectrometer surrounds the calorimeters and consists of three subsystems: eight superconducting air-core toroid magnets, a system of tracking chambers and a fast tracking chamber for triggering. A three-level trigger system selects events to be recorded for offline analysis.

The ATLAS detector has approximately 100 million electronic channels in total. Interactions in the ATLAS detector produce an enormous volume of data. ATLAS makes use of a trigger system which is designed to record interesting events at approximately 200 Hz (up to around 400 Hz in later revisions) of the LHCs 40 MHz bunch crossing rate. The Worldwide LHC Computing Grid (WLCG), which is an international collaborative project that consists of a grid-based computer network, is used to handle and analyze the large volume of data.

2.2.1 Magnet System

The Lorentz force law is a well founded law of electrodynamics describing the magnetic force $\mathbf{F}_{\text{mag}}$ on a charge q, moving with velocity $\mathbf{v}$ in a magnetic field $\mathbf{B}$ [47]:

$$\mathbf{F}_{\text{mag}} = q(\mathbf{v} \times \mathbf{B}). \tag{10}$$

As a simple example we consider a particle of mass m, charge q and momentum p, moving in a circular orbit of radius R at a constant speed, in a constant magnetic field orthogonal to the orbit. Since the motion of the particle and magnetic field are perpendicular, the right hand side of Equation 12 reduces to qvB. If we replace $\mathbf{F}_{\text{mag}}$ with the equation for centripetal acceleration, the left hand side of Equation 12 reduces to $\frac{mv^2}{R}$.

$$qvB = \frac{mv^2}{R}, \text{or } p = qBR \tag{11}$$

Equation 11 is known as the cyclotron formula [47] and allows one to calculate a charged particle's momentum from the curvature of its motion, by submerging it in a constant magnetic field. For relativistic particles in cyclotron motion, the centripital force is not $\frac{mv^2}{R}$ as in classical mechanics. The velocity v is replaced by the ordinary velocity $\mathbf{u} = \frac{d\mathbf{l}}{dt}$ meassured by a ground observer, leaving the force as [47]:

$$F = \frac{dp}{dt} = p\frac{d\theta}{dt} = p\frac{u}{R}. \tag{12}$$

Hence for relativistic particles the cyclotron formula is equivalent to Equation 11, except that p is now the relativistic momentum. Particle physicists have been exploiting this technique from as early as the days of the cloud chamber experiments conducted in the 1920s in order to calculate a charged particles momentum [1]. In ATLAS a system of magnets provides, to a good approximation, sections with constant magnetic fields to the experiment, in order to curve charged particles, and provide accurate momentum measurements. The ID is surrounded by a central solenoid, providing the ID with a central magnetic field of 2 T which will cause the trajectories of even highly energetic particles to bend. There are eight large air-core toroidal magnets, composed of a collection of 25 m long and 5 m wide coils, situated outside the calorimeters and generating the magnetic field for the muon spectrometer. Finally two end-cap toroidal magnets are inserted at each end of the ATLAS detector, and line up with the central solenoid. The toroidal magnetic field is not uniform and varies from around 2 T to 8 T [48].

2.2.2 Inner Detector

The ID is used for precision mass measurements and tracking of charged particles. It is housed in a magnetic field of strength 2 T produced by the superconducting solenoid surrounding it which curves the trajectory of even highly energetic particles so as to measure their momentum. The ID is made up of three different layers of detection: the innermost pixel detector, which is the most accurate and sensitive component of the ID; the Semiconductor Tracker (SCT), which surrounds the pixel detector and provides coverage of a larger area; and the outermost Transition Radiation Tracker (TRT), comprised of straw detectors, all of which are depicted in Figure 13. These trackers produce high precision measurements of tracks in order to deal with the high track density at the ID. The detector traces the tracks of charged particles and is designed in such a way as to minimize material impedance of the tracks.

The pixel detector: The pixel detector [50, 51] is comprised of an arrangement of module units. All modules are identical rectangular devices, which are approximately 6 cm by 2 cm with 46,080 pixels. There are 1456 modules arranged in three concentric cylinders with the axis along the beam, while another 288 modules are arranged normal to the beam pipe, in disks lying on the outskirts of the pixel detector, providing a coverage of $|\eta| < 2.5$. The barrel modules are arranged in such a way as to slightly overlap each other, hence ensuring the barrel has no gaps. Due to the three concentric barrels, and three disks on either side of the barrel, each track generally crosses three pixel layers. The obvious exceptions are low-energy particles which spiral inside the ID due to the strong magnetic field, and are generally of no interest to the experiment and hence discarded from measurement. In order to resolve incoming data

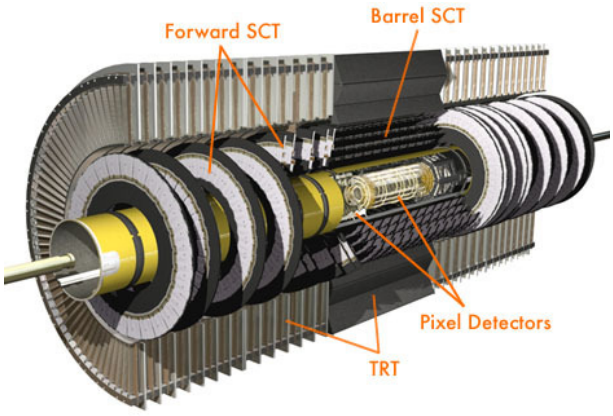


Figure 13: Cut-away view of the ATLAS inner detector. Shown are the constituent sub detectors: the pixel detector, barrel and end-cap SCT, and the TRT [49].

at high luminosity and collision rate ($\approx$ 40 MHz), every pixel has a dedicated electronics channel, which in total make 67 million channels for the barrel, and 13 million for the disc [48].

The semi-conductor tracker: The SCT is similar to the pixel detector, but instead of pixels, the SCT uses long silicon substrate strips to take readings, which allows the coverage of a much wider area than what is available with the pixels [48]. Silicon microstrip detectors where developed in the 1980s and are based on a silicon wafer around 100 μm thick, with a surface area of a few square centimeters. A charged particle crossing through a strip produces electron-hole pairs which are collected by the readout strips [1]. In the SCT the strips are single sided with a dimension of 6.36×6.40 cm^2. Two such strips are wire-bonded together to make a 128 mm long strip. Two long strips are attached back to back with a slight angle offset. A single SCT module is therefore a double sided sensor with a surface area of 6.36 cm by 128 mm. Each silicon module has 768 readout strips producing a total of $\approx$ 6.2 million channels in the SCT. Similar to the pixel detector, there is a barrel section along the beam pipe, and two end-cap sections perpendicular to the beam. The barrel section consists of eight layers (four double-sided cylinders) of silicon microstrip detectors, slightly tilted to provide a measurement of the z coordinate. The barrel modules are mounted on carbon-fibre cylinders at radii of 30.0, 37.3, 44.7, and 52.0 cm, generally providing eight readings per track. The end-cap region is made up of discs of thin barrel modules. In contrast to the pixel detector, the SCT covers a wider area, but at a lower resolution, due to fewer channels which cover a larger volume, and tracks can only be distinguished if they are separated by around 200 μm. Readings in the SCT contribute to the measurements of momentum, impact parameter and vertex position.

The transition radiation tracker: The TRT [48] comprises the outermost component of the ID and is made up of straw detectors, each filled with a non-flammable gas mixture of 70% Xenon, 27% carbon dioxide and 10% Oxygen, with a total volume of 3 m^2. Each straw works as an ionization detector, comprised of two electrodes within a gaseous substance, and provides a measurement of the relativistic factor $\beta\gamma$ of a charged particle, and hence a particle's velocity [1]. The straw detectors are able to operate at the high rates at the LHC due to their small 4 mm diameter and the isolation of a gold-plated W-Re sense wire housed within the individual gas volumes. By virtue of the Xenon within them, the straw detectors have an added electron identification capability by detecting transition-radiation photons created in a radiator between the straws. There are 50 000 straws making up the barrel region of the TRT. Each of these straws is divided in two at it's center and are read out at either end. In addition, there are 320 000 radial straws in the end-cap region, resulting in a total of 420 000 readout channels. In the barrel

region individual modules are made up of between 329 and 793 individual straws, depending on where the module is situated in the TRT.

2.2.3 Calorimeters

In particle physics energy measurements of particles are performed by devices known as calorimeters. Measurements are performed by stopping incoming particles in a material so as to release the energy carried by the particles. There are two types of calorimeters, both of which are present in ATLAS: the inner EM and the outer hadronic calorimeters. The EM calorimeter covers the pseudorapidity of $|\eta| < 3.2$. The hadronic calorimeter has a barrel section covering $|\eta| < 1.7$, and two end-cap calorimeters covering $1.5 < |\eta| < 3.2$. Forward calorimeters cover $3.1 < |\eta| < 4.9$ [48].

Electromagnetic calorimetry: Electrons, positrons and photons produce EM showers in a material [1] via bremsstrahlung

$$e^{\pm} + N \rightarrow e^{\pm} + N + \gamma \tag{13}$$

and electron-positron pair production

$$\gamma + N \rightarrow e^{+} + e^{-} + N. \tag{14}$$

The EM calorimeter forces these charged particles transversing it to interact with electrons in the material and produce secondary particles. This produces a chain effect where the secondary particles subsequently decay. The average distance between decays is given by the radiation length in a material, X_0 [1]. For the first part of an EM shower, the number of electrons, protons and photons increases. This increase occurs until the average energy of individual particles decreases to the point that they can no longer decay. When this occurs, the number of particles begins to decrease. Thus an effective calorimeter needs to be several X_0 lengths thick. A schematic representation of an EM shower stemming from an energetic photon is shown in Figure 14. An incoming γ will decay almost immediately through Equation 14, while a $e^{\pm}$ will survive an approximate length of X_0 before undergoing the process of Equation 13, providing a way of distinguishing $e^{\pm}$ and γ particles. The EM calorimeter in ATLAS is a lead liquid Argon (LAr) 'sampling' type of detector. This means that it is comprised of absorbing layers of lead, which initiate particle showers, alternated by layers of a sampling material. In said case, the sampling material is LAr and is ionized by the decay particles [1, 48]. The particle showers are detected in the sampling material by using a strong electric field. The position and energy of a particle shower can thus be determined. Since energy is absorbed by the lead layers, a certain amount of energy is not detected by the EM calorimeter. More energetic particles spend less time in the lead layers than less energetic particles. As a result, the energy resolution of the detector $\sigma(E)$ is proportional to $\sqrt{E}$. The EM calorimeter uses accordion shaped Kapton electrodes to detect ionization of the LAr. The calorimeter is divided into a barrel part covering $|\eta| < 1.48$, and two end-caps covering $1.38 < |\eta| < 3.2$, the total thickness of which covers $> 24\,X_0$ in the barrel, and $> 26\,X_0$ in the end-caps [48].

Hadronic calorimetry: Hadronic calorimetry is essential for the measurement of hardons, or hadronic groups of particles. In high-energy collisions quarks appear as hadronic jets, which are groups of hadrons travelling in a narrow cone. Furthermore, reconstruction of tau leptons in ATLAS can only effectively be done by the identification of their hadronic decays. This will be described in detail in the later Section 2.4. This makes hadronic calorimetry a vital component for studying heavy flavour physics. Hadronic calorimetry in the ATLAS detector is divided into two regions, one that uses tile calorimeters in the barrel region, and LAr calorimeters at large pseudorapidities, for which higher radiation resistance is needed [48]. The ATLAS hadronic calorimeters cover a large range of $|\eta| < 4.9$, where the tile calorimeter covers $|\eta| < 1.7$, while the LAr calorimeter covers $1.5 < |\eta| < 4.9$. The tile calorimeter is

also a 'sampling' detector, comprised of steel as the absorption material, and plastic scintillator tiles as the active material. The scintillators are made up of transparent plastic slabs, doped with particles that emit light when an ionizing particle passes through them. The light is directed to a photocathode where it can be detected [1]. The LAr hadronic calorimeter is further divided into two components: the Hadronic End-cap Calorimeter (HEC) extends to $|\eta| < 3.2$, while the range $3.1 < |\eta| < 4.9$ is covered by the Forward Calorimeter (FCAL). Of particular importance to the ATLAS design was the thickness of the calorimeters, allowing for good hadronic containment, and minimizing the punch-through to the muon chambers. The total thickness is 11 interaction lengths (λ), while 10 λ of calorimetry is sufficiently adequate for providing good resolution of high-energy jets and, by extension, good E_T^{miss} measurements [48].

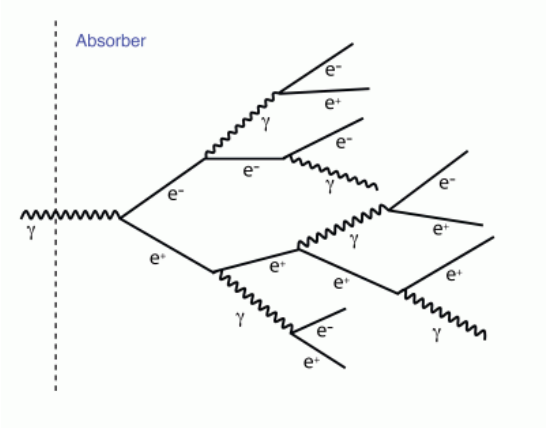


Figure 14: Schematic representation of the EM shower of an energetic photon in an absorbing material [52].

2.2.4 Muon Spectrometer

Due to the high design λ and X_0 lengths of the EM and hadronic calorimeters, most particles are stopped at calorimetry. Particles which do not interact with either the EM or hadron calorimeters pass into the muon spectrometer. Muons are relatively stable particles inside the detector and will generally pass through the calorimeter section. Muons do not feel the strong force and only interact weakly with nuclei. They are also too large to interact by ionization, and are hence not picked up by the calorimeters. The muon spectrometer [48] covers a total pseudorapidity of $|\eta| < 2.7$, with a small opening in the central R-ϕ plane ($\eta = 0$) feeding cables to the inner components of the detector. Once in the muon spectrometer, a muon is deflected by the magnetic field from the toroidal magnets, mostly orthogonal to the muon trajectory, providing a method for measuring its momentum identical to the one described in the ID. For the most part this deflection is measured in the drift chambers, comprised of aluminum tubes filled with a non-flammable gas mixture of 93% Argon and 7% carbon dioxide. Each tube has a diameter of 30 mm and wall thickness of 400 mm, with a 50 mm diameter central W-Re wire. Like the TRT straw detectors described in Section 2.2.2, the aluminum tubes are ionization detectors. At large pseudorapidities cathode strip chambers, which are multi-wire chambers with a cathode strip readout and with a symmetric cell, offer a higher granularity measurement than that of the drift chambers. They are used in the innermost plane, over $2 < |\eta| < 2.7$. The resistive plate chambers are gaseous detectors in the barrel region. Thin gap chambers, which are similar to the cathode strip chambers in the end-cap regions, serve as triggering detectors of muons and cover a total range of $|\eta| < 2.4$.

2.2.5 Trigger System

A triggering system is vital for data acquisition and analysis at ATLAS, as the large number of interactions in the detector create a large rate of data. ATLAS uses a three-level online event selection system of triggering to identify and discard all unnecessary data from reconstruction by searching for potentially interesting events [48]. The design crossing rate of 40 MHz, resulting in $\approx$ 25 proton-proton interactions per bunch crossing, is reduced to only 200 Hz for storage and analysis [44]. The trigger system is comprised of three levels of event selection: Level 1 (L1) which is hardware based; and Level 2 (L2) and Event Filter (EF), which together are referred to as the High Level Trigger (HLT) and are software and algorithm based. A schematic representation of the ATLAS trigger system is given in Figure 15, with an overview description of each trigger level given below.

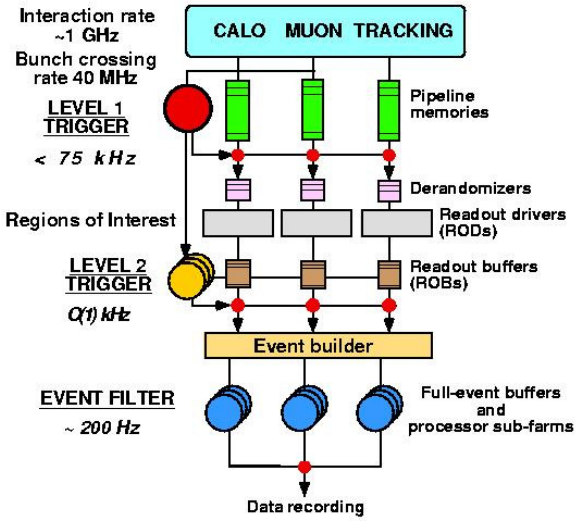


Figure 15: Schematic representation of the ATLAS trigger system, showing the three stages of triggering: L1, L2 and EF [48].

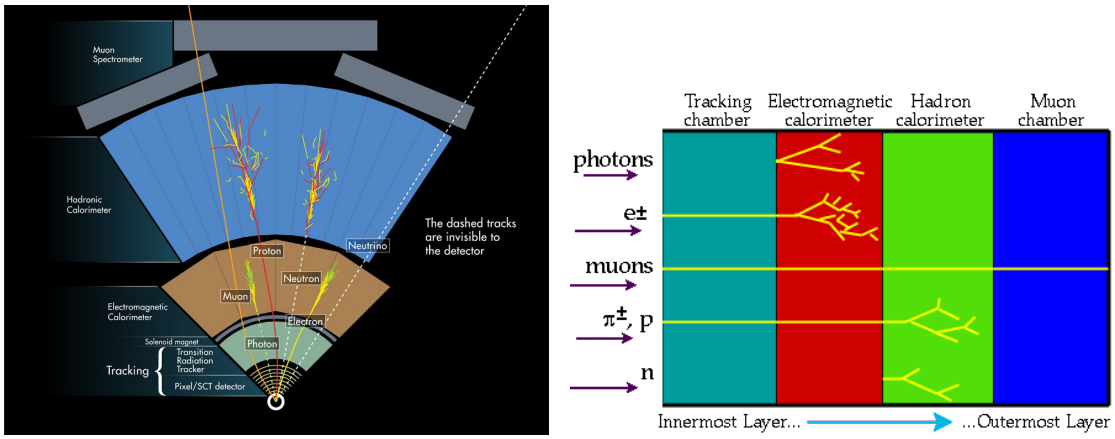
Level 1: The L1 trigger receives data at the full 40 MHz bunch crossing rate, and reduces it to an output rate of around 75 kHz [44]. It makes decisions based on the data coming from the calorimeter and muon detectors. The L1 constructs objects from the LAr and tile calorimeters, including EM clusters, taus, jets, E_T^{miss}, the scalar sum E_T (ΣE_T) in the calorimeter, and the total transverse energy of observed L1 jets. Various energy and jet multiplicity criteria are applied to these objects. L1 triggers on muons based on the multiplicity for various p_T thresholds, seeded by the resistive plate and the thin gap chambers explained in Section 2.2.4.

Level 2: The L2 trigger is algorithm based, running on dedicated PC farms. L2 is seeded by an L1 candidate consisting of the L1 object's p_T threshold and η and ϕ coordinates. From this seed the L2 algorithms construct a region of interest (RoI) around the object, whose size depends on the triggered object (*e.g.* electron triggers use smaller RoIs than jets) [44]. Only the data local to a RoI is analyzed by the L2 trigger, reducing computation time, as well as bandwidth. Using a richer amount of information than was available at L1, the L2 trigger provides an additional event rejection of a higher quality. Included in the L2 are reconstructed tracks from the ID. For each L1 RoI a sequence of L2 algorithms compute quantities which are passed through a stringent set of selection criteria, reducing the output rate to around 2 kHz.

Event Filter: The EF is the final online selection applied in the triggering system. It boasts direct use of the complete data for a given event, as it is performed after an event building step [44]. The EF algorithms are generally more time consuming, $\approx$ 4s per event, than those in L2 which, where particularly optimized for timing performance. This added computation time is used for stringent event selection. The EF is seeded by events surviving the L2 trigger and reduces the input rate of 2 kHz to around 200 Hz, corresponding to around 300 Mb/s.

2.2.6 Overview of object reconstruction

The ATLAS detector, it's components and their functions were described extensively in Section 2.2. As explained above, ATLAS has a complex array of sub detectors used to identify and reconstruct the particles, and decay daughter particles, stemming from high energy pp collisions at the interaction point. The purpose of the ID (Section 2.2.2) is to track the trajectories of charged particles, which are bent by a solenoid magnet, thereby determining their mass, velocity and momentum. EM calorimetry (Section 2.2.3) serves as a tool to determine the energy of EM particles, photons, electrons, and positrons. Hadronic calorimetry (Section 2.2.3) is used to determine the energy, as well as identify hadrons. Typically the hadronic calorimeter identifies neutral hadrons, like neutrons which will leave no tracks in the ID, and charged hadrons, such as $\pi^{\pm}$ and protons, matching tracks in the ID. Elusive muons will pass through calorimetry, depositing charged tracks in all stages of the detector, and are measured by the muon spectrometer (Section 2.2.4) which is under a large magnetic field from the toroidal magnets. Weakly interacting neutrinos are capable of passing through the entire Earth without interacting with anything, and can only be observed by ATLAS as E_T^{miss}. A dedicated trigger system (Section 2.2.5) selects physically interesting events from a large rate of incoming data. An overview of different particle trajectories, and their expected interactions with ATLAS, is shown in Figure 16.



(a) (b)

Figure 16: Representation of different particle paths throughout the layers of the ATLAS detector shown (a) with a cross section view, and (b) schematically [49].

2.3 The ATLAS computing model

The ATLAS collaboration has developed a wide set of software and middleware tools which provide access to data to all members of the collaboration in sites all over the world. Software on the user end provides functionality at various stages of the data or Monte Carlo (MC) production at ATLAS. To this end, various formats of data and MC simulation are used in order to distinguish different stages

in the production. The Worldwide LHC Computing Grid, a grid-based computer network comprised of a large collaboration of servers around the world, is used for storing the large amounts of data, as well as providing the CPU for running analysis algorithms at various stages of data production. The ATLAS computing grid, along with it's structure and functions, will be discussed in Section 2.3.1. An integrated analysis tool called ATHENA which is comprised of hundreds of packages, providing tools for processing and analyzing data, is discussed in Section 2.3.2. In Section 2.3.3 we discuss the framework used for simulating events in ATLAS.

2.3.1 The computing grid

The ATLAS Experiment makes use of CERN's WLCG, a grid system of servers and individual PCs located at various computing facilities across the world, which offers a high degree of decentralization, and ample sharing of computing resources [53]. A hierarchy system of the different computing facilities is imposed since different facilities are better apt to undertake certain computing responsibilities. This should not detract from the fact that all stages of data production are vital, and lower ranked sites still provide an invaluable resource. The hierarchical system is split into four levels, ranging from the Tier-0 facility, an on-site server which receives data right after triggering (Section 2.2.5), to Tier-3 facilities, with dedicated local storage and available CPU. The different Tiers and their functions are described below.

Tier-0: The Tier-0 site is located at the CERN site in Geneva. This is where the primary event processing occurs. After surviving the final stage of HLT, known as the Event Filter (Section 2.2.5), events are archived as RAW data in Tier-0 sites [53]. Raw data arrives at the rate of 200 Hz, and has an event size of $\approx$ 1.6 MB. It is stored in a byte-stream format, reflecting the data produced in the detector, and has no object-oriented representation. Each RAW file contains the events from a single run. The Tier-0 facility at CERN is used for fast data reconstruction along with prompt data calibration and data quality [54]. A first round of processing is conducted on RAW data, producing derived datasets which are distributed to Tier-1 sites. These are the Event Summary Data (ESD), Analysis Object Data (AOD) and Tag Data (TAG) formats described in detail below. Some promptly reconstructed AOD files are also stored along with RAW data. Access to Tier-0 is generally restricted and only available to people working in the central production group or those providing first-pass calibration [53].

Tier-1: After RAW data is archived at Tier-0, it is distributed equally to the Tier-1 facilities. They provide additional long term storage and access to the RAW data. They also provide a back up for first-pass processing and calibration in the event of prolonged downtime of Tier-0 [53]. Refined reconstruction and alignment is run at Tier-1 and saved as derived datasets of the original RAW data. Access to derived ESD, AOD and TAG datasets are available to the ATLAS collaboration from these Tier-1 sites, and are also distributed to Tier-2 sites. Furthermore, CPU is available at Tier-1 sites for users to run their analysis code. ATLAS has incorporated a framework which works on the principle that analysis algorithms, or 'jobs', should be sent to the computers where the data is stored, and run on the server side. The output can then be downloaded to a local directory. The alternative would be for users to download data and run their jobs locally, which would produce a vast duplication of datasets, not to mention waste valuable bandwidth and time. ESD files are duplicated in at least two Tier-1 sites at any given time, reducing the reliance on any one site. The ESD files are derived from RAW data. The full output from reconstruction is contained in an ESD, including tracks, calorimeter clusters, calorimeter cells, combined reconstructed objects, *etc.*. While some tasks, such as re-reconstruction and changes in calibration, can only be done on RAW data, the ESD format is intended to replace RAW data for most physics applications. ESD has an object-oriented representation, and is stored in POOL ROOT files. They are made up of $<$ 1 MB per event. On the other hand TAG data is around 100 kB per event, and provides event-level metadata which

is used for identifying and selecting individual events.

Tier-2: The Tier-2 sites store various versions of ESD, AOD and Derived Physical Data (D3PD) data. Dedicated CPUs are available at these sites so that users may run jobs on the desired dataset. Tier-2 sites store various versions of AOD files. AOD is a reduced event representation derived from ESD and is used for physics analysis. It contains reconstructed physics objects, such as electrons, muons, jets, *etc.*, as well as other physics-related information. An AOD event is stored in < 1 MB. The D3PD format is a largely reduced format. It is derived from the AOD and boasts around 10 kB per event after reducing the AOD via skimming, slimming and trimming. D3PDs are small and easy to work with, and can be read by the ROOT infrastructure [55, 56]. ROOT is a library of C++ classes providing functionality for data analysis; it includes data display, persistency, minimization, fundamental classes, *etc.*.

Tier-3: Tier-3 sites offer users access to the grid. They provide users with local storage space. They also contribute their CPU to MC production when available.

2.3.2 The ATHENA framework

ATLAS uses a common event processing framework based on plug-compatible components and abstract interfaces called "The Athena Framework", or ATHENA [53]. Athena is an object orientated control framework written in an object orientated programming language known as C++, with some components using FORTRAN, Java and Python. ATHENA is based on the Gaudi framework, originally developed by LHCb [57, 58]. The Gaudi project is a kernel which is now supported by both experiments, while ATHENA is the combination of the Gaudi kernel and ATLAS specific enhancements [59]. The architecture consists of a handful of core packages and is supplemented by external libraries such as Geant.

The main function of ATHENA is to provide a common development and user framework which supports the offline operation of the ATLAS experiment. This encapsulates a broad range of functionality, from providing software for object reconstruction, detector alignment and simulation, and simulating MC events, to providing an end user with tools for physics analysis. ATHENA does this by providing a set of software tools which are used for offline analysis. The entire ATLAS offline software framework is organized hierarchically into a structure of projects and packages. The main projects are listed below in order of hierarchy [59]:

- **AtlasCore** This project contains the core components of ATHENA, being the Gaudi architecture and ATLAS specific packages. All other projects are AtlasCore dependant.
- **AtlasConditions** Is dependant on AtlasCore. This project contains information on the ATLAS detector's conditions, geometry and calibration.
- **AtlasEvent** This project is dependant in AtlasConditions. It contains the Event Data Model (EDM) comprised of classes for defining the RAW, ESD, AOD *etc.* data structures. It supports both AtlasReconstruction and AtlasSimulation projects directly.
- **AtlasSimulation** Contains all tools, algorithms and services related to simulation. This includes the Geant4 simulation, physics generators, pile-up and digitization tools, *etc.*.
- **AtlasReconstruction** Contains tools, algorithms and services for reconstruction and fast simulation.
- **AtlasTrigger** Dependant on AtlasReconstruction. It contains all tools, algorithms and services related to the HLT.

- **AtlasAnalysis** Dependant on AtlasTrigger. It provides tools, algorithms and services related to physics analysis, monitoring and event display.
- **AtlasOffine** The AtlasOffline project is dependant on both the AtlasAnalysis and AtlasSimulation projects. It is used as a placeholder project where bug fixes can be explored and implemented.
- **AtlasProduction** This is the top level project and depends on all other projects. This final project dedicated to an official release of ATHENA.

Each of these projects has various packages, most of which are divided further into sub-packages, which are updated regularly and distinguished by different tags for the different versions. A given package in ATHENA is organized into several sub-directories, not all of which are necessary [59]:

- **cmt** In this folder the Configuration Management Tool (CMT) is used to set up and build the code in the package. A requirements file contains the package dependencies.
- **PackageName** The folder generally stores all the header files of the C++ code. Files are of *.h extension.
- **src** Here you find the source code of the package, written in C++. Files are of *.cxx extension.
- **share** The share directory contains any job options files (described below).
- **run** A directory where jobs can be run, particularly used for testing the code on individual samples.
- **python** Any necessary Python scripts may be stored here.

Packages are updated frequently by their developers so as to implement changes and bug fixes. The packages are saved with a specific tag so as to distinguish between the different version. All tags are stored using the Apache Subversion (SVN) system which archives different versions of source code. This allows users to revert back to previous changes, and also allows backwards compatibility to previous ATHENA releases.

Due to the continuous nature of updates to the ATLAS software framework the entire software is released with a unique release number [59]. The release number consists of three numbers, separated by dots. At the time of writing, the most recent release of ATHENA available is 19.2.0. The number 19 refers to the major ATHENA release. The second number (2) indicates a specific branching, while the third number indicates minor changes. There are sometimes patches to a release, which fix minor bugs, *e.g.* 19.2.0.1 is a patched version of 19.2.0. Although the release of new production releases only occur every few months, releases are built nightly to provide developers with the most up to date release. Nightlies are built every day, with rel-0 built on Sundays, and rel-6 on Saturdays. An example of a nightly release is 19.2.0.1, rel-4.

Athena uses Python as an object-orientated scripting and interpreter language to configure and load the C++ algorithms from the packages described above. Control of the run-time configuration of a package, or packages, are handled by job options files which are Python scripts which can be run using ATHENA [59]. Job options files give the user control over several run-time functionalities. These include the message output level, which prints different degrees of text which is used for debugging purposes; the number of events to be processed; the input files to be used in run-time; the objects to be saved, as well as the format and output file names, *etc.*. Job options files can be run locally in the desired version of ATHENA on local data. The beauty of a job options file is that the same set-up used locally can be

sent to the ATLAS grid described in Section 2.3.1, where the algorithms can be run over huge volumes of datasets. This is done by using a framework called pATHENA, a combination of ATHENA though a grid job submission client which organizes the jobs sent to the grid. pATHENA functions by sending the jobs to the grid sites where the datasets are available. This procedure is conducted in Tau Validation, and examples will be given in Section 3.

2.3.3 Simulated data and Monte Carlo production

The success of the ATLAS Experiment is heavily reliant on the effective simulation of the detector's response to physics processes and scenarios. The simulation of physics processes stemming from high energy collisions is done on an event-by-event basis and is performed predominantly at Tier-2 sites. The fallout of said events is modeled through the detector. The simulation output is delivered in a format identical to that of the true detector. This allows for both simulated and real data to be run through the the same trigger and reconstruction packages. The process of simulation in ATLAS can therefore be divided into three steps: generation of an event and it's immediate decays; simulation of the detector and the physics interactions within the detector; and the digitization of energy deposits in the detector, into voltages and currents which mimic the output of the true detector [60]. These three stages are discussed in detail below.

Event generation: The generation of events consists of the production of a set of particles which are later passed through full or fast detector simulation. In ATLAS the generation is done through the ATHENA framework, driven by MC generators. There are many generators to choose from. All the generators rely on large repositories of Parton Distribution Functions (PDFs) as part of their input. The PDFs describe the substructure of a proton in a collision. A generator is responsible for simulating prompt decays, such as those from Z and W bosons which have lifetimes of $c\tau < 10$ mm. Particles within this range are considered unstable since they usually decay before reaching the detector. The generator also stores stable particles ($c\tau > 10$ mm) but leaves their decay to the detector simulation [60].

The MC generators: The event generators available to ATLAS have their own weaknesses and strong points. Deciding on which generator to use depends on the type of process that one wishes to study. Generators used for general large-scale production of events include Pythia [61], PythiaB [62] (for events with b-quark jets), Herwig [63], Sherpa [64], Hijing [65], Alpgen [66], MC@NLO [67] and AcerMC [68]. Tauola [69] is used for generating events with tau decays. Photos [70] is used for photon emissions. EvtGen [71] is used for more detailed studies of b-jet decays. Phytia8 [72] and Herwig++ [73] are the newer multipurpose C++ generators. The total list of generators is not exhausted here [60].

Detector modelling with Geant4: The simulation of the particles from the event generation is passed though a simulation of the ATLAS detector. The standard simulation relies on the Geant4 particle simulator toolkit [74]. Geant4 is able to the model physics processes related to particles passing through matter with applications going beyond experimental particle physics. To name a few, it has been used to determine radiation dose due to the deposition of charged particles (particularly protons) [75] and for microdosimetry purposes of internalized and non-internalized radionuclides [76]. The detector's configuration, including misalignments and distortions, are fed into Geant4 by the user, and each generated particle is allowed to propagate though the detector simulation. Each event can take several minutes to simulate. Around 80% of this time is spent on the simulation of particles decaying in the calorimeter, where a dense population of particle showers will show up. Up to 75% of the time is spent just simulating EM particles. An alternate fast-simulation method is available for studies which do not require extensive information of processes in the calorimeter. It replaces the simulation of low-energy EM showers in the calorimeter with pre-simulated showers reducing the total computation time by a factor of three [60].

Energy deposits in the detector simulation are recorded as hits, containing the total energy deposited, its position and time. The simulation output is written to a HITS file format. The format contains metadata about the detector configuration and simulation. They also contain truth information which is described below.

Truth information: In both the event generation and detector simulation truth information of the event is stored [60]. The truth information consists of the information of the true underlying process which was generated. The goodness of the information is directly related to the goodness of the underlying physics model. In the event generation truth information contains the history of the incoming and outgoing particles of the interaction. All particles generated are stored. In the simulation stage the truth information of physically interesting particles are stored. This consists of the true particle tracks and decay products. Truth information provides many uses. It can be used as an effective test of a models proficiency to model the real world phenomena. In certain cases it is used to formulate physics analysis strategies, and is used to calculate effective background estimations. Furthermore, comparing truth information to simulated reconstructed objects allows for a quantification of object reconstruction efficiencies. The MC truth information makes up a large fraction of the total simulated event ($\approx 30\%$). Since real data contains no truth information, the file size of MC simulation per event is much larger.

Digitization: Digitization take the HITS files as input and converts it to detector responses, or 'digits'. A digit is typically produced when the voltage or current of a read out channel in the detector spikes above a set threshold. During the digitization stage one may choose to recreate the pile-up conditions associated to a certain instantaneous luminosity. Pile-up involves the overlay of events at a user defined rate mimicking that of the required luminosity. Detector noise is added to the event at this stage. After this the L1 trigger is applied and each trigger hypothesis is evaluated. The digits are constructed and passed though emulated Read Out Drivers (RODs), see Figure 15. The data is output in the Raw Data Object (RDO) format. This format is similar to the byte-stream RAW format referred to in Section 2.3.1 with the main exception that it contains truth information. The HLT and reconstruction can then be run on these RDO files.

2.3.4 Software development for Run-II

In Run-I ATLAS followed a rigid Tier-0 policy to ensure the stability and reproducibility of data [54]. This however resulted in an accumulation of outdated Tier-0 AODs, which did not reflect the most up to date understanding of the detector and physics. Physics and performance groups in ATLAS would therefore have to apply the latest fixes to the AODs, creating their own private datasets for further analysis. Furthermore, since the AOD format is not readable by ROOT, most groups would create large private datasets in the D3PD format for the group members to use. Due to the obvious wastefulness of this procedure the structure of the EDM that would be used for Run-II was reviewed and redesigned. In Run-II the AOD format is replaced by a new data format named xAOD. The xAOD format is both readable by ATHENA and ROOT, allowing for both high level reconstruction and access to the full list of objects. Run-II will permit the reprocessing of Tier-0 xAOD datasets with updated detector calibrations and reconstruction algorithms, proving centralized updates to the xAODs. ATHENA is being updated to take full advantage of xAODs by developing and migrating analysis projects and tools to facilitate the xAOD format. The tools that run on xAODs will be fully integrated and distributed into ATHENA.

2.3.5 Physics Validation

As described in Section 2.3.2, new releases of ATHENA are constantly distributed to WLCG sites. Before the release becomes available for mass MC production the new release needs to be tested for consis-

tency, so as to verify that no bugs have crept into the reconstruction during changes to the code. This step is called Physics Validation. The Physics Validation group is a dedicated group of experts comprised of representatives from every detector performance (*e.g.* trigger, b-tagging and jet-reconstruction groups) and physics (*e.g.* SM, supersymmetry, *etc.*) group in ATLAS [60]. Whenever a new release is distributed, a set of validation samples are produced which include around 1 400 000 events and 250 000 particles per process. The Physics Validation group's task is to verify the quality of individual object reconstruction (*e.g.* electrons, muons, jets, taus, *etc.*) and more complex reconstructions (*e.g.* $Z \to e^+e^-$,$Z \to \mu^+\mu^-$, *etc.*). The samples are generally compared to samples which where produced with ATHENA releases that have been previously evaluated. During my research I directly contributed to updating and running the validation software for reconstructed tau leptons. This included performing validations of numerous tasks for a period extending over two years. The validation code was updated by myself in order to run on the new ATHENA frameworks which are being developed for Run-II.

The validation procedure is as follows:

- A request is made by Simulation, Reconstruction, Data Preparation or MC Production coordinators for a new cache / configuration that needs to be checked. The following configuration is specified in the request: the release cache, geometry, conditions tag, trigger menu and any other specific option needed for the production of the samples.
- A new set of validation samples are produced for the requested configuration. If the validation is testing simulation, new samples are simulated and reconstructed. For a digitization and reconstruction cache only the reconstruction of the cache will be needed.
- Information about the validation samples, including the samples which one needs to compare to, are circulated to the validation group. The Physics Validation contacts will run their analysis code and produce histograms comparing the distributions of the test and reference samples. The results are discussed in a meeting two to three days after the information has been distributed.
- If problems are found they are reported to the developers or release experts and followed up by the validation groups.

Due to the large number of events in the validation samples, Physics Validation exposes minor problems which might not be found with smaller samples, such as a shift of a few percent of an object's reconstructed energy.

2.4 Tau lepton reconstruction in ATLAS

Tau leptons serve as an important constituent in many topologies which are part of the searches performed in ATLAS, including searches such as $H \to \tau^+\tau^-$ [77] and $H^\pm \to \tau^\pm\nu$ [78]. Tau leptons are massive particles and have a short lifetime of $c\tau = 87.11\,\mu$m. In turn they offer a way to measure the polarization, spin and parity of the resonances that produce them, making tau leptons an invaluable tool in particle physics research [44]. The range of interest of the transverse momentum of tau leptons at the LHC is large, from below 10 GeV to approximately 500 GeV, where the lower energies are related to the W and Z boson observability with tau decays, and also to Higgs boson searches and SUSY decays. The higher energy range is mostly of interest in searches for heavy Higgs bosons in MSSM models and for extra heavy W and Z gauge bosons [44]. In this thesis tau leptons play an important role in the $A \to Zh \to \ell\ell\tau\tau$ analysis. The reconstruction of tau leptons is discussed in this section. The validation of tau lepton reconstruction in MC production is discussed in Section 3.

2.4.1 Tau characteristics

Due to their tiny lifetime tau leptons decay before ever reaching the ATLAS detector and must be reconstructed from their decay products. Tau leptons are the only leptons with a mass large enough to decay into composite particles, hence they undergo either hadronic (τ_{had}) or leptonic (τ_{lep}) decay. However one only considers hadronically decaying taus when talking about tau reconstruction in ATLAS, as leptonically decaying taus are very difficult to distinguish from electrons and muons stemming from different processes [44]. Leptonic τ-decay occurs in the $\tau \to \ell\, \bar{\nu}_\ell \nu_\tau$ and $\tau \to \ell\, \bar{\nu}_\ell \nu_\tau \gamma$ channels, where $\ell = e$ or μ [20]. Tau leptons will undergo leptonic decay at a rate of approximately 17.41% for muons and 19.58% for electrons. Hadronic τ-lepton decay occurs at a rate of 64.8% and has a characteristic 1-prong[1] (one charged π) or 3-prong (three charged πs) signature[2]. Hadronic τ-lepton decays, with one charged π, occur in the channels $\tau \to \pi^{\pm}\upsilon$ (22.4%) and $\tau \to n\pi^0\pi^{\pm}\upsilon$ (73.5%), while decays with three charged πs occur as $\tau \to 3\pi^{\pm}\upsilon$ (61.6%) and $\tau \to n\pi^0 3\pi^{\pm}\upsilon$ (33.7%) [44]. The 1- and 3-prong channels are therefore dominated by $\pi^{\pm}$ and π^0, plus a small percent of $K^{\pm}$ detected by the same techniques used to detect pions. A schematic representation of the tau decay modes is shown in Figure 17. The τ-lepton's lifetime is in principle long enough to reconstruct a 3-prong decay vertex in the ATLAS detector, and the neutral pions decay immediately into a di-photon pair which eventually convert inside the calorimeter. To summarize, when searching for tau leptons in ATLAS, we search for collimated low multiplicity (1 or 3 tracks in the ID) jets with energy deposits in the EM and hadronic calorimeters. These are known as tau jets (τ-jet).

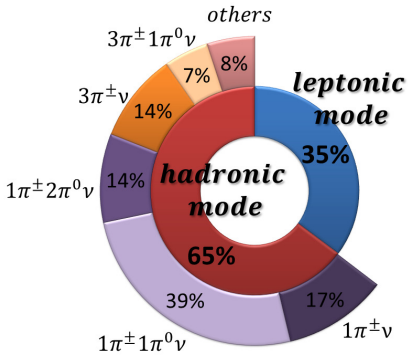


Figure 17: Schematic representation of the brake-down of leptonic and hadronic tau decay modes [79].

2.4.2 Tau reconstruction

Since tau reconstruction is focused around reconstructing and identifying hadronic tau decay products, it is particularly difficult to distinguish from background processes dominated by QCD multi-jet production, which produce tau like tracks in the ID and clusters in the calorimeter. However, we are able to make use of some properties of tau decays which are almost unique to tau leptons. The main way in which hadronic τ-leptons can be distinguished from QCD jets is by their 1- or 3-track multiplicity in narrow cones. Figure 18 shows the difference between a tau jet, with low track multiplicity, and a jet of hadrons coming from a background event. The tracks in the ID, and clusters in the calorimeter need to be isolated from the rest of the event for a jet to be considered for tau reconstruction. In addition, certain characteristics of the track systems, as well as the shape of the calorimeter showers provide insight on whether or not the reconstructed object is a tau [44]. A set of identification variables have been

[1]The prong number refers to the number of charged particle tracks found from the same vertex in the detector.
[2]The 5-prong channel only occurs 0.1% of the time and is not reconstructed by ATLAS since it is difficult to identify.

constructed from these criteria, to which either cut-based or multi-variate discrimination techniques are applied to select the tau lepton candidates.

The information of a tau lepton candidate is supplied by the ID, and the EM and hadronic calorimeters. The ID provides information about the charged track, or collimated multi-track systems. These tracks cannot match tracks in the muon spectrometer, nor have features which are characteristic to electron tracks (*e.g.* having many hits in the TRT). Multi-track systems in the ID need to be well grouped in η and ϕ and have an invariant mass smaller than that of the tau lepton ($m_{\text{tracksys}} < m_{\tau}$). The charge of the individual track(s) will sum up to the charge of the resonant tau lepton(s). Calorimetry, on the other hand, provides information about energy deposits from visible decay products, which is to say excluding neutrinos. Hadronic taus are well collimated producing relatively narrow showers in the EM calorimeter. Tracking and calorimetry information needs to match, such that the clusters are matched to the point of impact of the track to the calorimeter [44].

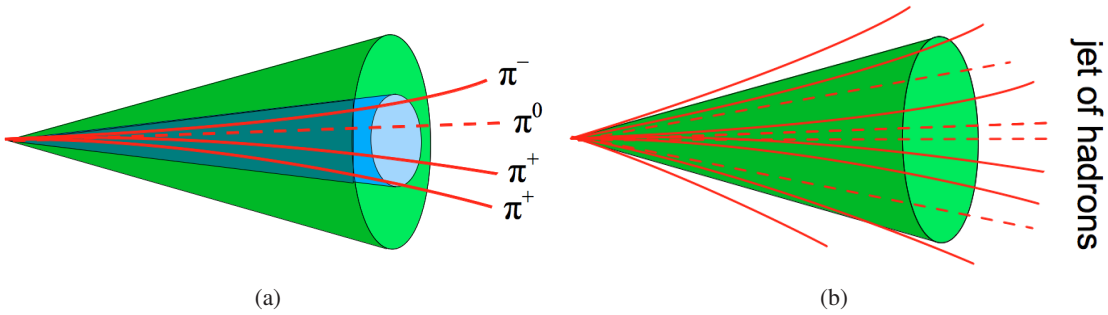


Figure 18: Schematic representations of (a) a hadronically decaying tau jet, and (b) QCD jet [80].

Tau reconstruction algorithms in ATLAS are dependant on algorithms of different subdetectors (*e.g.* track reconstruction in the ID, and topological clustering of energy deposits in the calorimeters), and are therefore considered to be high level reconstruction algorithms. There are two main tau reconstruction methods which evolved into the algorithm used today in ATLAS [44]. One is considered to be calorimeter based (*cellBased*), and the other track based (*eFlowRec*). The *cellBased* algorithm starts by selecting clusters in the calorimeters as tau candidates. These clusters are provided by a sliding window clustering algorithm, which scans for appropriate clusters over the cells of all layers of the calorimeter in a grid the size of $\Delta\eta\times\Delta\phi = 0.1\times 2\pi/64$. A set of identification variables are constructed from tracker and calorimeter information [81]. On the other hand, the *eFlowRec* algorithm starts with a few high quality tracks collimated around a leading track. The energy calculation comes from the tracks and clusters found in the EM calorimeters only. A set of identification variables is constructed from tracker and calorimeter information [82].

For ATLAS 2012 data a single dedicated algorithm, which combines both tracking and calorimeter information, is used for tau reconstruction [83]. In an event all jet-objects reconstructed using the anti-k_t algorithm [84] are considered as $\tau_{\text{had-vis}}$ candidates. These jets are reconstructed from topological clusters [85]. The reconstruction of a topological cluster begins with a seed calorimeter cell, the cluster is constructed by subsequently adding an additional neighboring cell to the cells already in the cluster, with the condition that the energy in the additional cell is above a threshold defined as a function of the expected noise. The jet-objects are required to have $p_T > 10$ GeV and $|\eta| < 2.5$. To compensate for the probability of incorrectly assigning a pile-up vertex as the primary vertex of the $\tau_{\text{had-vis}}$ candidate,

a dedicated vertex association algorithm, known as Tau Jet Vertex Association (TJVA) [86], is used to determine the best vertex hypothesis. This vertex, referred to as the tau vertex, is used as the origin of the co-ordinate system used to calculate the direction of cell- and cluster-based variables. An intermediate axis is recalculated from the tau vertex coordinate system using the four-vectors of all topological clusters which are within $\Delta R := \sqrt{(\Delta\eta)^2 + (\Delta\phi)^2} < 0.2$ of the $\tau_{\text{had-vis}}$ barycenter. The reconstructed four-momentum of the $\tau_{\text{had-vis}}$ candidate is defined in terms of η, ϕ and p_T. The $\tau_{\text{had-vis}}$ mass is chosen as zero, consequently forcing $p_T = E_T$. The list of calorimeter clusters associated to each $\tau_{\text{had-vis}}$ candidate is then refined and used to calculate kinematic quantities [44]. Tracks are associated to the $\tau_{\text{had-vis}}$ candidate if they are within the the core cone, a region within $\Delta R \leq 0.2$ of the intermediate axis. These tracks must satisfy the following quality criteria [83]:

- $p_{\text{T}} \geq 1$ GeV,
- Number of pixel hits ≥ 2,
- Number of pixel + SCT hits ≥ 7,
- $|d_0| \leq 1.0$ mm,
- $|z_0 \sin\theta| \leq 1.5$ mm,

where the impact parameter, d_0, is the distance of closest approach of the track to the tau vertex in the transverse plane, and z_0 is the longitudinal distance of closest approach. The number of tracks counted in the core cone (N_{tracks}) dictates whether the $\tau_{\text{had-vis}}$ candidate will be classified as a single or multi-prong tau. The number of tracks within the isolation annulus ($N^{\text{iso}}_{\text{tracks}}$), a region within $0.2 < \Delta R \leq 0.4$ of the intermediate axis, meeting the same quality criteria mentioned above, are used for variable calculations.

2.4.3 Tau background discrimination

Although the $\tau_{\text{had-vis}}$ reconstruction mentioned in Section 2.4 makes use of the properties inherent of hadronic tau decay, these properties are not unique and provide very little rejection from jet background. In order to adequately reject backgrounds we make use of an additional identification step, which makes use of a number of discriminating variables which are provided from the $\tau_{\text{had-vis}}$ reconstruction. These variables are used for either cut-based (Boosted Decision Trees (BDT)) or or multi-variate (Projective Likelihood (LLH)) discrimination. Three working points (loose, medium and tight) are defined, corresponding to target efficiencies of 70%, 60% and 40% for 1-prong and 65%, 55% and 35% for multi-prong $\tau_{\text{had-vis}}$ candidates, respectively [83]. This corresponds to a loose selection containing a large amount of $\tau_{\text{had-vis}}$ candidates, but allowing a large amount of fake background to be selected. On the other hand, a tight selection has a smaller $\tau_{\text{had-vis}}$ efficiency, but discriminates against more background. A handful of variables are introduced and discussed informally in this section, with the aim of providing a foundation for the discussions on the tau validation software in Section 3. For a complete list of the discriminating variables and a description how they are used the reader is referred to Ref. [83].

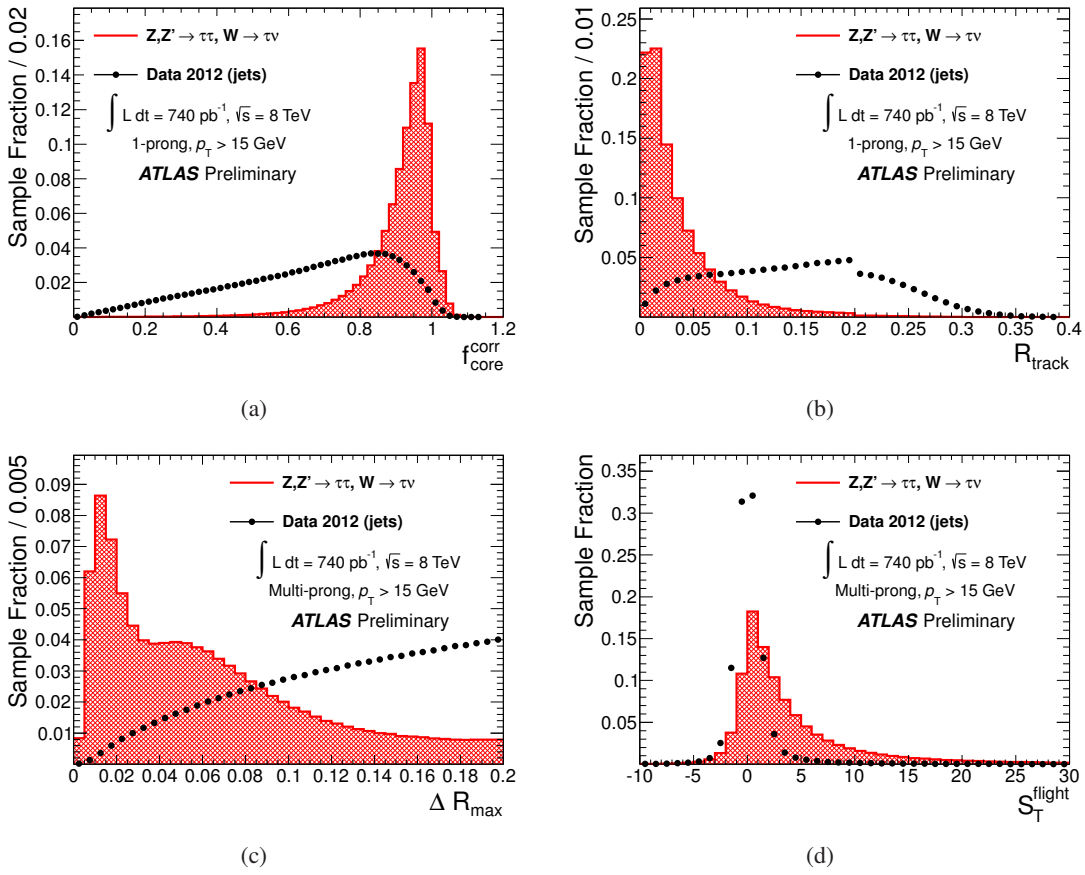


Figure 19: Distributions of discriminating variables which are used to reject jet background in tau identification. Events populated with true taus are taken from simulated $Z, Z' \to \tau\tau$ and $W \to \tau\nu$ MC, while the background is taken from jet data from 2012. The variables are all defined in the text [83].

At a given momentum a jet coming from a tau will tend to be narrower that a QCD jet. Hence calorimeter and track based variables describing shower size and shape are important for jet discrimination. To this effect an important calorimeter based variable is the pile-up-corrected core energy fraction ($f_{\text{core}}^{\text{corr}}$), which is defined as the fraction of transverse energy deposited in the center most cone ($\Delta R < 0.1$) of the $\tau_{\text{had-vis}}$. Figure 19(a) shows the $f_{\text{core}}^{\text{corr}}$ distribution of 1-prong tau candidates with $p_T > 15$ GeV coming from simulated signal Z , $Z' \to \tau\tau$ and $W \to \tau\nu$ versus QCD jet data from 2012 [83]. The distribution shows that there is a large separation in $f_{\text{core}}^{\text{corr}}$ between events with true taus, and events with only jets.
Important tracking variables include the track radius (R_{track}), defined as the p_T-weighted track distance from the tau axis (Figure 19(b)), and maximum ΔR (ΔR_{max}) for multi-prong decays, which is the maximal ΔR_{max} between a core track associated to the $\tau_{\text{had-vis}}$ and the intermediate axis (Figure 19(c)). The discontinuity in Figure 19(b) at 0.2 is caused by the fact that 1-prong tau candidates can have additional tracks in the isolation annulus. While jets with no isolation tracks will populate only the region of $\Delta R < 0.2$, jets with isolation tracks will populate the whole ΔR range, introducing the hard discontinuity at 0.2. The significance of a reconstructed secondary vertex, S_T^{flight}, also provides good discrimination for 3-prong decays (Figure 19(d)).

2.4.4 Di-tau mass reconstruction with the Missing Mass Calculator

As mentioned in the introductory paragraph of this section, τ-leptons are present in the final state of the $A \to Zh \to \ell\ell\tau\tau$ analysis. The analysis requires an effective way in order to fully reconstruct and identify the A boson from the final state. This is a challenging prospect when one considers the presence of two τ leptons in the final state. Both τ-leptons decay with neutrinos, via either leptonic ($\tau \to \ell\,\bar{\nu}_\ell\nu_\tau$ and $\tau \to \ell\,\bar{\nu}_\ell\nu_\tau\gamma$) or hadronic ($\tau \to \pi^\pm\upsilon$, $\tau \to n\pi^0\pi^\pm\upsilon$, $\tau \to 3\pi^\pm\upsilon$ and $\tau \to n\pi^0 3\pi^\pm\upsilon$) decay, contributing to a large amount of E_T^{miss}. Since the E_T^{miss} is reconstructed as a transverse 2-vector quantity, associating the individual neutrino 4-momentums to their respective parent tau, and as such fully reconstructing the di-tau system, is impossible. Reconstructing the di-tau 4-momentum becomes even more complex when considering that resonant decaying taus generally decay back-to-back, and the missing momentum associated with their neutrinos partially cancel out. Reconstruction of the di-tau mass ($m_{\tau\tau}$) is therefore a challenging obstacle in any resonant search decaying to two or more taus. This section describes the available methods that are used to partially and fully reconstruct the $m_{\tau\tau}$ mass in ATLAS, and introduces the Missing Mass Calculator (MMC) as the chosen method for reconstructing $m_{\tau\tau}$ in the $A \to Zh \to \ell\ell\tau\tau$ analysis. Each method has it's own benefits and faults and deciding on how to deal with $m_{\tau\tau}$ reconstruction should not be considered as set in stone. For a detailed description of these methods the reader is encouraged to visit Ref. [87].

The transverse mass method: The first method considered is the transverse mass method, and relies on a reduced invariant mass reconstruction. One can choose to either reconstruct $m_{\tau\tau}$ from the visible decay products, $m_{\tau\tau}(\tau_{\text{vis1}}, \tau_{\text{vis2}})$, or from the visible decay products and the E_T^{miss} in the event, $m_{\tau\tau}(\tau_{\text{vis1}}, \tau_{\text{vis2}}, E_T^{\text{miss}})$. The benefit to this method is that it can be applied to and reconstruct any signal event and does therefore not reduce the available statistics. Furthermore the transverse mass method generally provides good discrimination against QCD jets, and is chosen over other techniques in the MSSM neutral Higgs search ($A/h/H \to \tau_{\text{had}}\tau_{\text{had}}$) for this reason [30]. However, while neglecting to take into account the full neutrino momenta, the transverse mass method leads to a significantly reduced sensitivity.

The collinear approximation: This method has an advantage over the transverse mass method in that it fully reconstructs $m_{\tau\tau}$. It assumes that the neutrinos from each tau decay are nearly collinear to the corresponding visible tau decay. Furthermore it assumes that the E_T^{miss} in an event comes solely from tau decays. The total invisible momentum carried away by neutrinos in each tau decay ($p_{\text{miss}_{1,2}}$) can then be estimated by solving a set of two equations:

$$\begin{aligned}(E_T^{\text{miss}})_x &= p_{\text{miss}_1}\sin\theta_{\text{vis}_1}\cos\phi_{\text{vis}_1} + p_{\text{miss}_2}\sin\theta_{\text{vis}_2}\cos\phi_{\text{vis}_2}\\ (E_T^{\text{miss}})_y &= p_{\text{miss}_1}\sin\theta_{\text{vis}_1}\sin\phi_{\text{vis}_1} + p_{\text{miss}_2}\sin\theta_{\text{vis}_2}\sin\phi_{\text{vis}_2},\end{aligned} \tag{15}$$

where $\theta_{\text{vis}_{1,2}}$ and $\phi_{\text{vis}_{1,2}}$ are the polar and azimuthal angles for each visible tau decay. The mass of the di-tau system can then be estimated by $m_{\tau\tau} = \sqrt{\frac{m_{\text{vis}}}{x_1 x_2}}$, where m_{vis} is the invariant mass of the di-tau system, and $x_{1,2} = \frac{p_{\text{vis}_{1,2}}}{p_{\text{vis}_{1,2}}+p_{\text{miss}_{1,2}}}$ Assuming that the neutrinos are approximately collinear to their respective visible tau decay is a very restrictive assumption. This occurs in a very limited number of events, where the $\tau\tau$ system is boosted, *i.e.*, for highly energetic taus. Furthermore the visible tau decays cannot be back-to-back in the transverse plane, as the system of Equations 15 becomes degenerate as $\phi_{\text{vis}_1} \to \phi_{\text{vis}_2} + \pi$. This becomes exceedingly problematic in topologies like $H \to \tau\tau$, as the majority of events are produced with back-to-back taus. The collinear approximation can only ultimately be used on a relatively small fraction of events.

The Missing Mass Calculator: The MMC offers an alternative method for fully reconstructing $m_{\tau\tau}$, without the statistical limitations of the collinear approximation. It assumes that all neutrinos in an event come from tau decays. Full reconstruction of the event topology requires solving 6 to 8 unknowns, depending on how many taus decay leptonically. These are the spacial components of the invisible momentum carried away by the neutrinos, as well as the invariant mass of the neutrinos of each leptonic tau decay. The system of unknowns is under-constrained and an exact solution is not possible under these conditions. However, not all solutions in this system are equally likely, and knowledge of the visible tau decay kinematics can be used to distinguish the more likely solutions, from less likely ones. For the fully hadronic case a scan for $m_{\tau\tau}$ over points in $(\phi_{\text{miss}_1}, \phi_{\text{miss}_2})$ is performed, and the value which maximizes an event likelihood function is chosen as the estimator of $m_{\tau\tau}$. A similar process is followed for events with leptonically decaying taus, where higher dimensional scans are considered. The additional unknowns decrease the significance of the MMC method for leptonic tau decays. Figure 20 shows the performance of the MMC when compared to the transverse mass and collinear approximation methods. Overall the MMC provides an improved reconstruction of the mass of the di-tau system compared to the transverse mass method. It is also not constrained by the event kinematics as with the collinear approximation, seen by the large number of events in the zero bin, where no solution could be found.

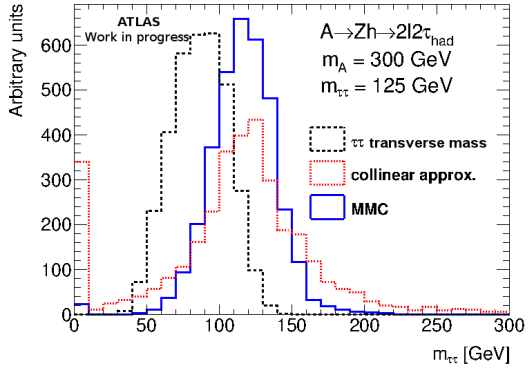


Figure 20: Comparison of $m_{\tau\tau}$ distributions of a $m_A = 300$ GeV signal sample decaying via $A \to Zh \to \ell\ell\tau_{\text{had}}\tau_{\text{had}}$ using different di-tau mass reconstruction techniques.

3 Physics validation and tau leptons

As explained in Section 2.3.5 the purpose of the Physics Validation groups is to test the reconstruction and identification of different objects for different ATHENA releases that will be used for MC production. The large number of events in the validation samples expose differences in the samples that may not be observed otherwise, such as small percentage discrepancies in an identification yield. The validations are performed by comparing the new ATHENA samples (test sample) to samples generated by an already verified version of ATHENA (reference sample). The samples are centrally generated. The processes to be generated are requested by the specific validation groups and experts within ATLAS. The samples are available for processing in AOD format. In order to maintain a unique labeling scheme the Physics Validation group uses the following naming convention for their samples:

`valid1.processNumber.processDescription.recon.AOD.eXXXX\_sXXXX\_rXXXX`

The first parameter (*valid1*) is unique to validation samples and may also be labeled *valid2*, *etc.* if the samples are reprocessed due to some type of error. The *processNumber* is a unique six digit number for

the process and MC generator used. The *processDescription* describes the MC generator and the process in words. The *recon* parameter refers to a reconstruction validation. The *AOD* parameter is the format of the samples. The last three parameters are the production tags. The *eXXXX*, *sXXXX* and *rXXXX* tags refer to the event generation, simulation and reconstruction configurations respectively, where XXXX is a three or four digit number. Groups run their own reconstruction code and produce histograms comparing variables of the test and reference samples. The results are discussed at regular Physics Validation meetings.

As discussed in Section 2.3.4 the updates to the EDM include a migration to the new xAOD format in Run-II, which will replace the AOD format. The move to xAOD involved a large effort to migrate object reconstruction packages. From the beginning of 2014 Physics Validation began to coordinate the migration of the individual validation codes to run on xAOD files. The validation of the the migrated code began shortly after, alongside the reconstruction migration efforts. The migration is being done and tested in ATHENA Release 19. Although the new EDM will be used for Run-II, requests for MC production for Run-I are continuously requested and the validation of ATHENA 17 continued to be an important task in 2014. The validation of τ-lepton reconstruction in ATHENA 17 will be discussed in Section 3.1. This will be followed by a discussion on the migration of the tau validation code to xAOD for ATHENA 19 (Section 3.2). Lastly an example validation using ATHENA 19 is shown in Section 3.2.3. During my time as the Tau Physics Validation contact, a period from July 2013 till November 2014, my tasks involved performing numerous weekly MC validation in ATHENA 17. From 2014 I was in charge of migrating and updating the Tau Validation code to ATHENA 19, which included writing the code from scratch, attending meetings to receive feedback from the tau CP conveners, and implementing tools into the software, including the migration of tau truth matching tools. During this period, I was involved in the testing of the ATHENA 19 tau validation package, as well as performing ATHENA 19 MC validations while still doing a reduced amount ATHENA 17 validations. I also produced several comparisons of ATHENA 19 MC versus ATHENA 17 MC.

3.1 Tau validation for ATHENA 17

The validation of versions of ATHENA 17 is coordinated centrally by the Physics Validation coordinators who send out various tasks during a given validation. Datasets are produced centrally by Physics Validation. The datasets produced by the Physics Validation group which are used by the tau validation are: a $Z \rightarrow \tau\tau$ process produced with Powheg and Pythia8; a $t\bar{t}$ sample with a leptonic filter produced with MC@NLO; and a $Z' \rightarrow \tau\tau$ with $m_Z = 750$ GeV produced with Pythia8. Note that the $t\bar{t}$ sample decays as $t\bar{t} \rightarrow WbWb$ and is forced to have one $W \rightarrow \ell\nu$ due to the leptonic filter. The other W may decay into electrons, muons, taus (approximately 10.8% of the time for each type of leptonic decay) or hadronically (67.6%) [20]. These samples are considered to be highly populated with true taus and hence provide the tau reconstruction and identification algorithms with many tau candidates. Hence, they can be used for testing the distributions of tau variables. Two background samples are also used: an electron populated $Z \rightarrow ee$ produced with PowhegPythia8; and a QCD jet sample produced with Pythia8. These samples are used for ensuring that no changes occur in electron and jet discrimination.

For any given task the analyzer must run their validation code in order to create histograms of relevant variables. For the validation of τ-leptons in ATHENA 17 one uses the TauValidation package which is part of the PhysicsAnalysis package in the AtlasOffline project. The generation of histograms is controlled by a job options file. The job options file runs both the TauRec and TauDiscriminant packages, which produce the variables used for tau reconstruction and tau identification as described in Section 2.4. TauRec falls under the Reconstruction package, while TauDiscriminant is part of the PhysicsAnalysis package. In order to run the TauValidation code on a given dataset one must set up the required version

of ATHENA into a local work-space. In the work-space the user must check out all the required packages, including TauValidation, TauRec and TauDiscriminant. Once this is done all the packages need to be built via CMT. One can test the setup by running the job options file with ATHENA on a single sample from the dataset. A single sample from the dataset can be downloaded locally. pATHENA is used to run the job options file on the Grid on the entire dataset. The output of the job options file is an array of D3PDs which are downloaded locally and merged into a single D3PD file. The D3PD has an array of histograms of interesting variables. A screen-shot of a D3PD viewed in ROOT is shown in Figure 21.

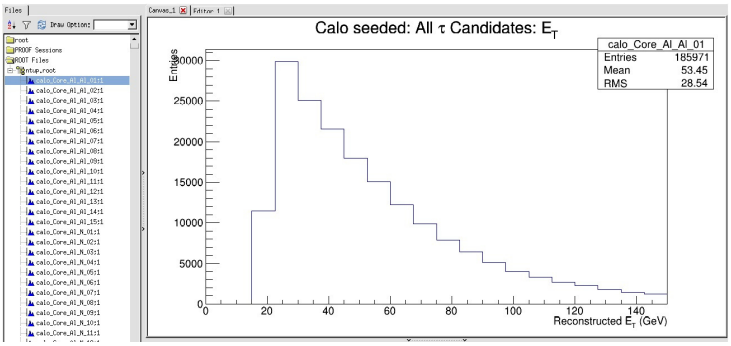


Figure 21: A screen-shot of a tau validation D3PD file viewed using the ROOT GUI. Shown on the left hand side is an incomplete list of available histograms alongside a histogram of the transverse energy, E_T, of all calorimeter seeded tau candidates.

Using scripts in the TauValidation package the histograms of two D3PDs, one from the test dataset and the other from the reference dataset, are overlayed for comparison. Since the distributions in tau validation are binned, a χ^2 test is used for testing the difference between the test and reference distributions. Let T_i be the number of entries in the i^{th} bin of the test distribution. Similarly let R_i be the number of entries in the i^{th} bin of the reference distribution. The χ^2 distribution is given by,

$$\chi^2 = \sum_i \frac{(T_i - R_i)^2}{T_i + R_i}. \tag{16}$$

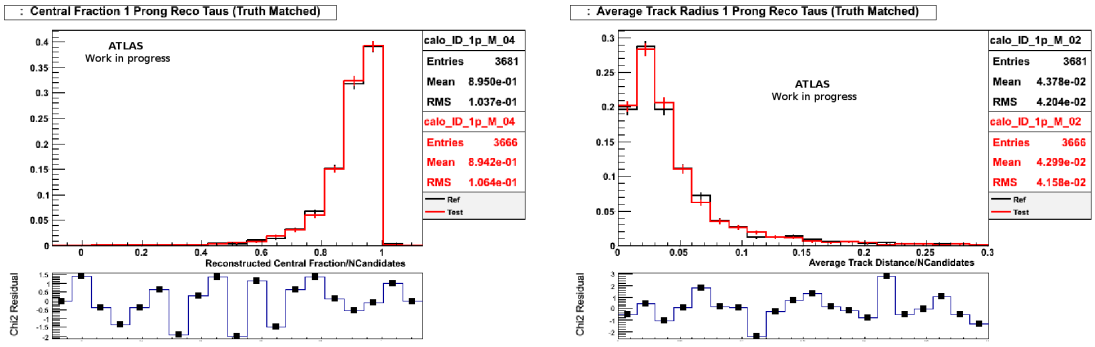
The distributions are scored in terms of χ^2/N_{df} where N_{df} is the number of degrees of freedom. This N_{df} is essentially the number of non-empty bins in the overlapped distribution. The distributions are characterized as green if $\chi^2/N_{\text{df}} < 10$, yellow if $10 < \chi^2/N_{\text{df}} < 100$, and red if $\chi^2/N_{\text{df}} > 100$. Due to the large amount of distributions produced in tau validation, the χ^2 test is used so as to provide a fast way of picking up problematic distributions. HTML files are automatically generated using scripts in TauValidation. The HTML files are saved in a group directory for easy accessibility. Figure 22 shows the overview page of the comparison of the test and reference of a $t\bar{t}$ process with a leptonic filter. Figure 23 shows some comparison histograms of the same validation which can be compared to the distributions in Figure 19.

Residual Legend	0 - 10	10 - 100	>100
Efficiency Legend	0 - 1	1 - 5	>5

Author 1 and 3 Seeded Tau (Pt 20GeV-10TeV)

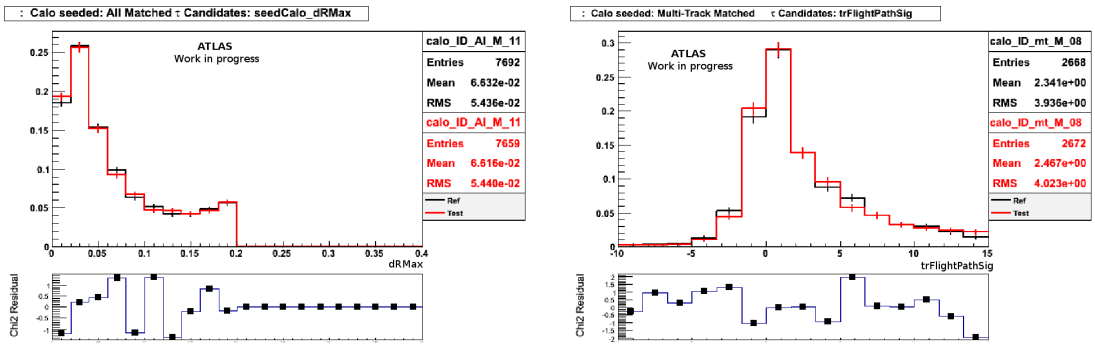
Type of Tau Candidates	Number of Variables Classified as:			
	Green	Yellow	Red	All
Distributions ID	296	9	0	305
Distributions MATCHED	204	7	0	211
Distributions NEWCORE	30	0	0	30
Distributions Total	814	12	0	826
Efficiencies MATCHED	21	0	0	21
Efficiencies Total	183	0	0	183

Figure 22: A screen-shot of the overview HTML page of a given task and process in the Tau Validation website.



(a)

(b)



(c)

(d)

Figure 23: Comparison histograms of tau variable distributions for test and reference samples in a tau validation task. Distributions for taus are taken from simulated $t\bar{t}$ MC. Truth matched distributions of the (a) 1-Prong core energy fraction, (b) 1-Prong R_{track}, (c) multi-track ΔR_{max} (d) and multi-track S_T^{flight} are shown.

3.2 Tau validation for ATHENA 19

The migration of AOD to xAOD required validation experts to rewrite their validation code so that it could work on the new xAOD data classes. Since most of the code would have to be rewritten from scratch, Physics Validation took this opportunity to restructure the procedure which is used for performing validations. No longer would the individual validation groups spend countless hours battling with the submission of jobs to the grid to produce results, but rather the histograms would be produced centrally. This requires individual validation groups to maintain their code, and commit any changes to ATHENA. The validation code of each group is then run centrally on the test and reference samples. The aim of this is to minimize the time that experts would have to spend producing results, so that more time would be focused on interpreting results and communicating with the working groups.

3.2.1 The TauDQA package

The validation of τ-lepton reconstruction in ATHENA 19 is done with the TauDQA package. This package has a direct dependence on the TauHistUtilities package which defines histogram classes which are filled in TauDQA. The main class in TauDQA is called PhysValTau. This class is used to fill the histograms of interest. An array of variables is plotted for all tau jet candidates. Later, different variables are plotted for matched and fake tau jets.

In the xAOD samples all tau candidates are provided by the TauJetContainer. The TauJetContainer is simply a vector of TauJet objects in a given event. The TauJet class is defined in the Event/xAOD/xAODTau package and is available as part of the AtlasOffline project. The TauJet class contains variables which are used to register information about the tau jet. The variables include, but are not limited to: the jet's 4-vector variables; individual 4-vector components at different calibration levels; the summed up charge of all tau tracks; boolean type identification flags; links to incoming and outgoing vertex and secondary decay vertex objects; tracking variables, such as number of tracks and the ΔR of the π^0 cone; links to *eFlowRec* and *cellBased* Particle Flow Objects(PFOs). Alongside the variables are various getter and setter methods for retrieving and filling the variables, respectively. The object links are used to call on the Vertex and PFO object containers, related to the TauJet object. The Vertex class is defined in the Event/xAOD/xAODTracking package while the PFO class is defined in the Event/xAOD/xAODPFlow package.

One of the most important particle containers in the xAOD is the TruthParticleContainer. This container is a vector of all truth particles in a given event. The class for handling truth particles is the TruthParticle class, which is found in the Event/xAOD/xAODTruth package. Truth particles are identified by a MC numbering scheme described in detail in Ref. [20]. The numbering scheme is defined by the Particle Data Group and known as the particles PDG ID. As an example, a particle with a PDG ID of 11 is an electron, 13 is a muon, and 15 is a τ-lepton. The lepton neutrinos have a PDG ID of 12, 14 and 16 for ν_e, ν_μ and ν_τ respectively. A negative PDG ID refers to the anti-particle, so a particle with a PDG ID of -11 is a positron. The TruthParticle class defines many variables for a single truth particle, including: the particle's 4-vector; the PDG ID; the particle status, giving an indication of whether it is a decay particle; the number of parents and children, along with links to these objects; boolean flags indicating whether a particle has production or decay vertexes, along with links to these objects; the particles charge and polarization; *etc.*.

In the PhysTauVal all the histogram definitions from TauHistUtilities are called. For each event in the xAOD the TauJetContainer and TruthContainer. There is a loop trough each TauJet object in the TauJetContainer. Every TauJet with $|\eta| > 2.5$ or $p_{\mathrm{T}} < 20$ GeV is discarded. For each TauJet passing this

selection an array of BDT and PFO related distributions are plotted. Reconstruction and kinematic distributions are plotted for all 1-prong and 3-prong TauJets. After the loop though the TauJetContainer there is a loop through the true tau objects in the TruthParticleContainer. For each true tau, a TauJet candidate is considered for truth matching. Histograms for tau matched, electron matched and fake TauJets are then plotted. The procedure for matching true taus and TauJet objects is described directly below.

3.2.2 Truth matching of tau leptons

It is important to understand the effectiveness of tau reconstruction, particularly since τ-leptons have many background processes in ATLAS. The effectiveness of tau reconstruction can be directly probed in MC data as both reconstructed and truth information are available. In tau validation it is therefore possible and important to monitor the distributions of reconstructed taus which are successfully matched to true taus. As explained above, the TruthParticle class contains the PDG ID of any truth particle. One could imagine that matching a TauJet to a true tau would be as simple as finding a TruthParticle with PDG ID = |15|, and testing if it overlaps spatially with the TauJet. Unfortunately the story is not so simple. In Section 2.4.1 it was explained that a τ-lepton's lifetime is short, and any tau will decay before reaching the ID. Any reconstructed τ-lepton will therefore only be observed without it's missing energy. Since this is not taken into account for taus in the TruthParticleContainer, a true tau needs to first be reduced to it's visible counterpart. A true visible tau is a true tau minus the total 4-vector of it's neutrino decay. The full truth matching process used in tau validation is described here.

The first step in the truth matching procedure is to retrieve all true hadronic taus from the TruthParticleContainer. A loop trough every TruthParticle of the TruthParticleContainer is performed. Each TruthParticle with a PDG ID = |15| and passing a good status requirement is considered. Furthermore the TruthParticle needs to have a decay vertex object. A loop through all the children (outgoing) TruthParticle objects from the decay vertex is performed. Each child's PDG ID is checked. If any child is either an electron, muon or tau, the TruthParticle is disregarded as being a hadronic tau. This is to eliminate leptonically decaying taus, as well as tau self coupling processes, $e.g\ \tau \rightarrow \tau\gamma$ (where the daughter tau will still be considered as a hadronically decaying candidate). Each TruthParticle passing this selection is saved in a new TruthParticleContainer, referred to here as the TrueHadTauContainer.

The TrueHadTauContainer now contains all TruthParticle objects which have been identified as true hadronic taus. For each TruthParticle in the TrueHadTauContainer, the number of charged and neutral decay hadrons is counted. To count the number of charged hadrons one loops over each decay and subsequent decay child particle of the TruthParticle. Any child particle with a PDG ID = $\pm$211 (for $\pi^{\pm}$) and passing a status requirement is counted. Charged kaons are also counted. Neutral hadrons are counted in much the same way, except that the child's PDG ID = $\pm$111 (for π^0). The TruthParticle is only considered if it decays into 1 or 3 charged, and 0 to 5 neutral hadrons. The visible 4-vector of the TruthParticle is then constructed. This is done by adding the 4-vectors of all the direct descendant particles with the exception of the neutrinos (PDG ID $\pm$12, $\pm$14 and $\pm$16 for ν_e, ν_μ and ν_τ). Every true visible tau with $|\eta| > 2.5$ or $p_{\mathrm{T}} < 20$ GeV is discarded.

Once the true visible tau has been constructed, it is time to loop through each TauJet in the TauJetContainer, and search for a suitable match. A match in ΔR is performed between the 4-momentum of the true visible tau and the 4-momentum of the intermediate axis of the TauJet. If $\Delta R < 0.2$ the objects are considered to be matched. The TauJet which produces the smallest ΔR below 0.2 with the true visible tau is chosen as a truth matched reconstructed tau. The truth matched reconstructed tau is removed from the TauJetContainer and not considered in subsequent matching.

All matched TauJets are used to fill histograms for truth matched taus in the HistUtilities package. Along with kinematic and identification related histograms two histograms are defined for keeping track of the *cellBased* and *eFlowRec* decay migrations. The number of tau jets is displayed on the y-axis. On the x-axis are 13 bins labeled by a $tX_tY_trX_rY_r$ convention. Here the t stands for the true tau, while the proceeding X_t and Y_t are numbers representing the number of charged and neutral hadrons, respectively. The values of X_t and Y_t are either $X_t = 1$ and $Y_t \in \{0, 1, x\}$ (where $1 < x \leq 5$), or $X_t = 3$ and $Y_t \in \{0, x\}$ (where $0 < x \leq 5$). Similarly r stands for the reconstructed tau, while X_r and Y_r are numbers representing the number of charged and neutral hadrons, respectively. Therefore, as an example, the bin labeled $t10r10$ shows the number of TauJets decaying to one charged hadron and no neutral hadrons, matched to a true visible tau with the same decay signature. Similarly, the bin labeled $t30r3x$ shows the number of TauJets decaying to three charged hadrons and at least one neutral hadron, matched to a true tau which decayed to three charged hadrons and no neutral hadrons. Finally two bins labeled $t1r3$ and $t3r1$ show the number of 1-Prong TauJets matched to 3-Prong true visible taus and 3-Prong TauJets matched to 1-Prong true visible taus, respectively. The migration histograms are useful in that they can be used to detect problems in the *cellBased* or *eFlowRec* algorithms with a specific reference to which decay channels are being affected. An example of each histogram is shown in Figure 28 of the following section.

All TauJets which are not matched to a truth tau are considered for matching to electrons in the TruthParticle container (|PDG ID| = 11). A match in ΔR is performed between the 4-momentum of true electrons and the 4-momentum of the TauJet. If a TauJet is neither matched to a true electron or a true visible tau, it is labeled as a fake tau jet.

3.2.3 Example validation with ATHENA 19

This section presents a selected set of histograms from a validation task completed by the Tau Validation group. The validation histograms come from the official validation code and are rather coarse, so the reader is excused from digesting the poorly formatted figures. The validation is of a simulation patch containing a significant speed increase. Both test and reference samples are simulated with the Run-I detector geometry w/o pileup. Here a new Geant4 patch in ATHENA 17.7.5.1 is compared to the previously validated ATHENA 17.7.4.2. For the most part changes where not expected to be seen between both the test and reference, although slight deviations in truth information are possible due to improvements in the simulation framework's truth handling. Detector simulation is done in ATHENA 17, while both the test and reference samples are reconstructed using ATHENA 19.1.1.5. The validation is therefore performed using the latter release. The samples which are used for this validation are: $Z \to \tau\tau$ (PowhegPythia8); $t\bar{t}$ with a leptonic filter (MC@NLO); $Z' \to \tau\tau$ with $m_Z = 750$ GeV (Pythia8); and $Z \to ee$ (PowhegPythia8). These samples are identical to those used in ATHENA 17 validations due to the fact that the simulation had to be performed in ATHENA 17. In validations where both simulation and reconstruction are performed with ATHENA 19 the $t\bar{t}$ sample is not used, and the $Z \to \tau\tau$ (PowhegPythia8) and $Z' \to \tau\tau$ samples are replaced by $Z \to \tau\tau$ (Pythia8) and Drell-Yan $\tau\tau$ (Pythia8), respectively.

Figure 24 and Figure 25 show the comparison of the test and reference distributions of the different samples for electron and jet BDT identification variables, respectively. Considered in the distribution is every reconstructed tau jet object in the xAOD with a $p_{\mathrm{T}} > 20$ GeV. For BDTEleScore (BDTJetScore), a tau jet with a value close to zero is considered to be electron(jet)-like, whereas values closer to unity are more tau-like. This is seen in Figure 24 where the $Z \to ee$ distribution has a right-skewed distribution which indicates electron-like jets, while the signal distributions are left-skewed. The slight differences in the test and reference histograms where not considered significant as they are a product of slight shifts in the distributions from the detector differences. The χ^2/N_{df} are below unity for all histograms, which is considered to pass the chi squared test for goodness in pysics validation. Similarly in Figure 25 all

distributions, with the exception of $t\bar{t}$, are left-skewed, indicating that the reconstructed tau jets are tau-like. The right-skewed distribution in Figure 25(a) is due to the large hadronic background in the $t\bar{t}$, as this sample will have a large number of events without true taus, and a large number of QCD jets coming from W decay. As emphasized by Figure 25(b) and Figure 25(c), which have many tau jets with low BDTJetScore values, the BDTJetScore is not powerful enough to identify hadronically decaying τ-leptons by itself. The distribution in Figure 25(d) further shows that electrons produce very tau-like jets. This highlights the importance of the additional electron discrimination (electron veto) with respect to identifying taus, embodied in variables such as BDTEleScore. The small deviations between the test and reference histograms in Figure 25(b) produce a $\chi^2/N_{\mathrm{df}} = 1.057$, which is not significant, particularly when you further consider that the differences manifest as a small histogram shape effect.

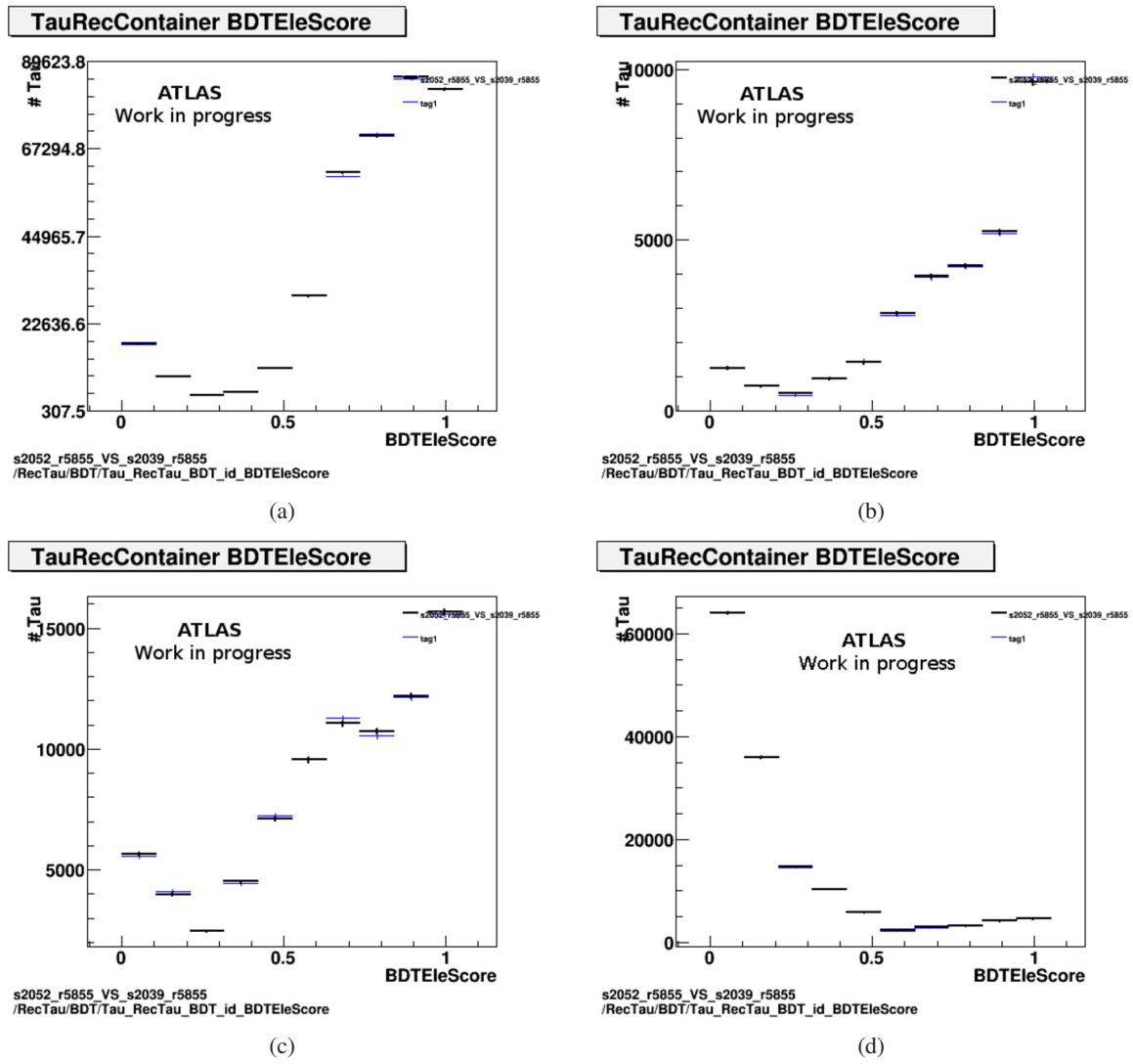


Figure 24: Comparison of test (black) and reference (blue) distributions of the BDT electron score variable for all selected reconstructed tau jets in the (a) $t\bar{t}$, (b) $Z \to \tau\tau$, (c) $Z' \to \tau\tau$ and (d) $Z \to ee$ samples.

As mentioned in Section 2.4.3, an important tau identification variable for 1-prong tau candidates is the $f_{\mathrm{core}}^{\mathrm{corr}}$, shown in Figure 19(a). Figure 26 shows the $f_{\mathrm{core}}^{\mathrm{corr}}$ distribution comparisons of all 1-prong tau jets, 1-prong tau jets which have been matched, and fake 1-prong tau jets for $t\bar{t}$. Figure 26(a) shows the total

$f_{\text{core}}^{\text{corr}}$ distribution for all 1-prong tau jets, which shows that there are a number of event with low values. If one compares this to the distributions in Figure 26(b) (1-prong truth matched tau jets) and Figure 26(c) (1-prong fake tau jets) it is evident that the low tail seen in Figure 26(a) is due to jets which have been mis-identified as taus. This agrees with the low tail of the QCD background in Figure 19(b). The small fluctuations between the test and reference distributions are within statistical errors and can be explained by the improvements with respect to truth information mentioned earlier.

It was also shown in Section 2.4.3 that ΔR_{max} provided good discrimination for multi-prong tau jets, where QCD jets tend to have higher values of ΔR_{max} (Figure 19(c)). Figure 27 shows the comparison of all, truth matched and fake 3-prong tau jets in $t\bar{t}$. This shows that the ΔR_{max} distribution tends to have lower values for true tau jets when compared to its QCD background, as expected. For completeness the migration histograms for *cellBased* and *eFlowRec* described the previous section are shown for $t\bar{t}$ in Figure 28. The slight variations in these histograms can be explained by the expected differences in the truth information variables.

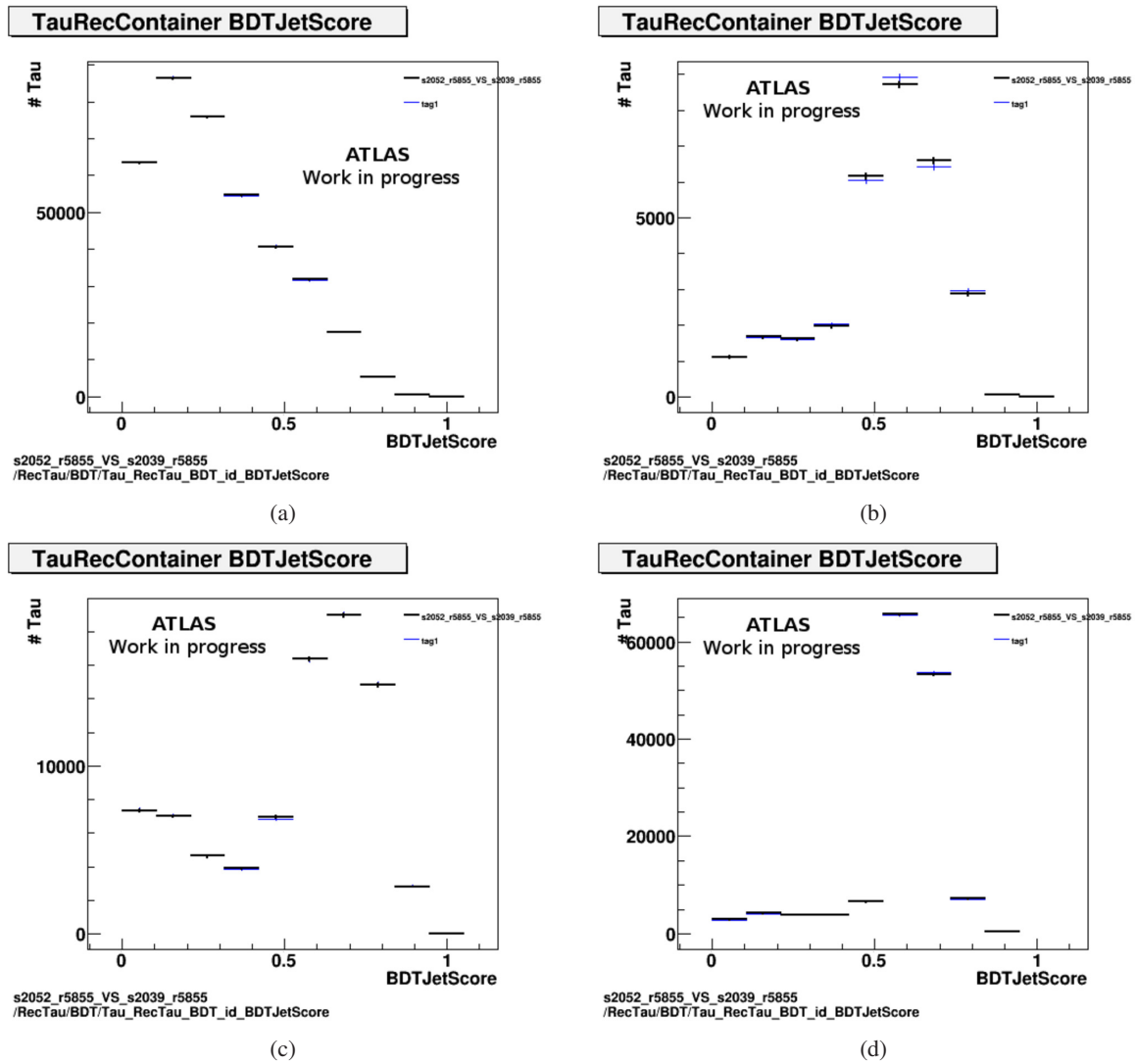
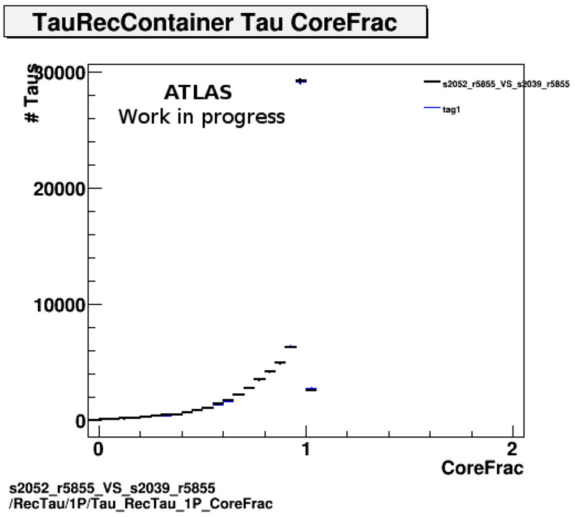
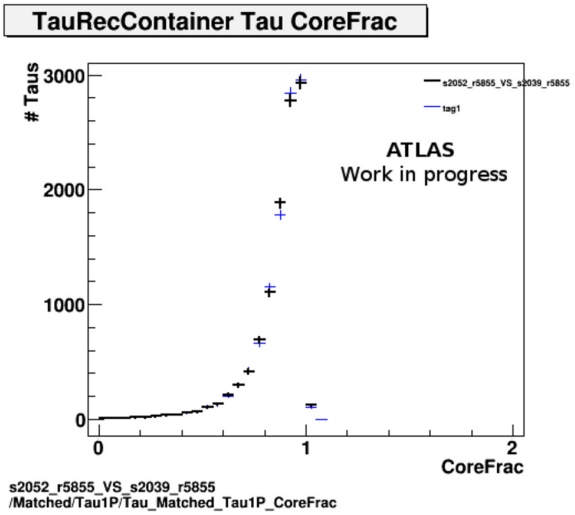


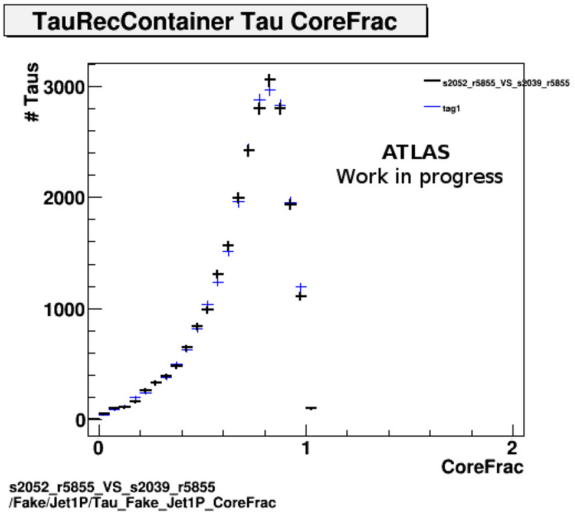
Figure 25: Comparison of test (black) and reference (blue) distributions of the BDT jet score variable for all selected reconstructed tau jets in the (a) $t\bar{t}$, (b) $Z \to \tau\tau$, (c) $Z' \to \tau\tau$ and (d) $Z \to ee$ samples.



(a)

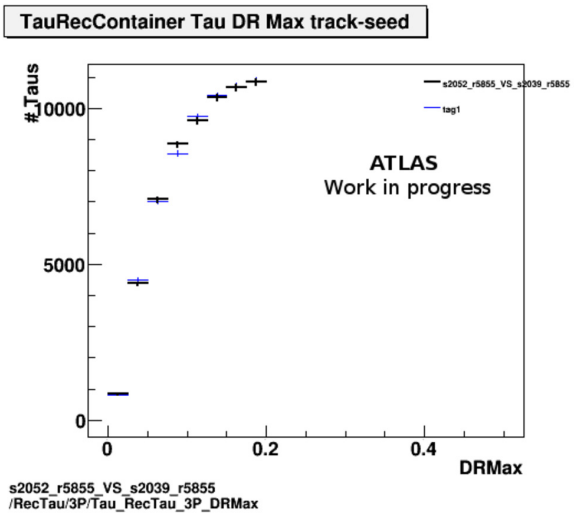


(b)

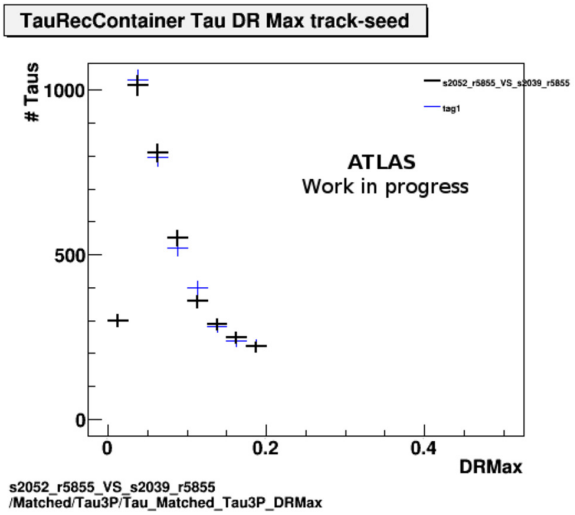


(c)

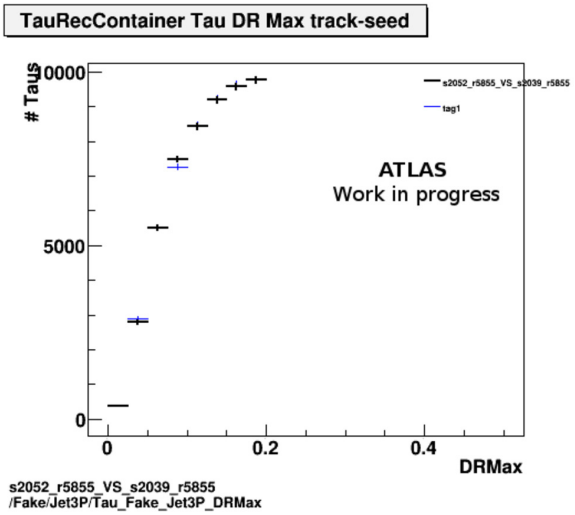
Figure 26: Comparison of test (black) and reference (blue) $f_{\text{core}}^{\text{corr}}$ distribution for (a) all, (b) truth matched, and (c) fake 1-prong tau jets in the $t\bar{t}$ validation samples.



(a)

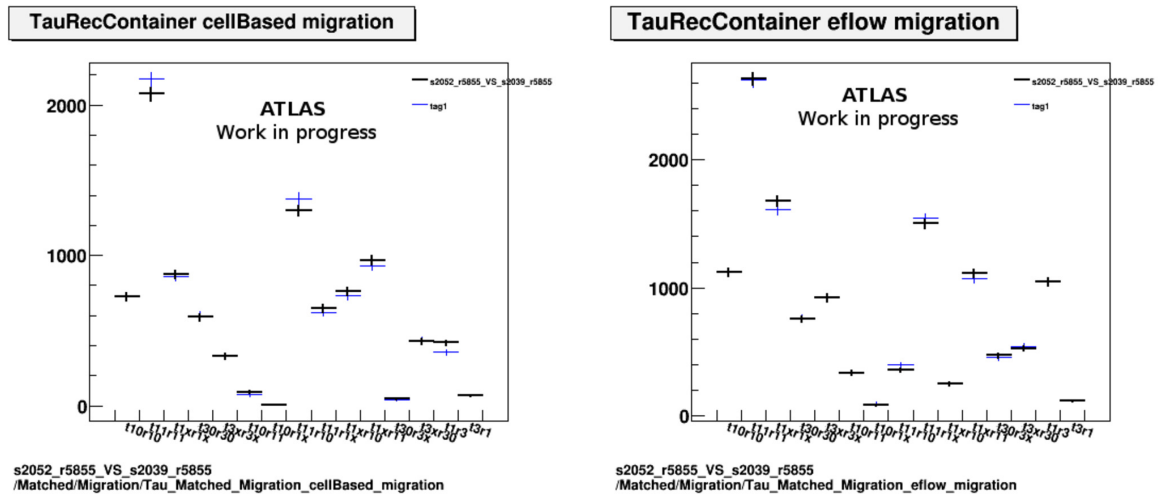


(b)



(c)

Figure 27: Comparison of test (black) and reference (blue) $\Delta R_{\max}$ distribution for (a) all, (b) truth matched, and (c) fake 3-prong tau jets in the $t\bar{t}$ validation samples.



(a) (b)

Figure 28: Comparison of test (black) and reference (blue) migration distributions for truth matched tau jets in $t\bar{t}$ using either (a) *cellBased* or (b) *eFlowRec* reconstruction algorithms.

4 The A →Zh →$\ell\ell$ $\tau\tau$ analysis

As discussed in the introductory paragraph of this thesis, the search for the pseudoscalar A boson gives a gateway to searches for physics beyond the SM. The search for a gluon-fusion produced A in the decay to Zh is largely motivated by a desirable cross-section times branching ratio within $220 \leq m_A \leq 1000$ GeV, even for ATLAS Run-I data at 8 TeV center of mass energy collisions. The $A \rightarrow Zh \rightarrow \ell\ell\tau\tau$ has never before been searched for in ATLAS, and the recent discovery of the Higgs boson opens a way to look at this topology by incorporating the m_h mass in the search.

The $A \rightarrow Zh \rightarrow \ell\ell\tau\tau$ analysis is split in three different channels depending on the decay of the di-tau system, *i.e.* $\tau_{lep}\tau_{lep}$, $\tau_{lep}\tau_{had}$ or $\tau_{had}\tau_{had}$. The three channels differ in their final state signature and as such will have different methodologies. This difference manifests itself in distinctions between object and event selections, background processes and predictions, and systematic uncertainty calculations between the different channels. The three different analysis strategies do however have large similarities. Each analysis optimizes their own object and event selection in such a way as to maximize their signal significance over background. Moreover, although the different final states result in different background signatures, all three analyses predict the contribution of fake background in some data-driven way. Finally the systematic uncertainty calculations will differ between the channels inherently from the preceding differences described, *i.e.* differences in event triggers, signatures, and background predictions require different systematic uncertainties to be used.

This thesis focuses on the $\tau_{had}\tau_{had}$ channel as it is the channel in which my work was undertaken. A summary of the chosen MC and data samples are given in Section 4.1. A general object selection which is used, in most cases, across all three channels is given in Section 4.2. A description of the event selection used in the $\tau_{had}\tau_{had}$ channel is given in Sections 4.3 and 4.4, with a description of the selection's optimization study given in Section 4.5. The description of the method used in the $\tau_{had}\tau_{had}$ channel to predict the fake tau background contribution is given in Section 4.6. The systematic uncertainty calculations for the $\tau_{had}\tau_{had}$ channel are described in Section 4.7. Finally the three channels converge with a common method for setting limits on the expected cross-sections times branching ratios, described in

Section 4.8. Where applicable, short summaries of the results from the $\tau_{lep}\tau_{lep}$ and $\tau_{lep}\tau_{had}$ studies are given, however, a rigorous review of these channels is not presented in this thesis. The resulting limits on the cross-sections times branching ratios are combined in Ref. [88] with similar limits set by an $A \to Zh \to ffb\bar{b}$ analysis, where $f = e, \mu$ or ν. The combined limits are interpreted in the four 2HDM scenarios by setting exclusion limits on their phasespace.

4.1 Monte Carlo and data samples

The simulation and data samples used are listed in this section.

4.1.1 Signal MC samples

As mentioned in Section 1.5 the chosen A mass range which is probed in this analysis is $m_{\mathrm{A}} \in [220, 1000\,\mathrm{GeV}]$. This range is chosen because of the clear dominance of the $A \to Zh$ BR for $m_{\mathrm{A}} < 2m_{\mathrm{top}}$ over other channels, and the still significant sensitivity for $m_{\mathrm{A}} > 2m_{\mathrm{top}}$. Of course searches of $A \to Zh$ for $m_{\mathrm{A}} < 220$ GeV are impossible since the $A \to Zh$ is not kinematically available. Since at masses larger than $2m_{\mathrm{top}}$ the di-top decay becomes kinematically accessible, searches where $m_{\mathrm{A}} > 2m_{\mathrm{top}}$ have a significantly reduced sensitivity. The search is capped at $m_{\mathrm{A}} < 1$ TeV due to the reduced gluon-fusion cross section, $\sigma(\mathrm{pp} \to A)$, as m_A increases. Signal samples for gluon-fusion produced A boson are produced for an array of m_A masses between 220 and 1000 GeV. Separate samples are produced for the different final states, $A \to Zh \to \ell\ell\tau_{had}\tau_{had}$, $A \to Zh \to \ell\ell\tau_{lep}\tau_{had}$ and $A \to Zh \to \ell\ell\tau_{lep}\tau_{lep}$, as well as for $\ell = e, \mu$ and $\ell = \tau$. These samples are produced with Madgraph5 [89], while the hadronization is performed with Pythia8. Table 5 shows the dataset ID numbers for the $A \to Zh \to \ell\ell\tau\tau$ signal samples created in ATLAS.

m_A (GeV)	Dataset ID number					
	$\ell\ell\tau_{had}\tau_{had}$		$\ell\ell\tau_{\ell}\tau_{had}$		$\ell\ell\tau_{\ell}\tau_{\ell}$	
	$\ell = e, \mu$	$\ell = \tau$	$\ell = e, \mu$	$\ell = \tau$	$\ell = e, \mu$	$\ell = \tau$
220	189020	189686	189010	189676	189000	189666
240	189021	189687	189011	189677	189001	189667
260	189022	189688	189012	189678	189002	189668
300	189023	189689	189013	189679	189003	189669
340	189024	189670	189014	189680	189004	189670
350	189025	189671	189015	189681	189005	189671
400	189026	189672	189016	189682	189006	189672
500	189027	189673	189017	189683	189007	189673
800	189028	189674	189018	189684	189008	189674
1000	189029	189675	189019	189685	189009	189675

Table 5: Monte Carlo dataset ID numbers for the gluon-fusion produced signal samples $A \to Zh \to \ell\ell\tau\tau$.

Theoretical cross sections and branching ratios at various scenarios for Type-I and Type-II 2HDMs are summarized in Tables 3–4 in Section 1.5. Benchmark scenarios for each signal sample are chosen in such a way as to maximize the cross section and branching ratio of $gg \to A \to Zh \to \ell\ell\tau\tau$ at the set m_{A}. To define the benchmarks, $m_h = 125$ GeV is chosen. Furthermore the potential parameter is chosen as $m_{12}^2 = m_A^2 \tan\beta/(1 + \tan\beta^2)$ in order to comply with the SM limit, $\sin(\beta - \alpha) \to 1$. For $m_A > 300$ GeV it is required that $m_H = m_A = m_{H^\pm}$, while for $m_A < 300$ GeV, $m_{H^\pm} = 300$ GeV is required. The parameter space is scanned in Type-I, Type-II, Type-III, and Type-IV 2HDMs, excluding the region $\tan\beta < 0.5$ due

to large widths. The scan takes into account the exclusion limits for $A \to Zh$ from the CMS result [34], as well as the ATLAS 2HDM limits from Higgs couplings [36]. The maximum benchmark cross sections times branching ratios chosen are displayed in Table 6. The individual values are dependant on the point on the parameter space chosen, as well as the 2HDM type. The largest value is for the 240 GeV signal point. The decrease going from the 340 GeV to 350 GeV mass points is due to the $t\bar{t}$ kinematic region becoming available, as shown in Figure 7. Since the the branching ratio BR($A \to Zh$) is at a minimum at the 350 GeV mass point, as shown in Figure 7(b), there is an increase from the 350 GeV to 400 GeV mass points, followed by a decrease in $\sigma_A \times \mathrm{BR}_{\ell\ell\tau\tau}$ due to a subsequntly decreasing σ_A .

m_A [GeV]	220	240	260	300	340
$\sigma_A \times \mathrm{BR}_{\ell\ell\tau\tau}$ [pb]	0.02058	0.05808	0.03132	0.0296	0.02139
m_A [GeV]	350	400	500	700	1000
$\sigma_A \times \mathrm{BR}_{\ell\ell\tau\tau}$ [pb]	0.008567	0.01704	0.005452	0.0008027	0.00007691

Table 6: Benchmark cross section times branching ratio values for the $gg \to A \to Zh \to \ell\ell\tau\tau$ signal samples.

4.1.2 Background MC samples

In order to estimate contributions from background processes various MC samples are used. These include MC samples from the following background processes: SM Higgs production associated with a Z-boson; di-boson and tri-boson production, Z-boson plus jets; and single top and di-top production. Background simulation samples were not solely chosen as a result of the final expected background signatures in each channel. Some generators where chosen over others due to better kinematic predictions, as well as larger statistics. The MC background samples used in the analysis are listed in Table 7. The k-factor is the ratio of the NLO to LO cross section for a given process.

4.1.3 Data samples

Events used in this analysis were recorded with all ATLAS sub-systems operational. The data sample used is taken from stable beam proton-proton collisions having an 8 TeV center of mass energy, resulting in a 2012 data sample of $20.3 \pm 0.6\ \mathrm{fb}^{-1}$ (2.8% uncertainty) [90]. The LHC peak instantaneous luminosity of the 2012 data-taking period reached values of up to $7.7 \times 10^{33}\ \mathrm{cm}^{-2}\mathrm{s}^{-1}$, and produced, on average, 35 interactions per bunch crossing. This exceeded its expectations thanks to the large number of protons per bunch. Moreover, the LHC ran with an in-train bunch separation of 50 ns, as opposed to 25 ns, during this time. The high interaction rate gave rise to a large amount of in-time pile-up, attributed to detector signal stemming from other interaction vertices in the bunch crossing. There is also a large amount of out-of-time pile-up (signals coming from neighboring bunch crossings) posing a significant challenge for data analysis. Simulated events are therefore re-weighted using the standard ATLAS pile-up re-weighting tools, to match the distribution of the average number of pile-up interactions $\langle\mu\rangle$ in the data.

4.2 Object Selection

The object definitions for all objects relating to our search topologies are described here. This includes electron, muon and tau lepton candidates, as well as the criteria for jet, E_T^{miss} and di-tau reconstruction. The object selection described here entails a general description which is applicable to all channels.

Process	Dataset ID	Generator	Cross Section [pb]	k-factor	efficiency
SM ZH production					
$ZH(125) \to \tau_{lep}\tau_{lep}$	161675	Pythia8			
$ZH(125) \to \tau_{lep}\tau_{had}$	161686	Pythia8	0.02491976	1	0.456192
$ZH(125) \to \tau_{had}\tau_{had}$	161697	Pythia8	0.02491976	1.0	0.4199
Z + jets					
$Z \to ee$ + Np0	147105	Alpgen	718.97	1.18	1.0
$Z \to ee$ + Np1	147106	Alpgen	175.70	1.18	1.0
$Z \to ee$ + Np2	147107	Alpgen	58.875	1.18	1.0
$Z \to ee$ + Np3	147108	Alpgen	15.636	1.18	1.0
$Z \to ee$ + Np4	147109	Alpgen	4.0116	1.18	1.0
$Z \to ee$ + Np5	147110	Alpgen	1.2592	1.18	1.0
$Z \to \mu\mu$ + Np0	147113	Alpgen	719.16	1.18	1.0
$Z \to \mu\mu$ + Np1	147114	Alpgen	175.74	1.18	1.0
$Z \to \mu\mu$ + Np2	147115	Alpgen	58.882	1.18	1.0
$Z \to \mu\mu$ + Np3	147116	Alpgen	15.673	1.18	1.0
$Z \to \mu\mu$ + Np4	147117	Alpgen	4.0057	1.18	1.0
$Z \to \mu\mu$ + Np5	147118	Alpgen	1.2544	1.18	1.0
$Z \to \tau\tau$ + Np0	147121	Alpgen	719.18	1.18	1.0
$Z \to \tau\tau$ + Np1	147122	Alpgen	175.72	1.18	1.0
$Z \to \tau\tau$ + Np2	147123	Alpgen	58.862	1.18	1.0
$Z \to \tau\tau$ + Np3	147124	Alpgen	15.664	1.18	1.0
$Z \to \tau\tau$ + Np4	147125	Alpgen	4.0121	1.18	1.0
$Z \to \tau\tau$ + Np5	147126	Alpgen	1.2560	1.18	1.0
Di-boson					
WW	105985	Herwig	53.899	1	0.38212
WZ	105987	Herwig	22.258	1	0.30546
$ZZ \to 4e$	126937	Powheg	0.069	1	
$ZZ \to 2e2\mu$	126938	Powheg	0.145	1	
$ZZ \to 2e2\tau$	126939	Powheg	0.102	1	
$ZZ \to 4\mu$	126940	Powheg	0.070	1	
$ZZ \to 2\mu2\tau$	126941	Powheg	0.103	1	
$ZZ \to 4\tau$	126942	Powheg	0.008	1	
Tri-boson					
$WWW^* \to \ell\nu\ell\nu\ell\nu$	167006	MadGraph	0.0051	1.0	1.0
$ZWW^* \to \ell\ell\ell\nu\ell\nu$	167007	MadGraph	0.00155	1.0	1.0
$ZZZ^* \to \nu\nu\ell\ell\ell\ell$	167008	MadGraph	0.00033	1.0	1.0
Single top					
single top: t – channel $W \to e\nu$	117360	AcerMC	9.48	1	1
single top: t – channel $W \to \mu\nu$	117361	AcerMC	9.48	1	1
single top: t – channel $W \to \tau\nu$	117362	AcerMC	9.48	1	1
single top: s – channel $W \to e\nu$	108343	MC@NLO	0.606	1	1
single top: s – channel $W \to \mu\nu$	108344	MC@NLO	0.606	1	1
single top: s – channel $W \to \tau\nu$	108345	MC@NLO	0.606	1	1
single top: Wt – channel	108346	MC@NLO	22.37	1	1
$t\bar{t}$					
$t\bar{t}$(no hadronic)	105200	MC@NLO	238.06	1	0.543
$t\bar{t}$(all hadronic)	105204	MC@NLO	238.06	1	0.457
$t\bar{t}Z$	119355	MadGraph	0.0677	1.34	1.0

Table 7: Details for the simulated background samples that are used in this analysis.

All additional requirements which are specific to either the $\tau_{lep}\tau_{lep}$, $\tau_{lep}\tau_{had}$ and $\tau_{had}\tau_{had}$ channels are described independently in Sections 4.3 and 4.4.

4.2.1 Electrons

Electrons in the ATLAS detector are reconstructed from EM clusters identified the EM calorimeter, which are matched to tracks in the inner detector. Electrons are kinematically required to have transverse momentum $p_{\mathrm{T}} > 7$ GeV, and a pseudorapidity of $|\eta| < 2.47$ (the transition region is excluded, *i.e.* $1.37 < |\eta| < 1.52$). Electron quality and isolation requirements vary with each channel. A complete description of electron identification and reconstruction can be found in Ref. [91].

4.2.2 Muons

Muon reconstruction is driven primarily by the muon spectrometer described in Section 2.2.4. A track emerging from the inner detector and matched to one in the muon spectrometer is considered as a muon candidate. An offline reconstructed transverse momentum of $p_{\mathrm{T}} > 6$ GeV is required of each muon candidate, as well as a pseudorapidity of $|\eta| < 2.5$. Additional isolation and transverse momentum requirements are applied for the different channels.

4.2.3 Jets

Jets are reconstructed using the anti-k_t algorithm [84] with a size parameter of $R = 0.4$ and a $p_{\mathrm{T}} > 20$ GeV for jets with a pseudorapidity of $|\eta| < 2.5$. Jets with a pseudorapidity of $2.5 < |\eta| < 4.5$ are also considered, but require a $p_{\mathrm{T}} > 30$ GeV. Jets in the analysis are used for the calculation of E_T^{miss}, as well as used in overlap removal.

4.2.4 Taus

Reconstruction and identification of the visible product of hadronically decaying taus was explained meticulously in Section 2.4. Tau leptons are selected from jets reconstructed with one or three associated charged tracks. The visible transverse momentum of a tau jet is required to be $p_{\mathrm{T}} > 20$ GeV, with a pseudorapidity of $|\eta| < 2.47$ (2.5) for one track (three track) candidates. Finally as described in Section 2.4.3, BDT algorithms are used to discriminate against jet backgrounds separately for the one- and three-track cases, as well as the different levels of identification tightness. Additional algorithms are used to discriminate against electron and muon fakes.

4.2.5 Missing transverse energy

The total missing transverse momentum, E_T^{miss}, of an event stems from a momentum imbalance in the plane transverse to the beam axis, where momentum conservation is expected, signaling the presence of unseen particles like neutrinos. The momentum imbalance in the transverse plane is obtained from the negative vector sum of the momenta of all calibrated and reconstructed physics objects in the event [92]. This reconstruction includes contributions from energy deposits in the calorimeters and muon spectrometer. The contributions of low p_T particles which do not reach the calorimeters are taken from the tracks found in the ID, while muons reconstructed from the ID are used to recover muons in regions not covered by the muon spectrometer.

4.2.6 Di-tau reconstruction

The di-tau system is reconstructed in all channels using the MMC algorithm described in Section 2.4.4.

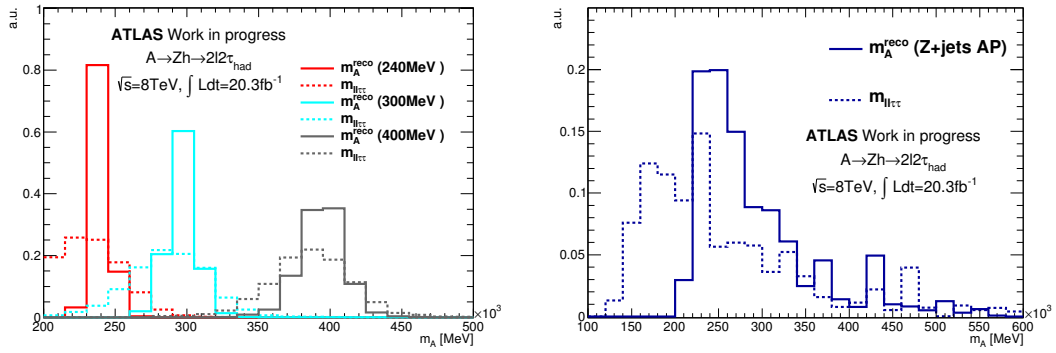
4.2.7 Scaled A mass reconstruction

The final discriminating variable for all three channels is chosen as the scaled reconstructed A boson mass, $m_{\mathrm{A}}^{\mathrm{rec}}$, defined as

$$m_{\mathrm{A}}^{\mathrm{rec}} = m_{\ell\ell\tau\tau} + [m_{\mathrm{Z}}^0 - m_{\ell\ell}] + [m_h^0 - m_{\tau\tau}], \tag{17}$$

where $m_{\ell\ell\tau\tau}$ is the invariant mass of the di-lepton plus di-tau system, the latter of which is reconstructed by the MMC; $m_{\ell\ell}$ is the invariant mass of the di-lepton system; $m_{\tau\tau}$ is the invariant mass of the di-tau system reconstructed by the MMC; m_{Z}^0 is the nominal experimental invariant mass of a Z boson, 91.1 GeV; and m_h^0 is the mass of the measured light Higgs, 125 GeV. This definition of the scaled reconstructed A boson mass offers an improved resolution to the alternate $m_{\ell\ell\tau\tau}$ since it includes the known boson

masses in it's derivation. The mass resolution improvement is seen particularly for lower mass values. Figure 29 shows the improved resolution when using m_A^{rec} in both signal and background MC. The resolution is better for lower mass signals and is dependant on the signal mass considered. Applying a Gaussian fit to the 240 GeV signal distribution histograms yields a mean A mass of $\bar{m}_{\ell\ell\tau\tau} = 228.3$ GeV with a standard deviation of $\sigma_{m_{\ell\ell\tau\tau}} = 25.5$ GeV, while $\bar{m}_A^{\text{rec}} = 239.4$ GeV and $\sigma_{m_{\ell\ell\tau\tau}} = 5.2$ GeV. On the other hand, the same numbers for the 400 GeV signal are $\bar{m}_{\ell\ell\tau\tau} = 386.6$ GeV with a standard deviation of $\sigma_{m_{\ell\ell\tau\tau}} = 27.9$ GeV, while $\bar{m}_A^{\text{rec}} = 394.1$ GeV and $\sigma_{m_{\ell\ell\tau\tau}} = 14.7$ GeV.



(a) (b)

Figure 29: Comparison of the MMC reconstructed $m_{\ell\ell\tau\tau}$ mass and the MMC scaled reconstructed m_A^{rec} mass distributions for different $\tau_{had}\tau_{had}$ (a) signal, and (b) Z+jets samples. The distributions are taken after pre-selection, but without applying the m_A sideband in order to improve statistics.

4.3 Event pre-selection

The preceding object selection in Section 4.2 described general selection criteria intended to provide a good quality selection of the various different objects expected in the desired events. This section describes a further selection which is related to the expected signal topology of the event. Event selection is intended to take into account the signature of the final signal event. By emphasizing characteristics in the signal topology one looks to reduce as much background as possible, while maintaining the signal efficiency as high as possible.

Events in the $\tau_{had}\tau_{had}$ channel are triggered by either of the `EF_e24vhi_medium1`, `EF_mu24i_tight`, `EF_mu36_tight` triggers. These are single lepton triggers in the Event Filter relating to either a single isolated medium electron with $p_{\text{T}} > 24$ GeV, a single tight isolated muon with $p_{\text{T}} > 24$ GeV, or a single tight muon with $p_{\text{T}} > 36$ GeV, respectively. Di-lepton triggers were studied and found to provide a negligible effect on the signal acceptance, thus they are not used. After triggering, events are required to have two same flavor opposite sign light leptons (*i.e.* either e^+e^- or $\mu^+\mu^-$). If triggered by either `EF_e24vhi_medium1` or `EF_mu24i_tight`, at least one of the two leptons must have $p_{\text{T}} > 25$ GeV. On the other hand, if the event is triggered by `EF_mu36_tight`, at least one lepton must have $p_{\text{T}} > 36$ GeV.

In order to take advantage of the fact that the signal region requires two light leptons decaying from a Z boson, sidebands are placed on the invariant mass of the di-lepton system. The di-lepton mass is required to be within the mass window $80 < m_{ll} < 100$ GeV. Different light lepton identification criteria were studied at different mass points and it was found that there is little significance gain from tightening the selection. The ratio of Data/MC in h mass sidebands in a loose-loose (0.80 ± 0.44) and tight-tight (0.85 ± 0.32) showed little difference. This offers a comparison of the QCD contribution of background

in the different regions. It was thus decided that both light leptons were to satisfy a loose++ selection criterion. The light leptons are required to pass both track and calorimeter track isolation requirements. The ptconeXX (etconeXX) of a lepton is the scalar p_{T} (E_{T}) sum of all tracks, baring the lepton track, within a cone of $\Delta R < 0.XX$. Leptons are required to pass a ptcone40/$p_{\mathrm{T}} < 0.2$ and etcone20/$p_{\mathrm{T}} < 0.2$ requirement when separated by $\Delta R > 0.4$. This assures that the lepton tracks are well grouped and separated from other leptons, reassuring lepton quality. In order to avoid rejecting events where lepton pairs are overlapping in their track isolation cones, lepton pairs within $\Delta R < 0.4$ need to pass a reduced track isolation of 0.2 (ptcone20/$p_{\mathrm{T}} < 0.2$ and etcone20/$p_{\mathrm{T}} < 0.2$).

In the $\tau_{had}\tau_{had}$ channel the SM-like h decays into a pair of hadronically decaying taus. The event is therefore required to have an opposite-sign $\tau_{\mathrm{had-vis}}$ pair in addition to the light lepton pair. Each $\tau_{\mathrm{had-vis}}$ satisfies the loose identification criterion. Both $\tau_{\mathrm{had-vis}}$ must also pass the muon and electron vetos, and an invariant mass sideband is placed on the di-tau pair, $75 < m_{\tau\tau} < 175$ GeV, so as to take advantage of the fact that $m_h = 125$ GeV. This also ensures that events where the MMC does not find a solution for $m_{\tau\tau}$ are not considered. The efficiency of the MMC is around 99% for signal and background samples, with the worst of cases being for higher mass signals and the Z+jets background ($\approx 97.8\%$ and $\approx 97\%$ for the 800 GeV signal and Z+jets background samples, respectively). Events passing all of these requirements pass the event pre-selection. The event $\tau_{had}\tau_{had}$ pre-selection is summarised in Table 8.

$\tau_{had}\tau_{had}$ pre-selection			
	Leptons		
Trigger	`EF_e24vhi_medium1`	`EF_mu24i_tight`	`EF_mu36_tight`
2 loose leptons	e^+e^-	$\mu^+\mu^-$	
At least 1 lepton	with $p_{\mathrm{T}} > 25$		with $p_{\mathrm{T}} > 36$
Di-lepton mass	$80 < m_{ll} < 100$ GeV		
Lepton isolation ($\Delta R > 0.4$)	ptcone40/$p_{\mathrm{T}} < 0.2$ and etcone20/$p_{\mathrm{T}} < 0.2$		
($\Delta R < 0.4$)	ptcone20/$p_{\mathrm{T}} < 0.2$ and etcone20/$p_{\mathrm{T}} < 0.2$		
	Taus		
2 loose taus	$\tau^+\tau^-$		
Vetos	Pass electron and muon vetos		
MMC	Must find solution		
Di-lepton mass	$75 < m_{\tau\tau} < 175$ GeV		

Table 8: Event pre-selection requirements for $\tau_{had}\tau_{had}$.

4.4 Event Selection

The full event selection is completed by some additional selection requirements. These include a tighter lower limit on the transverse energy of the leading tau (the tau candidate with highest p_{T} of the pair) $E_T > 35$ GeV. An additional lower limit is applied on the p_{T} of the Z boson, which is parameterized in terms of the final discriminating variable, $m_{\mathrm{A}}^{\mathrm{rec}}$. This limit is defined as $p_{\mathrm{T}}^{Z} > 0.64 \times m_{A}^{\mathrm{rec}} - 131$ GeV and is capped at $m_{A}^{\mathrm{rec}} = 400$ GeV as the extrapolation does not benefit higher masses. Both of these requirements are imposed in order to fully discriminate against background following an optimization study. Their selection is supported in the next Section 4.5. Finally all events with additional light leptons or taus are discarded. This last requirement, as well as the $\tau_{lep}\tau_{lep}$ and $\tau_{lep}\tau_{had}$ equivalent, guaranties that the $\tau_{lep}\tau_{lep}$, $\tau_{lep}\tau_{had}$ and $\tau_{had}\tau_{had}$ analysis are mutually exclusive.

The signal sample acceptance in the $\tau_{had}\tau_{had}$ channel after full event selection is shown in Table 9.

m_A [GeV]	220	240	260	300	340
Acceptance (%)	6.69 ± 0.17	8.33 ± 0.19	8.25 ± 0.19	8.38 ± 0.19	8.66 ± 0.19
m_A [GeV]	350	400	500	800	1000
Acceptance (%)	9.26 ± 0.19	9.52 ± 0.19	12.43 ± 0.22	16.28 ± 0.25	16.33 ± 0.25

Table 9: The signal acceptance and statistical uncertainty for for all simulated signal mass points.

Sample	Pre-selection		Full selection		MMC efficiency
	truth-matched $ll\tau\tau$	Other	truth-matched $ll\tau\tau$	Other	[%]
Z + *jets*	0.0	620 ± 25	0.0	25 ± 4.0	0.97 ± 0.021
WW	0.0	10 ± 3.6	0.0	0.0	N/A ± N/A
ZZ	15.0 ± 0.3	2.2 ± 0.1	4.2 ± 0.1	0.10 ± 0.02	0.99 ± 0.00
WZ	0.0032 ± 0.0032	13.0 ± 1.6	0.0	0.21 ± 0.21	1.0
single top	0.0	1.8 ± 0.8	0.0	0.0	N/A ± N/A
$t\bar{t}$	0.0	0.0	0.0	0.0	N/A ± N/A
SM ZH	1.6 ± 0.0	0.11 ± 0.01	0.88 ± 0.02	0.0054 ± 0.0017	1.0

Table 10: Number of events passing the $\tau_{had}\tau_{had}$ channel selection criteria. Events in which the light leptons are truth-matched to real light leptons with the same flavour and the τ_{had} candidates to true hadronic tau decays are shown separately. The last column, labeled "MMC efficiency", shows the ratio of events that pass the full selection over the number of events that pass the full selection apart from the valid MMC solution requirement. The quoted uncertainties in the numbers reflect the finite number of events in the simulated samples and the data.

The signal acceptance increases with m_A, and flattens out at higher mass points. The flattening of the acceptance at the 1000 GeV mass point is due to a decrease in the acceptance due to boosted leptons failing isolation requirements. The effect of contamination from other signal channels is negligible. Table 10 shows the number of events in the different MC background samples passing the pre-selection and full selection in the $\tau_{had}\tau_{had}$ channel. In addition, the efficiency of the MMC reconstruction algorithm is shown as the fraction of events that pass the full selection, apart from the requirement that there is a valid reconstructed $\tau_{had}\tau_{had}$ MMC mass. Table 10 also indicates the number of events in each MC background that contain truth matched taus, or have misidentified taus. The background in the $\tau_{had}\tau_{had}$ is dominated by events with jets that are misidentified as tau jets. This background is referred to as fake background and is estimated by a data-driven template method, shown in Section 4.6. The remaining irreducible background from true tau jets, primarily ZZ and SM ZH production, are estimated using the simulated samples, and scaled in such a way as to adjust them to the ratio of events that contribute to fake background.

For the $\tau_{lep}\tau_{had}$ analysis events are required to contain exactly three light leptons, eee, $ee\mu$, or $e\mu\mu$, and exactly one hadronic tau jet which must pass the medium tau selection requirement. The leading (sub-leading) electron(s) must have $p_{\mathrm{T}} > 26$ GeV (15 GeV). A leading muon must satisfy a p_{T} requirement of $p_{\mathrm{T}} > 25 - 36$ GeV, depending on the trigger used, while the sub-leading muon must satisfy $p_{\mathrm{T}} > 10$ GeV. The hadronic tau is required to have $p_{\mathrm{T}} > 20$ GeV. The di-lepton pair is chosen to be the pair which yields a mass closest to m_Z^0. The leptons making up the di-lepton pair must be same flavour and opposite charge. Similarly the remaining lepton must be opposite charge to the tau lepton. This lepton is used to reconstruct $m_{\tau\tau}$ using the MMC algorithm. The same m_h and m_Z sidebands defined in the

$\tau_{had}\tau_{had}$ analysis are used. The majority of the background in the $\tau_{lep}\tau_{had}$ channel comes from fake tau background, which is modeled using a data-driven template method identical to the $\tau_{had}\tau_{had}$ case. The remaining true background is comprised of ZZ and SM ZH production, as in the $\tau_{had}\tau_{had}$ case, and is predicted by simulation.

For the $\tau_{lep}\tau_{lep}$ analysis, events with at least four leptons are considered. The four leptons are divided into two same flavour opposite sign pairs. One lepton pair is required to have a mass in the range $80 < m_{\tau\tau} < 100$ GeV, while the other must satisfy a MMC reconstructed mass of $90 < m_{\ell\ell}^{\mathrm{MMC}} < 190$ GeV. The latter mass requirement is related to the $m_h = 125$ GeV mass. It is a slightly relaxed requirement than the $\tau_{had}\tau_{had}$ and $\tau_{lep}\tau_{had}$ equivalent since the MMC has a far poorer $m_{\tau\tau}$ resolution for the $\tau_{lep}\tau_{lep}$ case. Up to one muon reconstructed in the forward region ($2.5 < |\eta| < 2.7$) of the muon spectrometer, or muons identified in the calorimeter with $p_{\mathrm{T}} > 15$ GeV and $|\eta| < 0.1$ are allowed. The leading lepton must satisfy $p_{\mathrm{T}} > 20$ GeV, and the sub-leading (third) lepton must have $p_{\mathrm{T}} > 15$ GeV (10GeV). Where more than one possible combination of leptons satisfying the above requirements is present, the combination minimizing the mass difference with both the Z and h bosons is chosen. The $\tau_{lep}\tau_{lep}$ analysis is subdivided into same flavour (SF), with either four electrons or four muons, and different flavour (DF), with one electron pair and one muon pair, channels. This is done since the backgrounds in the two channels are very different. The final selection of the SF and DF cases is are optimized independently of each other.

4.5 Optimization Study

In order to maximize the signal to background significance in the $\tau_{had}\tau_{had}$ channel, a study is performed to identify variables which discriminate between signal and background effectively at the various signal points. To this end, m_A sidebands were chosen for the optimization related to each signal mass point. A 'rectangular cut' optimization was chosen as it is a transparent and common method for selecting signal events from a mixed signal and background analysis [93]. It involves the calculation of the signal significance while scanning the ranges of a set of chosen kinematic variables. The variables chosen can not be correlated, or must be linearly correlated with each other. The ideal selection would have a large discriminating power with the fewest possible discriminating variables. The ROOT infrastructure is used to conduct the optimization, alongside the TMVA tool [93] which is used for multivariate analysis. It should be noted that the optimization studies where performed in parallel with data-driven background estimation studies (described in Section 4.6). As such, each study influenced the other in their development. Early optimization studies on the tau identification selection of the MC background and signal samples revealed two promising scenarios: either two loosely selected tau leptons (LL), or a medium leading tau and a tight sub-leading tau lepton (MT). Thus template samples estimating the fake background were created for both LL and MT selections. These where used to refine variable optimization as the template method samples provide better statistics than their MC counterparts. It should also be noted that both the pre-selection and event selection looked very different as the optimization developed to the final selection described above. This included different choices in the m_Z and m_h sidebands, lepton p_{T} and isolation requirements, and so forth.

The data-driven background from the template method is combined with true-$\tau_{\mathrm{had-vis}}$ simulated background, and compared to signal points with their respective maximum cross sections. The data-driven background estimate is used due to the low number of simulated events in the dominant background of Z+jets, which made optimization over distributions difficult. Since events with jets misidentified as $\tau_{\mathrm{had-vis}}$ are not expected to be well modeled in simulation, in any case, the decision to use data-driven background estimations for the event selection optimization is further supported. Many different kinematic variables are considered. These include the ΔR separation between lepton and between tau objects,

and the reconstructed boson kinematic variables.

Additional angular distribution studies in the $\tau_{lep}\tau_{lep}$ channel revealed that $\cos\theta^*$ and $\cos\theta_Z$ are two uncorrelated variables that present good separation power against ZZ and fake lepton (Z + jets) backgrounds. Here θ^* is the angle between the decay products (Z and h) and the collision axis in the rest frame, while θ_Z is the angle between the flight direction of the Z boson and it's positive decay product in the Z rest frame. A discriminant function known as the angular discriminant, angularDisc, is built up based on a likelihood ratio of the two aforementioned variables:

$$\text{angularDisc} = \frac{pdf^{\text{S}}}{pdf^{\text{S}} + pdf^{\text{B}}} \tag{18}$$

where pdf^{S} and pdf^{B} are probability density functions obtained by performing a parametric estimation of the $\cos\theta^*$ and $\cos\theta_Z$ distributions for signal and background estimations, respectively. More precisely:

$$pdf^{\text{S}} = pdf^{\text{S}}(\cos\theta_Z) \times pdf^{\text{S}}(\cos\theta^*), \tag{19}$$

and

$$pdf^{\text{B}} = f_{B_{ZZ}} \times pdf^{\text{ZZ}}(\cos\theta_Z) \times pdf^{\text{ZZ}}(\cos\theta^*) + f_{B_{Z+\text{jets}}} \times pdf^{\text{Z+jets}}(\cos\theta_Z) \times pdf^{\text{Z+jets}}(\cos\theta^*), \tag{20}$$

where $f_{B_{ZZ}}$ and $f_{B_{Z+\text{jets}}}$ are the relative fractions of ZZ and Z + jets backgrounds.

Figure 31 shows signal and expected MC background distributions after-preselection for different variables. Figure 31(a) shows the m_A^{rec} distributions. The large peak when transitionong thorugh the 225 GeV bin is a manifestation of the minimum leptonic p_T cuts, reducing statistics in the first bin. As shown in Figure 31(b) and (d), the leading $\tau_{\text{had-vis}}$ E_T and angular discriminant provide good discrimination of background at fixed points after pre-selection. Furthermore, there is a clear dependence of the the reconstructed di-lepton transverse momentum to the signal sample m_A^{rec} mass, providing a m_A^{rec} dependant discriminator. Optimization of these variables is performed by varying each one and finding the points with the largest significance values for different signals. The signal significance, Sig, used is defined as:

$$\text{Sig} = \sqrt{2 \times ((S+B) \times \ln(1 + \frac{S}{B}) - S)}, \tag{21}$$

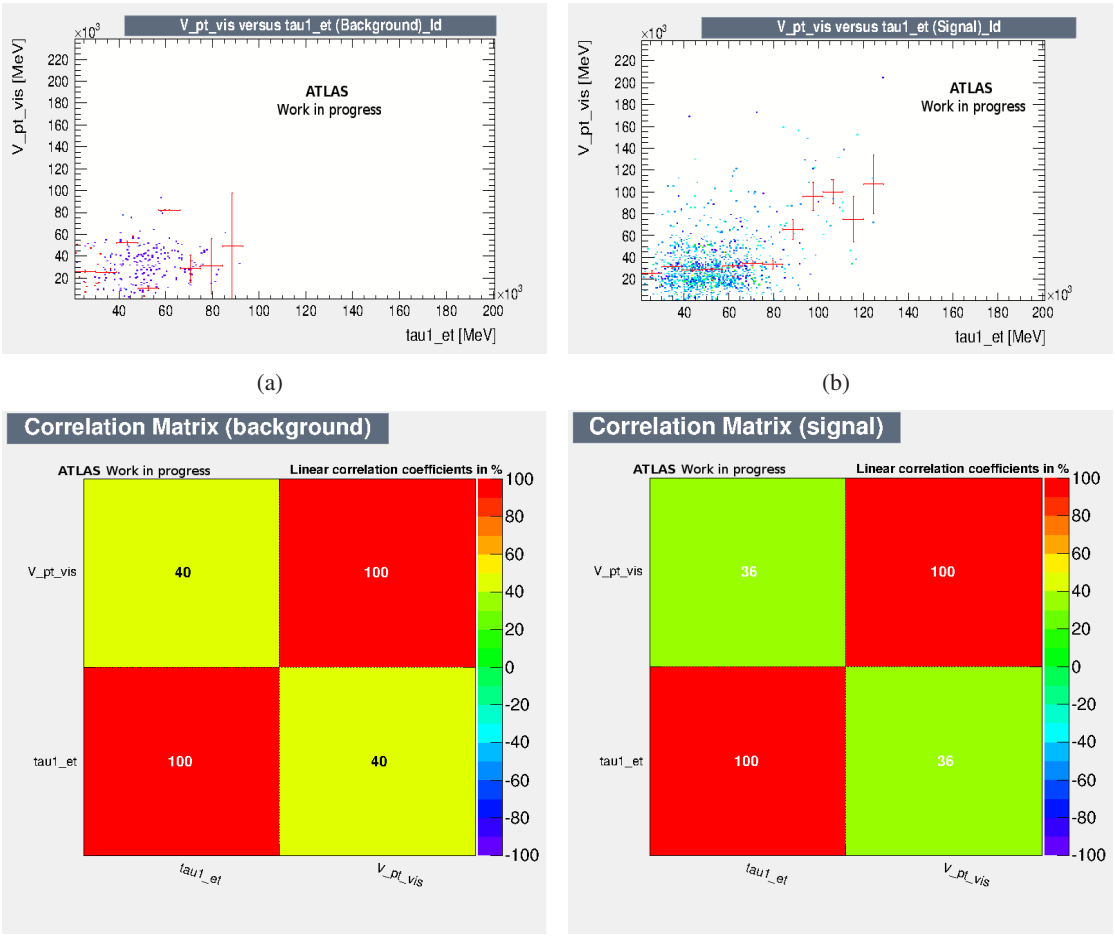
where S and B are the total amount of signal and background events, respectively. This equation gives a better signal significance approximation for low statistic distributions than $\frac{S}{\sqrt{S+B}}$. Two selection criteria are chosen for background discrimination: an A mass dependant p_{T}^Z cut, such that $p_{\text{T}}^Z > 0.64 \times m_A^{rec} - 131$ GeV, and a cut on the leading $\tau_{\text{had-vis}}$ transverse energy, ${E_T}^{\tau} > 35$ GeV. Figure 30 shows two dimensional scatter and linear correlation plots of p_{T}^Z and E_T^{τ} distributions for both signal and combined background samples. The linear correlation coefficient is 100% (−100%) for a perfect positive (negative) linear fit, and 0% for no correlation. The scatter plots show that the variables are randomly clustered and are not correlated. Both the p_{T}^Z and E_T^{τ} distributions are therefore permisable in the optimization study. The p_{T}^Z selection criteria is capped at 400 GeV as the extrapolation does not benefit higher masses. At these higher masses, background is negligible, so an increasing cut would primarily remove signal. Table 11 shows the p_{T}^Z and ${E_T}^{leading\tau}$ points which produce maximum significance.

Tightening the $\tau_{\text{had-vis}}$ identification was also considered, but ultimately rejected. Tightening the $\tau_{\text{had-vis}}$ identification requirement can drastically reduce the background overall, but the reduced number of events in the signal region limits the number of bins which can be used in the final m_A^{rec} histogram, for inputs into limits that rely on the asymptotic approximation. In a test of expected limits, the looser $\tau_{\text{had-vis}}$

identification outperformed the tightened requirements. Table 12 shows a comparison of expected signal and background number of events for loose and medium-tight tau identifications. The final selection distributions are shown in Figure 32.

Signal	V_{pT} [GeV]	$E_T^{leading\tau}$ [GeV]	Total Bkg [weighted events]	Total Signal [weighted events]	Significance
220	4	35.6	34.2	11.9	1.9
240	4	36.8	32.2	42.9	6.4
260	44	35.6	18.4	19.6	4.0
300	76	34.0	7.4	18.4	5.2
340	102	34.0	2.3	13.7	5.9
350	102	34.0	2.3	6.2	3.1
400	102	34.0	2.3	16.1	6.7

Table 11: p_{T}^{V} and $E_T^{leading\tau}$ which produce the largest significance for different signals for $\tau_{had}\tau_{had}$.



(a) (b)

(c) (d)

Figure 30: Scatter plots for the (a) combined background and (b) 220 GeV signal sample of the p_{T}^{Z} and $E_T^{leading\tau}$ variables used in the $\tau_{had}\tau_{had}$ optimization using TMVA. The corresponding linear correlation plots for p_{T}^{Z} and $E_T^{leading\tau}$ are shown for the (c) combined background and (d) 220 GeV signal samples.

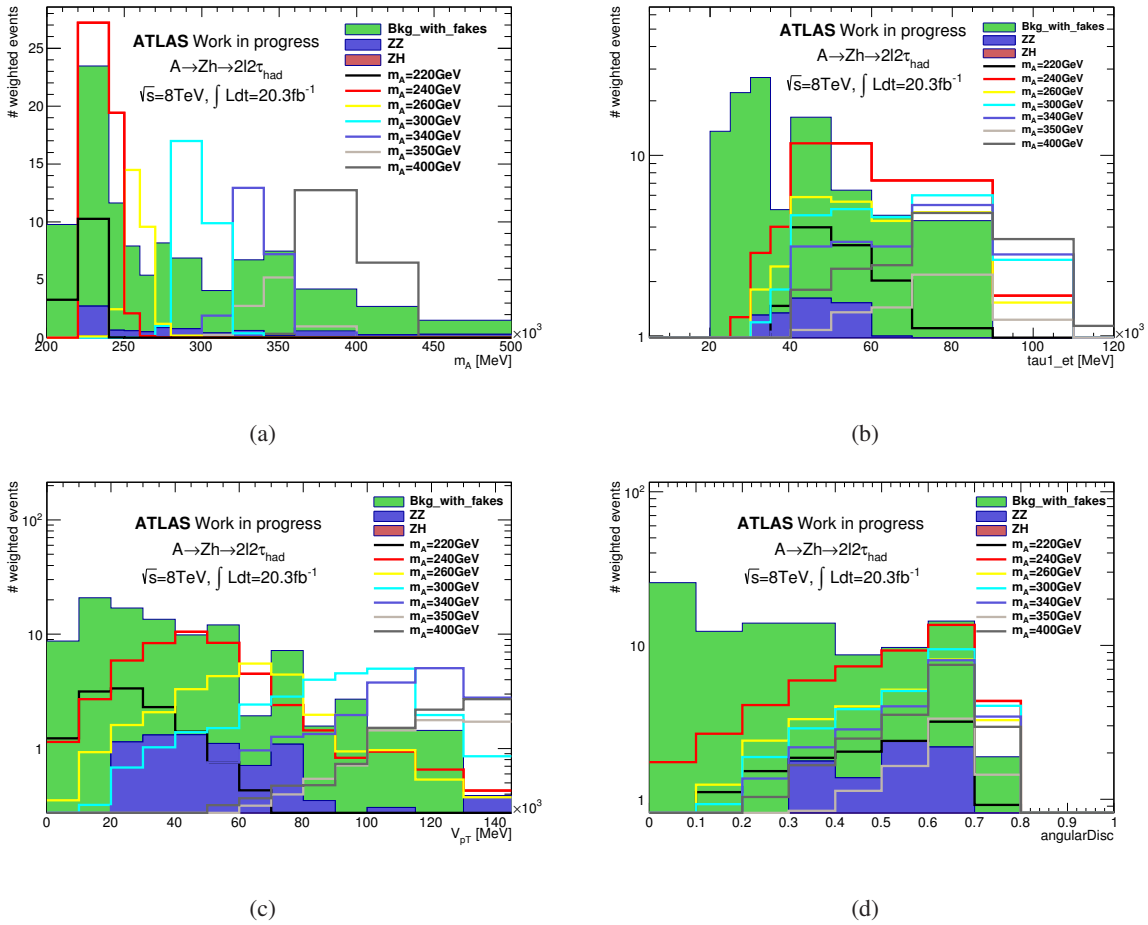


Figure 31: Data-driven background and signal yield comparisons for $\tau_{had}\tau_{had}$ after pre-selection as a function of (a) the reconstructed A boson mass, m_A^{rec}, (b) the leading tau E_T, (c) the di-lepton reconstructed transverse momentum, and (d) the angular discriminant.

4.6 Data-driven background predictions

Two sources of irreducible background dominate in the $\tau_{had}\tau_{had}$ channel. The first is attributed to events which share a final state identical to $\ell\ell\tau_{had}\tau_{had}$. This background is referred to as true background. After the full event selection, true background is dominated exclusively by di-boson ZZ and SM ZH production. Here the on-shell Z decays to $\ell\ell$, while the off-shell Z or SM H decays to $\tau_{had}\tau_{had}$. Alternatively, backgrounds which have signatures which are mis-identified as $\ell\ell\tau_{had}\tau_{had}$ are known as fake background. In the $\tau_{had}\tau_{had}$ channel fake background stems from events with either one or two mis-identified taus which come from jets. Mis-identified leptons play a negligible role in comparison. The background is dominated by $Z+$jets production, where $Z \to \ell\ell$, and the jets are mis-identified as taus. A small contribution also arises from di-boson and top production. Tri-boson and $t\bar{t}Z$ are also considered but produce a negligible background. In order to predict the contribution of the fake background in the $\tau_{had}\tau_{had}$ channel, a data-driven template method is used. The true background plays a far less significant role in the background and is estimated using MC. This section describes the template method prediction.

The main purpose of the template method is to boost the MC prediction of the fake background by using real data events from the detector. This is done by creating a control (template) region, highly

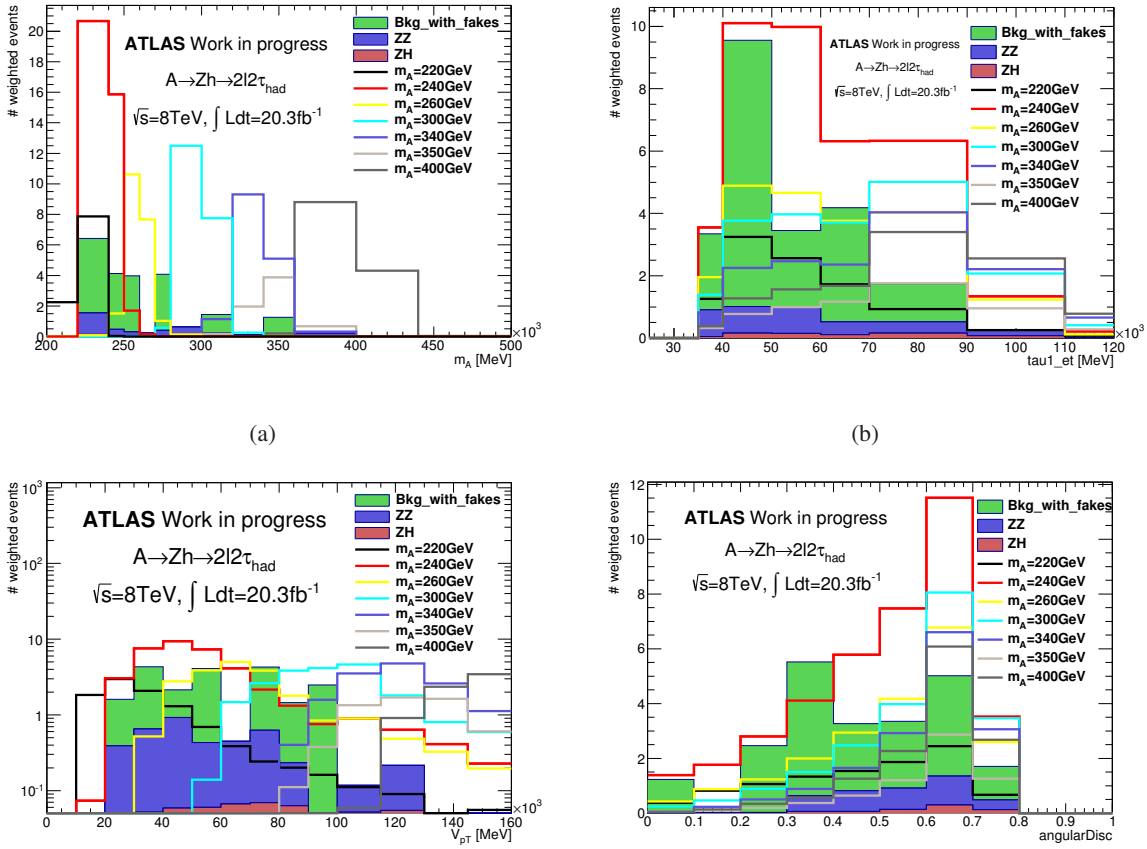


Figure 32: Data-driven background and signal yield comparisons for $\tau_{had}\tau_{had}$ after final selection as a function of (a) the reconstructed A boson mass, m_A^{rec}, (b) the leading tau E_T, (c) the di-lepton reconstructed transverse momentum, and (d) the angular discriminant.

Selection	Background [weighted events]					Signal [weighted events]		
	Fake	ZZ	ZH	Total	eff [ratio]	220 GeV	260 GeV	340 GeV
Loose tau ID								
Pre-selection	91.5 ± 10.6	8.1 ± 1.2	1.0 ± .02	100.6 ± 11.8	1	13.6 ± .3	28.14 ± .5	22.6 ± .4
${E_T}^{tau1}$ cut	30.5 ± 6.1	6.4 ± 1.0	0.9 ± .02	37.8 ± 7.2	.38	12.2 ± .3	25.2 ± .5	21.3 ± .4
${E_T}^{tau1}$,$p_{\mathrm{T}}^{V}(m_A^{rec})$ cut	18.3 ± 4.7	4.1 ± .8	0.8 ± .02	23.2 ± 5.6	.23	10.9 ± .3	21.8 ± .5	16.6 ± .3
Med-Tight tau ID								
Pre-selection	6.0 ± 1.1	5.0 ± .9	0.5 ± .02	11.5 ± 2.1	.11	7.1 ± .2	14.9 ± .4	11.8 ± .3
${E_T}^{tau1}$ cut	2.4 ± 0.7	3.5 ± .8	0.5 ± .02	6.3 ± 1.5	.06	6.4 ± .2	13.4 ± .4	11.1 ± .3
${E_T}^{tau1}$,$p_{\mathrm{T}}^{V}(m_A^{rec})$ cut	1.3 ± .5	2.0 ± .6	0.4 ± .02	3.7 ± 1.1	.04	5.8 ± .2	11.4 ± .3	8.5 ± .2

Table 12: Comparison of different selections applied to loose-loose and medium-tight tau identification in the $\tau_{had}\tau_{had}$.

populated with mis-identified taus, used to model the background in the signal region (Region A). The template region is comprised of three sub control regions. The first control region (Region B) is defined with the full event selection, except that the leading $\tau_{\text{had-vis}}$ is required to fail the loose *tau* identification. The second control region (Region C) is defined with the full event selection, except that the both taus are required to be of the same charge. The third control region (Region D) combines both the inverted loose $\tau_{\text{had-vis}}$ and same charge selection. Table 13 shows the selection requirements for all four regions as defined in the template method for $\tau_{had}\tau_{had}$. The three control regions are each orthogonal to the signal region and highly populated with fake background events. Contamination from both signal and true background in the template region. The shape of the fake background in the template region is used as a prediction of the fake background in the signal region. The template background is scaled in the signal region by using m_h sideband regions. The sideband region is defined as $m_h < 75$ GeV and $m_h > 175$ GeV. The ratio between the background events in the sidebands of the template region and the signal region is used as a scaling factor to normalize the template background in the signal region.

	$\tau\tau$ are opposite charge	$\tau\tau$ are same charge
Pass loose $\tau^{leading}$ selection	**Region A** signal	**Region C** control
Fail loose $\tau^{leading}$ selection	**Region B** control	**Region D** control

Table 13: Representation of the different selection requirements of the signal and three control regions as defined and used in the $\tau_{had}\tau_{had}$ template method.

Two main assumptions are necessary for this method. The first assumption is that the m_{A} shape in the template region describes the m_{A} shape in the signal region accurately. This is tested by comparing the m_A shape of the signal and template regions for MC as well as data in the m_h sidebands. In Figure 33 the final signal region is compared with the total combined background template. Figure 34 shows the comparison of data in the signal region and template regions, both in the m_h sidebands. Data had to be looked at in this way so as to have a blind analysis, where data in the signal region could not be directly looked at until the background predictions and limit setting mechanisms where ready. Both figures show a good agreement of the m_A shape when comparing the signal and template region.

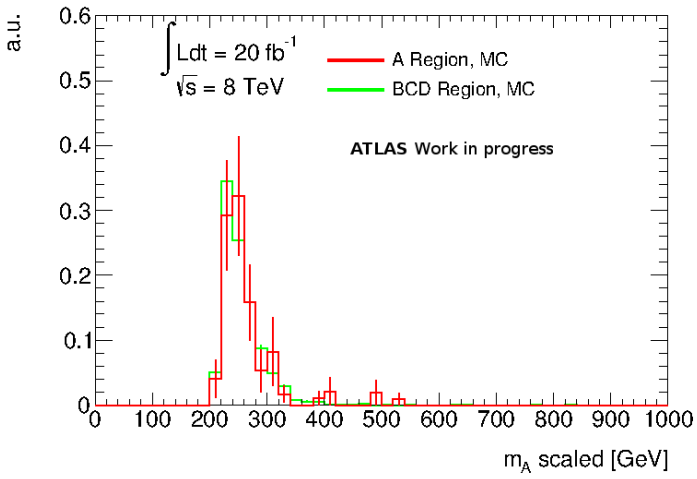


Figure 33: Comparison of the m_A^{rec} distribution for the signal and the combined template regions. Only simulated events with at least one fake $\tau_{\text{had-vis}}$ are shown.

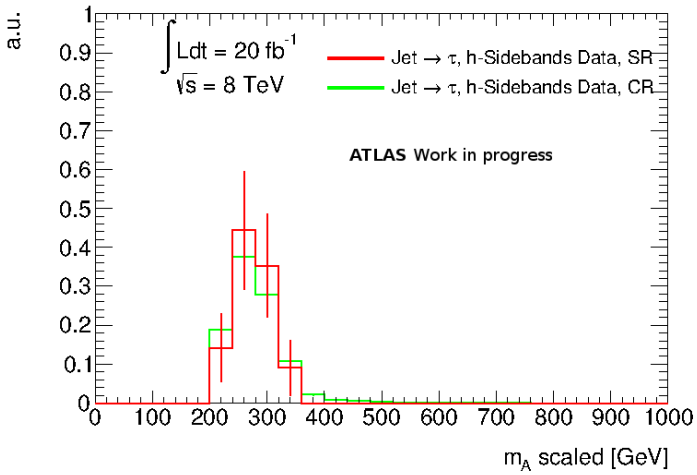


Figure 34: Comparison of the m_A^{rec} distribution in the m_h sideband control region that pass the signal or template region requirements. These distributions are of data events with true $\tau_{\text{had-vis}}$ contributions subtracted using simulation.

The second assumption is that the scale factor attained in the m_h sidebands correctly normalizes the template background in the m_h window. This is tested by looking at the template method background estimation in a m_Z sideband validation region. The validation region is defined as $m_Z < 80$ GeV or $m_Z > 100$ GeV making it orthogonal to the signal region. The number of fake events in the validation region predicted by the template method is 6.3 ± 2.9 (stat.). By passing the ATLAS 2012 data though the same selection required by the validation region, 5.9 data events are observed in this region are , showing that the method predicts the background normalization accurately in the validation region. The systematic uncertainties related to the template method background predictions are described in Section 4.7.

The resulting template background in the $\tau_{had}\tau_{had}$ channel signal region is used as the prediction of all backgrounds which come from mis-identified $\tau_{\text{had-vis}}$. This background is combined with the true background predictions taken directly from simulation to give the final background prediction. The

$\tau_{lep}\tau_{had}$ channel follows a nearly identical template method to predict the background coming from one mis-identified $\tau_{\text{had-vis}}$. The $\tau_{lep}\tau_{lep}$ channel combines both MC and data-driven techniques to predict the fake background which stems from mis-identified leptons.

4.7 Systematic uncertainties

Uncertainties attributed to event prediction, and variable distributions are inherent in any analysis. They are attributed in the $A \rightarrow Zh \rightarrow \ell\ell\tau\tau$ analysis to theoretical and data-driven signal and background predictions, as well as uncertainties in the experiment's measuring capabilities. These uncertainties are known as systematic uncertainties and are described in this section. They must be considered in the final limit setting mechanism.

4.7.1 Experimental and theoretical MC systematics

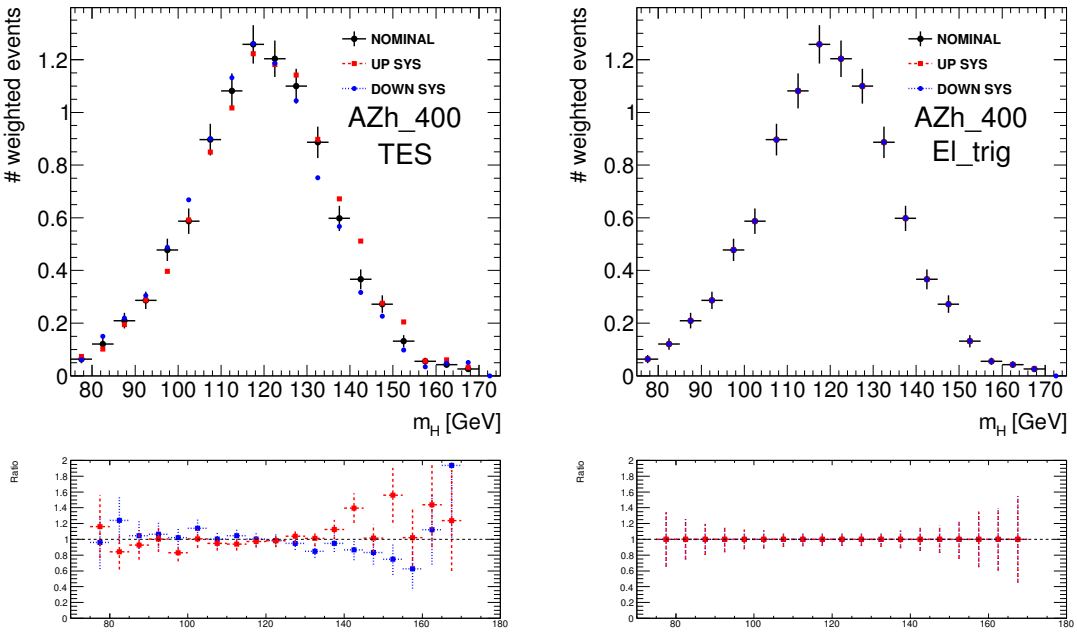
The MC signal and background predictions are susceptible to theoretical uncertainties which are attributed to the choice of PDFs re-normalization and factorization scales, and the choices in α, all of which effects the theoretical normalization. The PDF uncertainty also come from the intrinsic uncertainty due to their determination. On top of this, uncertainties attributed to experimental equipment plays an important part in the uncertainty of the prediction. The dominant detector-related uncertainties in the $A \rightarrow Zh \rightarrow \ell\ell\tau\tau$ analysis are attributed to: the reconstruction and identification of leptons and hadronic taus [86, 94]; the momentum or energy resolution of the reconstructed objects; the reconstruction of E_T^{miss} [92]; the triggering of events; and the measured luminosity. The luminosity uncertainty is taken as 2.8% and serves directly as a scale factor on the event yield [90].

The effect of each systematic uncertainty described above was applied to each MC signal and background that is estimated using MC. The experimental systematic effects on MC signal, as well as true MC backgrounds are evaluated by including the variations from the nominal yields of the above systematic sources. Table 14 shows combined systematic categories which contribute little to no effect when compared to the larger data-driven systematics (Section 4.6) and statistical uncertainties after the full $\tau_{had}\tau_{had}$ selection. The proposed combination of these systemics is the addition in quadrature of individual systematic effects related to: electron (ElID) and muon (MuID) identification, missing transverse energy (MET), jet energy scale (JES), tau energy scale (TES), jet energy resolution (JER) and jet vertex fraction (JVF)[3]. Each experimental uncertainty is also checked for shape variations. Figures 35 and 36 show shape variations from applying different systematic variables for the 400 GeV signal and combined MC background, respectively. The TES systematic shows a slight shape deviation in the m_h distributions in both MC signal and background. This deviation in the shape is however not present in the m_A distribution and does not need to be considered in the limit setting mechanism. The shapes of all other systematic distributions agree well, and no further shape deviation systematic is needed. The total systematic uncertainty on the true background amounts to 8.5%, with the largest contributions coming from TES and tau identification systematics. The largest systematic uncertainty on the true background prediction of the $\tau_{lep}\tau_{had}$ and $\tau_{lep}\tau_{lep}$ channels come from theoretical uncertainties. This amounts to a true background normalization uncertainty of 5.0% in the $\tau_{lep}\tau_{had}$ and 6.4% in the $\tau_{lep}\tau_{lep}$ channels.

[3]JVF is a discriminant which measures the probability that a jet originated from a particular vertex. It allows for the identification and selection of jets originating in the hard-scatter interaction through the use of tracking and vertexing information.

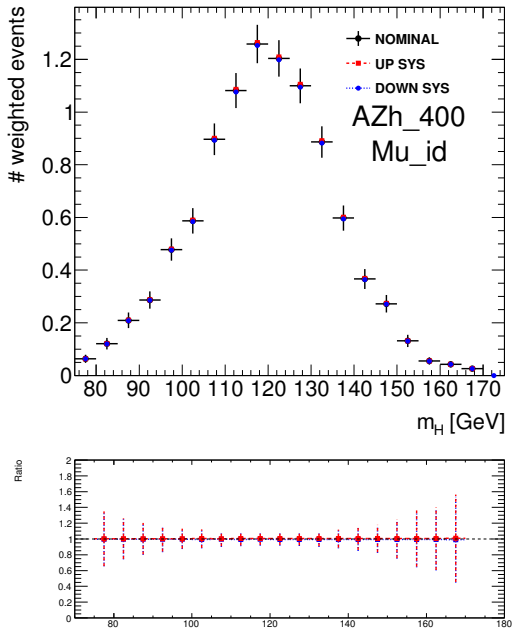
Sample	Total Events [weighted events]	ElID %		MET %		JES %		JER %		JVF %		MuID %		TES %		Stat %
		Up	Down	Up	Down	Up	Down	Up	Down	Up	Down	Up	Down	Up	Down	
True BKG	5.1	4.1	−4.1	0.035	−0.035	0.08	−0.08	7.5e−03	−7.5e−03	9.6e−03	−9.6e−03	0.022	−0.02	0.31	−0.91	2.3
220GeV	10	0.96	−0.78	0.22	−0.22	0.7	−0.54	0.37	−0.37	0	0	0.13	−0.13	0.2	−0.	0.34
240GeV	37	0.23	−0.51	0.3	−0.27	0.35	−0.48	0.36	−0.36	3.7e−03	−3.7e−03	0.029	−0.029	0.6	−0.9	0.3
260GeV	20	0.29	−0.24	0.2	−0.37	0.57	−0.58	0.26	−0.26	3.3e−6	−3.3e−6	0.25	−0.25	0.1	−0.5	0.3
300GeV	20	0.34	−0.33	0.4	−0.4	0.73	−0.76	0.31	−0.31	0	0	0.26	−0.26	0.2	−0.1	0.29
340GeV	15	0.36	−0.38	0.063	−0.16	0.35	−0.28	0.082	−0.082	0.043	−0.043	0.12	−0.12	0.4	−0.7	0.29
350GeV	6.5	0.2	−0.12	0.27	−0.28	0.51	−0.51	0.045	−0.045	0.041	−0.041	0.25	−0.25	0.2	−0.9	0.28
400GeV	13	0.36	−0.36	0.12	−0.17	0.42	−0.39	0.1	−0.1	1.1e−04	−1.1e−04	0.077	−0.077	0.97	−0.	0.27
500GeV	5.6	0.23	−0.23	0.07	−0.07	0.23	−0.23	0.22	−0.22	0	0	0.064	−0.064	0.2	−0.2	0.24
800GeV	1.1	0.36	−0.36	0.093	−0.093	0.17	−0.17	0.049	−0.049	0	0	0.19	−0.19	0.53	−0.97	0.21
1000GeV	0.082	0.23	−0.23	0.44	−0.44	0.62	−0.62	7.3e−05	−7.3e−05	0	0	0.23	−0.23	0.49	−0.34	0.23

Table 14: Table showing the up and down detector systematic fluctuations of the $\tau_{had}\tau_{had}$ MC signal and background samples after full selection, along with the corresponding statistical uncertainty.



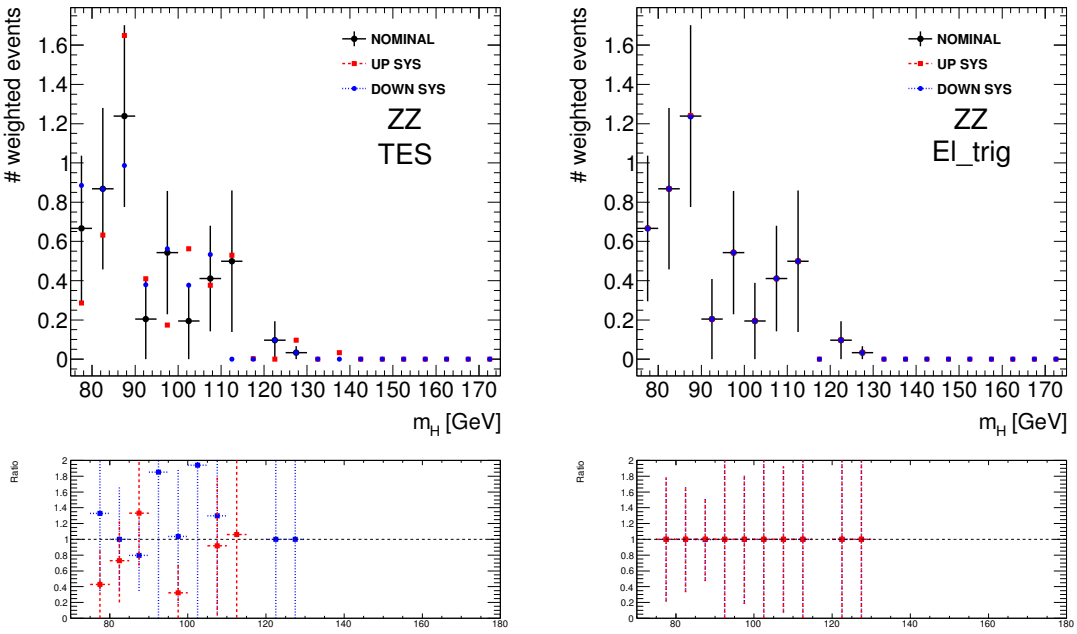
(a)

(b)



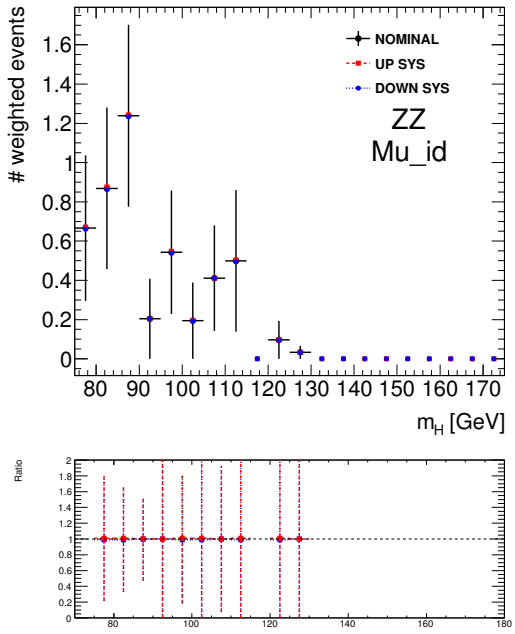
(c)

Figure 35: Up and down experimental systematic deviations of the m_h distribution from the 400 GeV signal nominal distribution. The systematic uncertainties are related to (a) the tau energy scale, (b) electron triggering, and (c) muon identification uncertainties.



(a)

(b)



(c)

Figure 36: Up and down experimental systematic deviations of the m_h distribution from the MC ZZ background nominal distribution. The systematic uncertainties are related to (a) the tau energy scale, (b) electron triggering, and (c) muon identification uncertainties.

4.7.2 Data-driven systematics

Systematic uncertainty in the template method described in Section 4.6 arises from the statistical uncertainty on the normalization factor, as well as from potential differences between the different template

regions. The method is performed with alternate regions in order to evaluate this uncertainty. Four different sub-regions for the background template are defined. Region 1 (R1) has events with two $\tau_{\text{had-vis}}$ of opposite charge, where one fails the loose $\tau_{\text{had-vis}}$ identification. Region two (R2) has events with 2 $\tau_{\text{had-vis}}$ of opposite charge, but both fail the loose $\tau_{\text{had-vis}}$ identification. Region 3 (R3) has events with two $\tau_{\text{had-vis}}$ of the same charge, where one fails the loose $\tau_{\text{had-vis}}$ ID. Region 4 (R4) has events with two same charge $\tau_{\text{had-vis}}$ that fail the loose $\tau_{\text{had-vis}}$ ID. The predictions of the background resulting from each of these template sub-regions and the combined final nominal template are shown in Table 15. The prediction from the sub-regions are consistent with the nominal template prediction. The final fake background yield prediction is 23.2 ± 0.4 (stat.) ± 5 (stat. on normalization factor) ± 2 (sys.). The total errors equal 25% when added in quadrature. The respective $\tau_{lep}\tau_{had}$ systematic uncertainties on the template method amounts to a normalization uncertainty of 38%. The normalization uncertainty for the $\tau_{lep}\tau_{lep}$ fake background predictions amounts to 65% (25%) for the SF (DF) category.

Sample	Norm. factor	Predicted N_{fakes}
Nominal	$(7.8 \pm 1.8) \times 10^{-3}$	$23 \pm 0.4 \pm 5.3$
R1	$(9.6 \pm 2.6) \times 10^{-2}$	$28 \pm 3.4 \pm 7.7$
R2	$(1.8 \pm 0.4) \times 10^{-2}$	$22 \pm 0.6 \pm 5.0$
R3	$(9.4 \pm 3.0) \times 10^{-2}$	$23 \pm 4.8 \pm 7.4$
R4	$(1.9 \pm 0.4) \times 10^{-2}$	$22 \pm 0.7 \pm 5.1$

Table 15: Normalization factors and predicted event yields for various definitions of the template region. The uncertainties quoted here are due to the data statistics and the finite number of generated MC. The uncertainty of the predicted yield that stems from the calculation of the normalization factor is given separately (this is the second quoted error).

4.8 Results

The final $\tau_{had}\tau_{had}$ m_A^{rec} and $m_{\tau\tau}^{\text{MMC}}$ distributions of data and the predicted background and systematic uncertainties after full selection are shown in Figure 37. The results are not represented with the same signal cross sections times branching rations presented in used for the optimization studies, but rather with the values used for in the final combination paper in Reference [88]. The data falls well within the background prediction when considering the full systematic uncertainty. The binning of the m_A^{rec} distribution is the same as that used in the limit setting mechanism described below. Table 16 shows the final event yields for all channels in the $A \to Zh \to \ell\ell\tau\tau$ analysis. The numbers are quoted with their respective statistical and systematic uncertainties. The number of data events in each channel coincide convincingly with the background predictions, within their respective uncertainties, after the full event selections.

Sample	$\ell\ell\tau_{had}\tau_{had}$	$\ell\ell\tau_{lep}\tau_{had}$	$\ell\ell\tau_{lep}\tau_{lep}$ SF	$\ell\ell\tau_{lep}\tau_{lep}$ DF
ZZ	4.2 ± 0.1 ± 0.45	6.97 ± 0.17 ± 0.40	8.60 ± 0.13 ± 0.54	3.98 ± 0.11 ± 0.26
SM ZH	0.88 ± 0.02 ± 0.09	0.85 ± 0.02 ± 0.09	–	–
Others	0.0	0.10 ± 0.01 ± 0.01	0.57 ± 0.15 ± 0.06	0.80 ± 0.20 ± 0.08
Data-driven	23.2 ± 0.4 ± 5.8	9.44 ± 0.76 ± 3.54	0.37 ± 0.12 ± 0.20	2.41 ± 0.52 ± 0.17
Sum	28.3 ± 0.4 ± 5.9	17.4 ± 0.8 ± 3.6	9.54 ± 0.24 ± 0.58	7.19 ± 0.57 ± 0.32
Data	29	18	10	7
Signal	4.5 ± 0.4	5.4 ± 0.4	1.43 ± 0.06	1.90 ± 0.09

Table 16: Final event yields of background predictions and data for all channels in the $A \to Zh \to \ell\ell\tau\tau$ analysis after their respective event selections. Both statistical and total systematic uncertainties are shown. The signal is given for a mass of 300 GeV, and assuming a cross section times branching ratio of 10 fb.

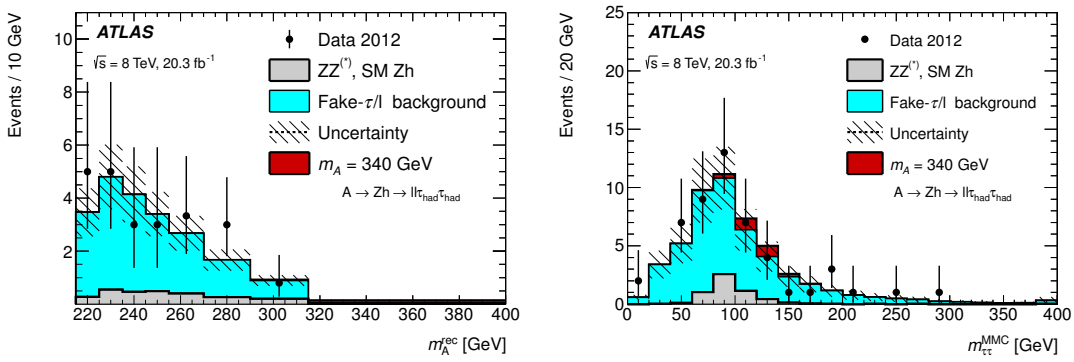


Figure 37: The reconstructed (a) A boson mass, m_A^{rec}, and (b) MMC di-tau mass, $m_{\tau\tau}^{\mathrm{MMC}}$, of the $\tau_{had}\tau_{had}$ channel after full event selection [88]. Events with true $\tau_{\mathrm{had-vis}}$ are taken from MC, while the fake background events are taken from the template method prediction. The 340 GeV signal MC, with an assumed cross section times branching ratio of 50 fb, is plotted for comparison.

Although the final m_A distributions and event yields show excellent agreement with the background predictions, one needs to quantify the the strength with which the background only hypothesis should be chosen. The signal strength, μ, is chosen as the parameter of interest in order to test the hypothesis. It is defined as the ratio of the fitted signal cross section times branching ratio to the predicted signal cross section times branching ratio predicted by our model. The value $\mu = 0$ corresponds to the absence of any signal, whereas the value $\mu = 1$ suggests a good match of the signal as predicted by the theoretical model under study. A binned likelihood function, $\mathcal{L}(\mu, \theta)$, is constructed as the product of Poisson probability terms, serving as an estimator of μ. Here θ denotes the nuisance parameters. The nuisance parameters θ consist of all systematic uncertainties described in Section 4.7. The binned likelihood function is constructed in bins of the reconstructed A boson mass, m_A^{rec}. The bins for the $\tau_{had}\tau_{had}$ channel are chosen as: 0, 225, 235, 245, 255, 270, 290, 315, 2000 [GeV]. The last bin (315 - 2000 GeV) is large since the sensitivity of the analysis drops considerably in this region.

To test a hypothesized value of μ the profile likelihood ratio,

$$\lambda(\mu) = \frac{\mathcal{L}(\mu, \hat{\hat{\theta}})}{\mathcal{L}(\hat{\mu}, \hat{\theta})}, \tag{22}$$

is considered [95]. Here $\hat{\hat{\theta}}$ is the value of θ that maximizes the likelihood function for a specific μ, referred to as conditional maximum-likelihood estimator, and is hence a function of μ. In the denominator, $\hat{\mu}$

and $\hat{\theta}$ are estimators of μ and θ respectively which maximize (unconditionally) the likelihood function. It is furthermore convenient to use the test statistic $t_\mu = -2\ln\lambda(\mu)$ which can be used to calculate the statistical p-value. The particle physics community regards a rejection of the background only hypothesis for p-values less than $p = 2.87 \times 10^{-7}$. This corresponds an excess in signal of more than 5σ. The signal hypothesis is excluded at a threshold p-value of 0.05 (or 1.64σ). For the current analysis we can assume that the presence of a new signal can only increase the mean event rate beyond the background expectation. Therefore t_μ must take into account that $\mu \geq 0$. In light of this a modified frequentist method (a.k.a. CL_s) is used in order to calculate the respective analysis sensitivity in the form of exclusion limits [96]. The test statistic for setting upper limits is denoted as $\tilde{q}_\mu$, and defined as:

$$\tilde{q}_\mu = \begin{cases} -2\ln(\mathcal{L}(\mu,\hat{\hat{\theta}})/\mathcal{L}(0,\hat{\hat{\theta}}_0)) & \text{if } \hat{\mu} < 0 \\ -2\ln(\mathcal{L}(\mu,\hat{\hat{\theta}})/\mathcal{L}(\hat{\mu},\hat{\theta})) & \text{if } 0 \leq \hat{\mu} \leq \mu \\ 0 & \text{if } \hat{\mu} > \mu \end{cases}$$

where $\hat{\hat{\theta}}_0$ is the conditional maximum-likelihood estimator given $\mu = 0$. An asymptotic approximation is assumed in the evaluation of $\tilde{q}_\mu$, while an Asimov data set is used to obtain median significance values [95]. Points within 1σ and 2σ are plotted as bands around the nominal predicted Asimov limit. For every observed value of m_A the test statistic is calculated for all values the cross section times branching ratio. Only values with a CL greater than 95% are selected.

Figure 38 shows the expected and observed upper limits of gluon-fusion $\sigma \times \mathrm{BR}(A \to Zh) \times \mathrm{BR}(h \to \tau\tau)$ for the combined $A \to Zh \to \ell\ell\tau\tau$ analysis. No assumptions are made on the branching ratio of $h \to \tau\tau$ in order to maintain the result model independent. The observed combined upper limit is within 2σ of the expected limit. The expected 95% CL for the $\tau_{lep}\tau_{lep}$, $\tau_{lep}\tau_{had}$ and $\tau_{had}\tau_{had}$ are shown in dashed lines. The drop in the limits at higher values are from the lack of data observed in the highest m_A bins. The 95% CL upper limits on the gluon-fusion $\sigma \times \mathrm{BR}(A \to Zh) \times \mathrm{BR}(h \to \ell\ell\tau\tau)$ range from 0.098–0.013 pb in a range of $220 \leq m_A \leq 1000$ GeV. No excess is observed outside the 2σ. The low observed limits at the higher mass points is caused by a lack of events in the final 315-2000 GeV m_A^{rec} bin.

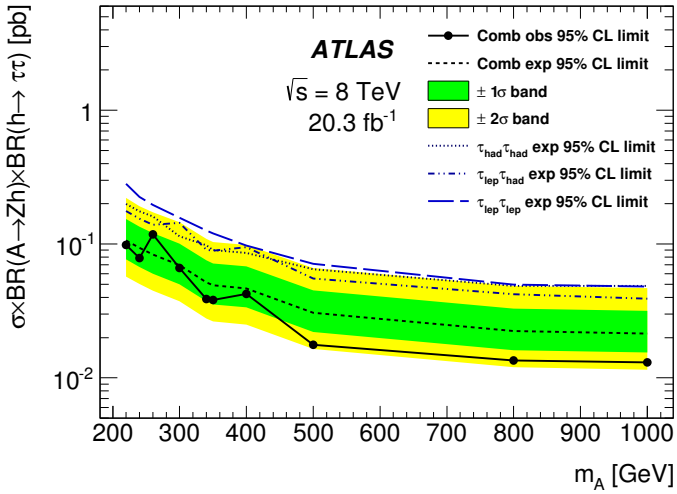


Figure 38: Expected and observed 95% CL upper limits of the gluon-fusion cross section times branching ratio of the combined $A \to Zh \to \ell\ell\tau\tau$ analysis as a function of m_A. Expected limits are represented in dashed lines, while observed limits are in solid lines [88].

In addition to the $A \to Zh$ search with a $h \to \tau\tau$ final state, an $A \to Zh$ search was conducted in-

dependently with a $h \to bb$ final state. Here the Z boson decays as either $Z \to \ell\ell$ or $Z \to \nu\nu$. The $A \to Zh(b\bar{b})$ final state has a larger branching ratio than that of $A \to Zh(\tau\tau)$. However, the $A \to Zh(b\bar{b})$ channel has a large background, while the $A \to Zh(\tau\tau)$ is rather clean. This causes both channels to have roughly the same sensitivity at the low mass region, for m_A masses around 300 GeV. The $A \to Zh(b\bar{b})$ channel has much better sensitivity at the higher mass regions and therefore has finer binning in this area than the $A \to Zh(\tau\tau)$ channel. Figure 39 shows the expected and observed upper limits of gluon-fusion $\sigma \times \mathrm{BR}(A \to Zh) \times \mathrm{BR}(h \to b\bar{b})$ for the $A \to Zh$, $h \to bb$ analysis. Here the limits are model independent since no assumption has been made on the $\mathrm{BR}(h \to b\bar{b})$. The 95% CL upper limits on the gluon-fusion $\sigma \times \mathrm{BR}(A \to Zh) \times \mathrm{BR}(h \to f f b\bar{b})$ range from 0.57–0.014 pb in a range of $220 \leq m_A \leq 1000$ GeV [88].

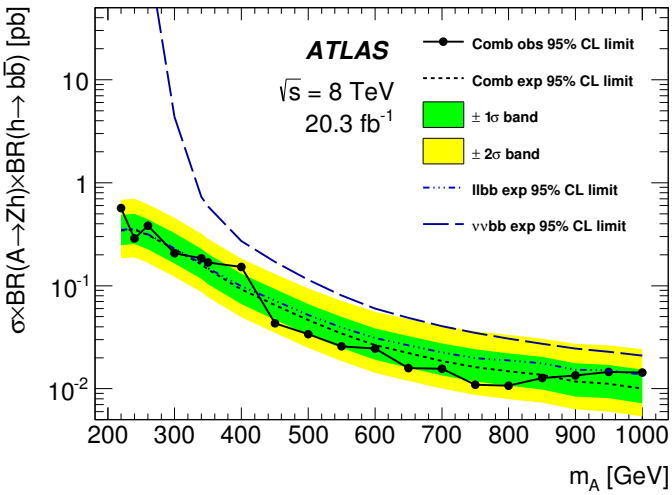


Figure 39: Expected and observed 95% CL upper limits of the gluon-fusion cross section times branching ratio of the combined $A \to Zh$, $h \to b\bar{b}$ analysis as a function of m_{A}. Expected limits are represented in dashed lines, while observed limits are in solid lines [88].

In order to increase the sensitivity of both the $b\bar{b}$ and $\tau\tau$ studies the resulting limits are combined in the context of the CP-conserving 2HDM (Section 1.4), and the results interpreted in a single $A \to Zh$ search [88]. Assumptions as described in Section 1.5, such as $m_{12}^2 = m_A^2 \tan\beta/(1 + \tan^2\beta)$, are made. The limit setting mechanism in both analysis are identical in order to conduct the combination. Common nuisance parameters of the subchannels are correlated and their pull distributions are checked to see if they are treated correctly in the combination. The pull distribution of each nuisance parameter should be close to a standard Gaussian distribution. No deviation from this is seen in any nuisance parameter used in the combination. The branching ratios $\mathrm{BR}(h \to b\bar{b})$ and $\mathrm{BR}(h \to \tau\tau)$ are assumed to take on their SM values. Corrections on the branching ratios are taken into account as they vary as functions of β and α, as shown in Table 2. The combined expected and observed upper limits of gluon-fusion $\sigma \times \mathrm{BR}(A \to Zh)$, assuming the SM branching rations of h to $\tau\tau$ and $b\bar{b}$, are shown in Figure 40.

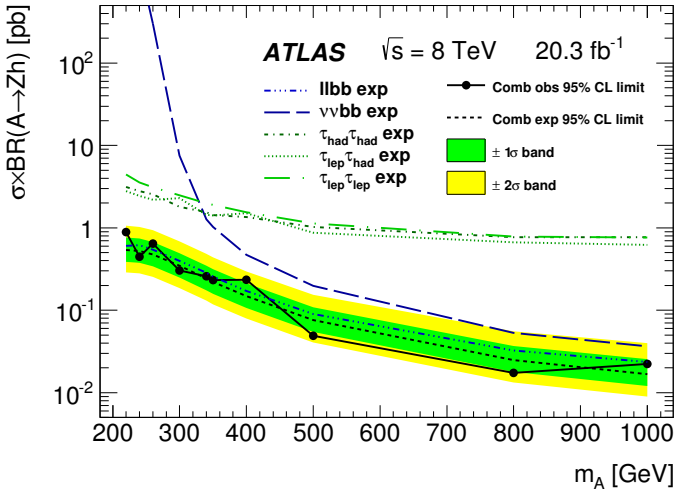
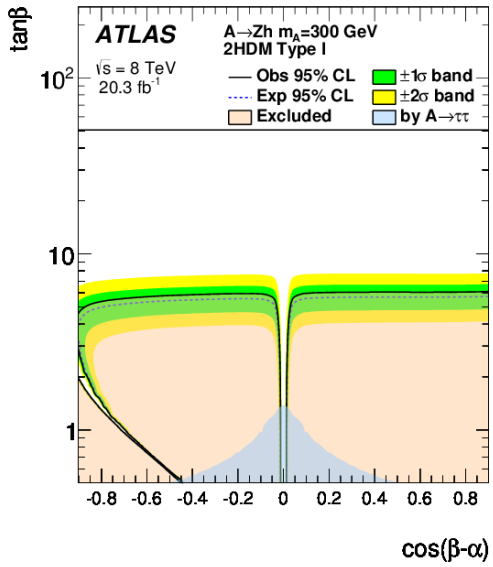
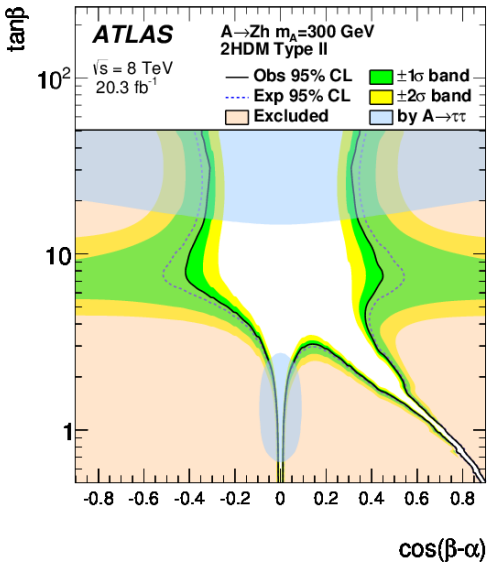


Figure 40: Expected (dashed) and observed (solid) 95% CL upper limits of the gluon-fusion cross section times branching ratio of the combined $A \to Zh$ analysis as a function of m_{A}. The branching ratios of h to $\tau\tau$ and $b\bar{b}$ are taken as the SM values [88].

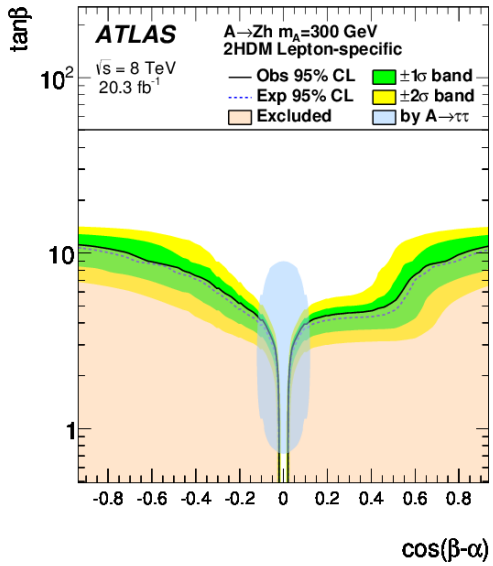
The constrains derived from this combined search are interpreted as exclusion regions in the free parameter phasespace of each of the four 2HDM models considered. For Type-II and Flipped models, where the b-associated production becomes dominant over gluon-fusion at large $\tan\beta$, the b-associated production is included. This is done by deriving the relative efficiencies and the predicted cross section ratio for the b-associated and gluon-fusion production. An empirical matching is used to combine the four-flavour and five-flavour (Figure 6) cross sections in order to derive the b-associated production cross section [97]. The four-flavour scheme cross section is determined as described in Ref. [98, 99], while the five-flavour cross sections are determined using SusHi. The b-associated production efficiencies are estimated from Pythia8 and Sherpa samples. Figure 41 shows the combined $A \to Zh$ interpretation as $(\tan\beta, \cos(\beta-\alpha))$ exclusion regions for the $m_A = 300$ GeV signal point for the four 2HDM scenarios. Large regions within the solid lines are excluded with a 95% CL, where the A boson coming from the specified 2HDM has not been observed. Both gluon-fusion and b-associated production are considered in the Type-II and Flipped models. Alongside the observed exclusion limits are the expected limits with 1σ and 2σ bands. The regions in Type-I and Type-II where no exclusion power is observed, which are at low $\tan\beta$ and far from $\cos(\beta-\alpha) = 0$, are caused by the vanishing branching ratios of $h \to \tau\tau$ and/or $h \to b\bar{b}$. The observed and expected limits agree well in all cases. Results of the $A \to \tau\tau$ analysis are reinterpreted and 95% CL exclusion regions are displayed in light blue for completeness [30]. In many cases the $A \to Zh$ interpretation compliments the regions excluded in the $A \to \tau\tau$ analysis. For all exclusion limits the width of the A boson is assumed to be less that 5% that of m_A. The grey solid areas are regions where the width of the A boson is greater that that 5% that of m_A. The exclusion contours further compliments the CMS exclusion limits placed on Type-I and Type-II modeled in Figure 10 [35]. Finally, Figure 42 shows the combined $A \to Zh$ interpretation as exclusion regions where m_A and $\tan\beta$ are varied and $\cos(\beta-\alpha) = 0.10$. This shows large regions in the (m_A,$\tan\beta$) plane which are excluded for the different 2HDM models. The $A \to Zh$ exclusion regions expand on the reinterpreted $A \to \tau\tau$ results which are plotted in light blue. Figure 43 shows a comparison of the exclusion limits for the bb abd $\tau\tau$ channels in the Lepton-specific and Flipped models. This highlights the importance of the $\tau\tau$ channel in the $A \to Zh$ analysis as it excludes regions which are not accessible in the bb channels.



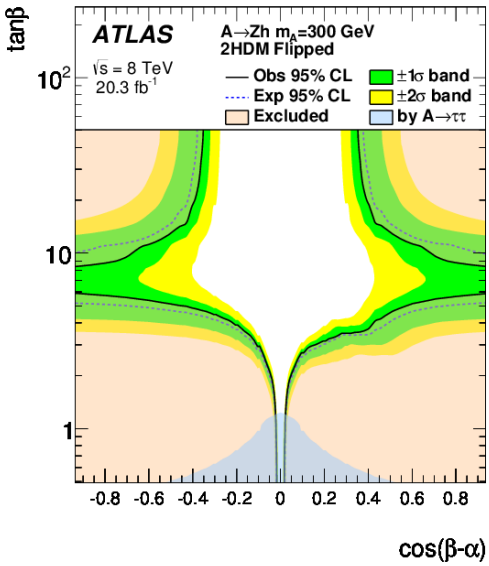
(a) Type-I 2HDM, m_A = 300 GeV



(b) Type-II 2HDM, m_A = 300 GeV

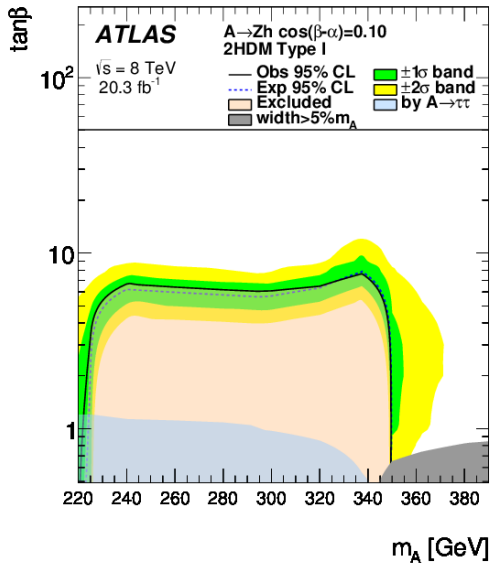


(c) Lepton-specific 2HDM, m_A = 300 GeV

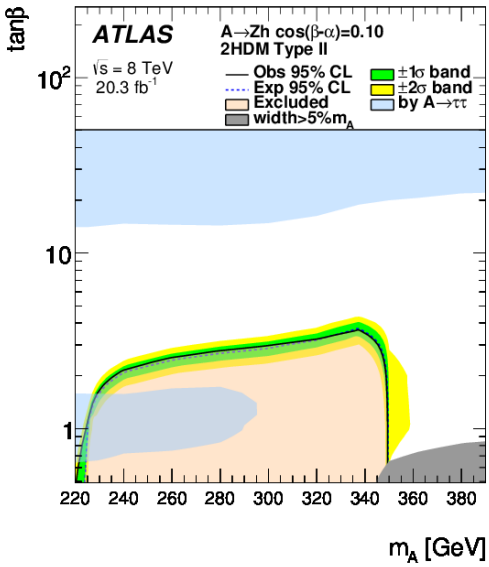


(d) Flipped 2HDM, m_A = 300 GeV

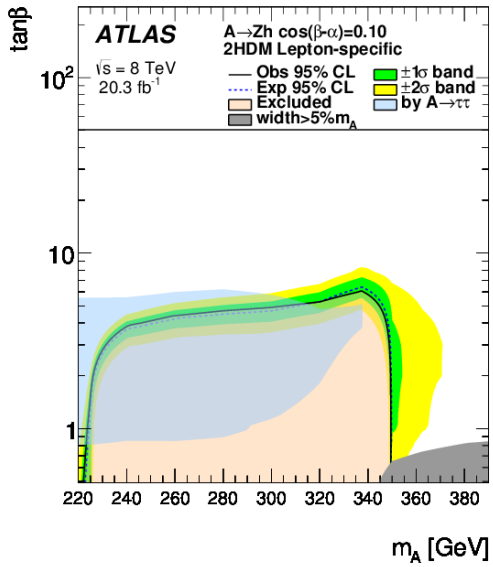
Figure 41: Exclusion plots in the (tanβ, cos($\beta - \alpha$)) plane of the cross section limits in the context of the (a) Type-I, (b) Type-II, (c) Lepton-specific, and (d) Flipped 2HDM types for m_A = 300 GeV. For Type-I and Flipped models the b-associated production has been included along with gluon-fusion. The blue area denotes the excluded regions resulting from reinterpreted constraints on $A \to \tau\tau$ in Ref. [30]. Variations of the natural width up to Γ_A/m_A=5% have been taken into account. The grey solid areas are regions where the width of the A boson is greater that that 5% that of m_A [88].



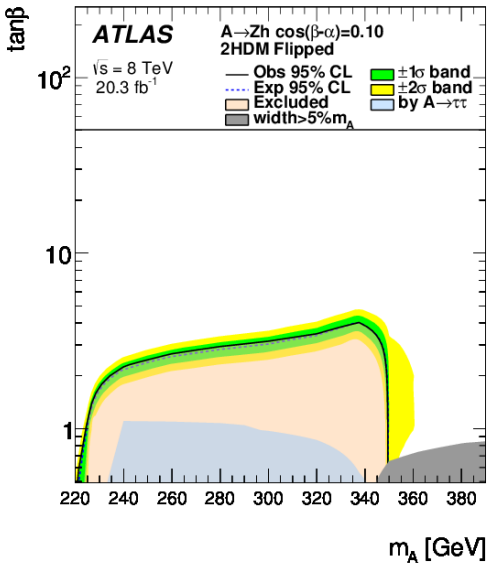
(a) Type-I 2HDM, $\cos(\beta - \alpha) = 0.1$



(b) Type-II 2HDM, $\cos(\beta - \alpha) = 0.1$

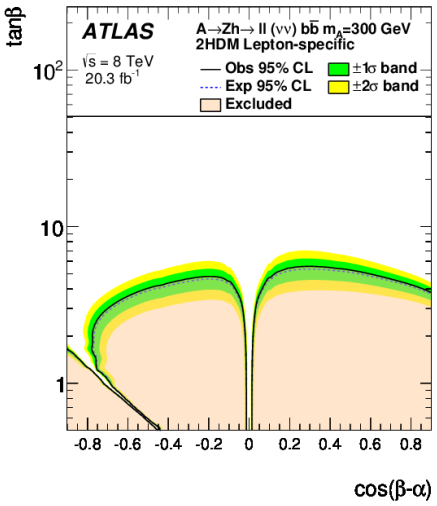


(c) Lepton-specific 2HDM, $\cos(\beta - \alpha) = 0.1$

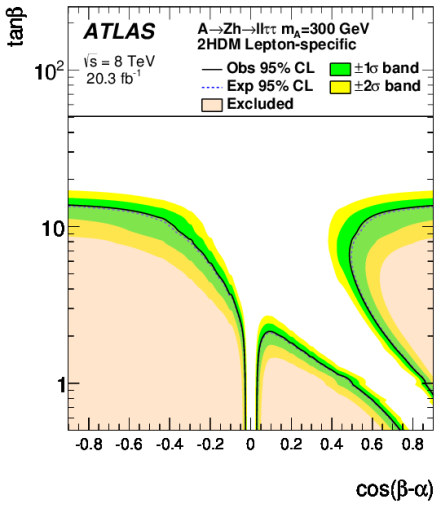


(d) Flipped 2HDM, $\cos(\beta - \alpha) = 0.1$

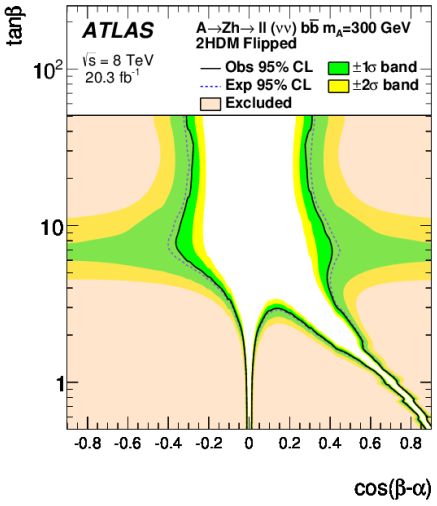
Figure 42: Exclusion plots in the (m_A, $\tan\beta$) plane of the cross section limits in the context of the (a) Type-I, (b) Type-II, (c) Lepton-specific, and (d) Flipped 2HDM types for $\cos(\beta - \alpha) = 0.10$. For Type-I and Flipped models the b-associated production has been included along with gluon-fusion. The blue area denotes the excluded regions resulting from reinterpreted constraints on $A \to \tau\tau$ in Ref. [30]. Variations of the natural width up to Γ_A/m_A=5% have been taken into account. The grey solid areas are regions where the width of the A boson is greater that that 5% that of m_A [88].



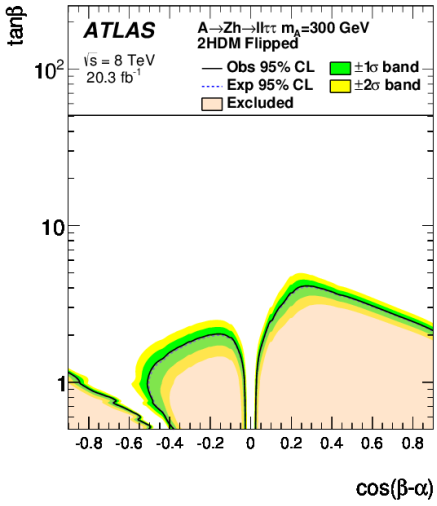
(a) Lepton-specific 2HDM, $A \to Zh \to \ell\ell bb$ and $\nu\nu bb$



(b) Lepton-specific 2HDM, $A \to Zh \to \ell\ell\tau\tau$



(c) Flipped 2HDM, $A \to Zh \to \ell\ell bb$ and $\nu\nu bb$



(d) Flipped 2HDM, $A \to Zh \to \ell\ell\tau\tau$

Figure 43: Exclusion plots in the ($\tan\beta$, $\cos(\beta-\alpha)$) plane of the cross section limits in the context of the (a) and (b) Lepton-specific, and (c) and (d) Flipped 2HDM types for $m_A = 300$ GeV. Variations of the natural width up to Γ_A/m_A=5% have been taken into account. Both the (a) and (c) $A \to Zh \to \ell\ell bb/\nu\nu bb$, and (b) and (d) $A \to Zh \to \ell\ell\tau\tau$ are shown separately to show their individual contributions to the exclusion limits. Variations of the natural width up to Γ_A/m_A=5% have been taken into account. For the interpretation in the Flipped 2HDM, the b-associated production has been included in addition to the gluon fusion [88].

5 Conclusions

A report on the search for a neutral CP-odd A-boson, predicted by 2HDMs, decaying to Zh in proton-proton collisions using the ATLAS detector at the LHC is presented. The final states considered in the search are $Z \to \ell\ell$ and h to either $\tau_{lep}\tau_{lep}$, $\tau_{lep}\tau_{had}$ or $\tau_{had}\tau_{had}$. Focus was placed on the $\tau_{had}\tau_{had}$ analysis where object and event selection, signal optimization techniques, data-driven background estimations, and limit setting mechanisms were described in detail. Where appropriate, mention was made of the respective $\tau_{lep}\tau_{had}$ and $\tau_{had}\tau_{had}$ methodology. Work on the τ_{had} reconstruction MC validation software, which is relevant to the $\tau\tau$ analysis, is also presented. The background predictions of the $A \to Zh \to \ell\ell\tau\tau$ fit the data within systematic and statistical uncertainties. Direct 95% CL upper limits are placed on the gluon-fusion produced $\sigma \times \mathrm{BR}(A \to Zh) \times \mathrm{BR}(h \to \ell\ell\tau\tau)$ for the combined $\tau_{lep}\tau_{lep}$, $\tau_{lep}\tau_{had}$ and $\tau_{had}\tau_{had}$ channels. The direct limits show no indication of an A boson signal above background, and excludes values of 0.098–0.013 pb in a range of $220 \leq m_A \leq 1000$ GeV. The limits are interpreted in a combination with results from the $A \to Zh \to ffb\bar{b}$ analysis, where $f = \nu, \ell$ [88]. The combined limits are calculated with the h branching ratio to $\tau\tau$ and $b\bar{b}$ taken as the SM values. For Type-II and Flipped 2HDMs the b-associated production is taken into acount along with gluon-fusion. The resulting limits are interpreted in four 2HDM models where large sections of phasespace are excluded. The limits from the $A \to Zh \to \ell\ell\tau\tau$ analysis are shown to complement those of $A \to Zh \to ffb\bar{b}$ by excluding regions which are not accesible to the latter analysis. The exclusion plots complement previous A boson searches.

References

[1] A. Bettini, *Introduction to Elementary Particle Physics*. Cambridge University Press, 2008.

[2] G. Gabrielse et al., *New determination of the fine structure constant from the electron g value and QED*, Phys. Rev. Lett. **97** (2006) .

[3] S. L. Glashow, *Partial symmetries of weak interactions*, Phys. Rev. Lett. **22** (1961) .

[4] P. W. Higgs, *Broken Symmetries and the Masses Of Gauge Bosons*, Phys. Rev. Lett. **13** (1964) 508–509.

[5] G. S. Guralnik, C. R. Hagen, and T. W. B. Kibble, *Global Conservation Laws and Massless Particles*, Phys. Rev. Lett. **13** (1964) 585–587.

[6] F. Englert and R. Brout, *Broken Symmetry and the Mass of Gauge Vector Mesons*, Phys. Rev. Lett. **13** (1964) 321–323.

[7] L. lvarez Gaum and J. Ellis, *Eyes on a prize particle*, Nature Physics **7** (2011) 2—3.

[8] Tevatron New Phenomena Higgs Working Group and CDF and D0 Collaboration, G. Bernardi et al., *Combined CDF and D0 Upper Limits on Standard Model Higgs Boson Production at High Mass* $(155 - 200 - GeV/c^{2})$ *with 3* fb^{-1} *of data*, arXiv:0808.0534 [hep-ex].

[9] Tevatron New Physics Higgs Working Group, CDF Collaboration, D0 Collaboration, *Updated Combination of CDF and D0 Searches for Standard Model Higgs Boson Production with up to 10.0* fb^{-1} *of Data*, arXiv:1207.0449 [hep-ex].

[10] ATLAS Collaboration, G. Aad et al., *Expected Performance of the ATLAS Experiment - Detector, Trigger and Physics*, arXiv:0901.0512 [hep-ex].

[11] CMS Collaboration, J. Man et al., *CMS Technical Design Report for the Phase 1 Upgrade of the Hadron Calorimeter*, .

[12] ATLAS Collaboration, *Observation of a new particle in the search for the Standard Model Higgs boson with the ATLAS detector at the LHC*, Phys. Lett. **B 716** (2012) 1–29, arXiv:1207.7214 [hep-ex].

[13] CMS Collaboration, *Observation of a new boson at a mass of 125 GeV with the CMS experiment at the LHC*, Phys. Lett. **B 716** (2012) 30–61, arXiv:1207.7235 [hep-ex].

[14] ATLAS Collaboration, *Measurements of Higgs boson production and couplings in diboson final states with the ATLAS detector at the LHC*, Phys.Lett. B **726** (2013) 88, arXiv:1307.1427 [hep-ex].

[15] CMS Collaboration, *Combination of standard model Higgs boson searches and measurements of the properties of the new boson with a mass near 125 GeV*, Tech. Rep. CMS-PAS-HIG-13-005, CERN, Geneva, 2013.

[16] ATLAS Collaboration, *Evidence for the spin-0 nature of the Higgs boson using ATLAS data*, Phys.Lett. **B726** (2013) 120–144, arXiv:1307.1432 [hep-ex].

[17] CMS Collaboration, S. Chatrchyan et al., *Study of the Mass and Spin-Parity of the Higgs Boson Candidate Via Its Decays to Z Boson Pairs*, Phys.Rev.Lett. **110** (2013) 081803, arXiv:1212.6639 [hep-ex].

[18] ATLAS Collaboration, G. Aad et al., *Evidence for the Higgs-boson Yukawa coupling to tau leptons with the ATLAS detector*, arXiv:1501.04943 [hep-ex].

[19] P. Langacker, *Grand unified theories and proton decays*, Phys.Rev.Lett. **72** (1981) 185–385.

[20] Particle Data Group, J. Beringer et al., *Particle Physics Booklet*, Phys. Rev. **D86, 010001** (2012) .

[21] G. Branco, P. Ferreira, L. Lavoura, M. Rebelo, M. Sher, et al., *Theory and phenomenology of two-Higgs-doublet models*, Phys.Rept. **516** (2012) 1–102, arXiv:1106.0034 [hep-ph].

[22] P. Fayet, *Supersymmetry and Weak, Electromagnetic and Strong Interactions*, Phys.Lett. **B64** (1976) 159.

[23] P. Fayet, *Spontaneously Broken Supersymmetric Theories of Weak, Electromagnetic and Strong Interactions*, Phys.Lett. **B69** (1977) 489.

[24] G. R. Farrar and P. Fayet, *Phenomenology of the Production, Decay, and Detection of New Hadronic States Associated with Supersymmetry*, Phys.Lett. **B76** (1978) 575–579.

[25] P. Fayet, *Relations Between the Masses of the Superpartners of Leptons and Quarks, the Goldstino Couplings and the Neutral Currents*, Phys.Lett. **B84** (1979) 416.

[26] S. Dimopoulos and H. Georgi, *Softly Broken Supersymmetry and SU(5)*, Nucl.Phys. **B193** (1981) 150.

[27] J. E. Kim, *Light Pseudoscalars, Particle Physics and Cosmology*, Phys.Rept. **150** (1987) 1–177.

[28] M. Joyce, T. Prokopec, and N. Turok, *Nonlocal electroweak baryogenesis. Part 2: The Classical regime*, Phys.Rev. **D53** (1996) 2958–2980, arXiv:hep-ph/9410282 [hep-ph].

[29] ATLAS Collaboration, *Beyond-the-Standard-Model Higgs boson searches at a High-Luminosity LHC with ATLAS*, Tech. Rep. ATLAS-PUB-2013-016, CERN, Geneva, 2013.

[30] ATLAS Collaboration, *Search for neutral Higgs bosons of the minimal supersymmetric standard model in pp collisions at $\sqrt{s}$ = 8 TeV with the ATLAS detector*, JHEP **1411** (2014) 056, arXiv:1409.6064 [hep-ex].

[31] M. Baak, M. Goebel, J. Haller, A. Hoecker, D. Ludwig, et al., *Updated Status of the Global Electroweak Fit and Constraints on New Physics*, Eur.Phys.J. **C72** (2012) 2003, arXiv:1107.0975 [hep-ph].

[32] F. Maltoni, G. Ridolfi, and M. Ubiali, *b-initiated processes at the LHC: a reappraisal*, JHEP **1207** (2012) 022, arXiv:1203.6393 [hep-ph].

[33] R. V. Harlander, S. Liebler, and H. Mantler, *SusHi: A program for the calculation of Higgs production in gluon fusion and bottom-quark annihilation in the Standard Model and the MSSM*, Computer Physics Communications **184** (2013) 1605–1617, arXiv:1212.3249 [hep-ph].

[34] CMS Collaboration, *Search for extended Higgs sectors in the H to hh and A to Zh channels in sqrt(s) = 8 TeV pp collisions with multileptons and photons final states*, Tech. Rep. CMS-PAS-HIG-13-025, 2013.

[35] CMS Collaboration, *Search for a pseudoscalar boson A decaying into a Z and an h boson in the llbb final state*, Tech. Rep. CMS-PAS-HIG-14-011, CERN, Geneva, 2014.

[36] ATLAS Collaboration, *Constraints on New Phenomena via Higgs Coupling Measurements with the ATLAS Detector*, Tech. Rep. ATLAS-CONF-2014-010, CERN, Geneva, Mar, 2014.

[37] D. Eriksson, J. Rathsman, and O. Stal, *2HDMC: Two-Higgs-Doublet Model Calculator Physics and Manual*, Comput.Phys.Commun. **181** (2010) 189–205, arXiv:0902.0851 [hep-ph].

[38] L. Evans and P. Bryant, *LHC Machine*, JINST **3** (2008) S08001.

[39] ALICE TPC Collaboration, *The ALICE TPC, a large 3-dimensional tracking device with fast readout for ultra-high multiplicity events*, arXiv:1001.1950v1 [hep-ex].

[40] LHCb Collaboration Tech. Rep. CERN-LHCC-2012-007. LHCb-TDR-12, CERN, Geneva, Apr, 2012.

[41] The TOTEM Collaboration, G. Anelli et al., *The TOTEM experiment at the CERN Large Hadron Collider*, JINST **3** (2008) S08007.

[42] The MoEDAL Collaboration, B. Acharya et al., *The Physics Programme Of The MoEDAL Experiment At The LHC*, Int.J.Mod.Phys. **A29** (2014) 1430050, arXiv:1405.7662 [hep-ph].

[43] The LHCf Collaboration, O. Adriani et al., *The LHCf detector at the CERN Large Hadron Collider*, JINST **3** (2008) S08006.

[44] ATLAS Collaboration, *Expected Performance of the ATLAS Experiment - Detector, Trigger and Physics*, arXiv:0901.0512v4 [hep-ex].

[45] ATLAS Collaboration, *The ATLAS Experiment at the CERN Large Hadron Collider*, JINST **3** (2008) .

[46] ATLAS Collaboration, *Observation of an excess of events in the search for the Standard Model Higgs boson in the $H \to ZZ \to 4l$ channel with the ATLAS detector*, Tech. Rep. ATLAS-CONF-2012-169, CERN, Geneva, Dec, 2012.

[47] D. Griffiths, *Introduction to Electrodynamics*. Pearson Benjamin Cummings, 2008.

[48] CERN, *ATLAS: Detector and physics performance technical design report. Volume 1*, Tech. Rep. CERN-LHCC-99-14, ATLAS-TDR-14, 1999.

[49] ATLAS Collaboration, *ATLAS Images*, `http://atlas.ch/photos/index.html`. [Online; accessed 2-October-2014].

[50] S. C. Loken, ed., *Proceedings of the International Workshop on Semiconductor Pixel Detectors for Particles and X-Rays*. Lawrence Berkeley Nat. Lab., Berkeley, CA, 2002.

[51] M. Garcia-Sciveres, *The ATLAS Pixel Detector*, in Loken [50].

[52] I. Goitom, *The Electromagnetic Calorimeter*, `http://mathsconcepts.com/node18.html`. [Online; accessed 2-October-2014].

[53] ATLAS Collaboration, *ATLAS computing: Technical Design Report*, Tech. Rep. ATLAS TDR-017; CERN-LHCC-2005-022, CERN, 2005.

[54] I. Bird, P. Buncic, F. Carminati, M. Cattaneo, P. Clarke, I. Fisk, M. Girone, J. Harvey, B. Kersevan, P. Mato, R. Mount, and B. Panzer-Steindel, *Update of the Computing Models of the WLCG and the LHC Experiments*, Tech. Rep. CERN-LHCC-2014-014. LCG-TDR-002, CERN, Geneva, Apr, 2014.

[55] M. Werlen, ed., *New computing techniques in physics research V. Proceedings, 5th International Workshop, AIHENP '96, Lausanne, Switzerland*. 1997.

[56] R. Brun and F. Rademakers, *ROOT - An Object Oriented Data Analysis Framework*, in Werlen [55].

[57] A. Aimar, ed., *Computing in high energy physics and nuclear physics. Proceedings, Conference, CHEP'04, Interlaken, Switzerland, September 27-October 1 2004*, no. CERN-2005-002. 2005.

[58] P. Calafiura, W. Lavrijsen, C. Leggett, M. Marino, and D. Quarrie, *The Athena Control Framework in Production, New Developments and Lessons Learned*, in Aimar [57].

[59] ATLAS Collaboration, *The ATLAS Computing Workbook*, `https://twiki.cern.ch/twiki/bin/view/AtlasComputing/WorkBook?redirectedfrom=Atlas.WorkBook`. [Online; accessed 7-October-2014].

[60] ATLAS Collaboration, *The ATLAS Simulation Infrastructure*, Eur. Phys. J. C **70** (2010) 823, `arXiv:physics.ins-det/1005.4568`.

[61] T. Sjostrand, S. Mrenna, and P. Z. Skands, *PYTHIA 6.4 Physics and Manual*, JHEP **0605** (2006) 026, `arXiv:hep-ph/0603175 [hep-ph]`.

[62] M. Smizanska, S. P. Baranov, J. Hrivnc, and E. Kneringer, *Overview of Monte Carlo simulations for ATLAS B-physics in the period 1996-1999*, Tech. Rep. ATL-PHYS-2000-025. ATL-COM-PHYS-99-042, CERN, Geneva, 2000.

[63] G. Corcella, I. Knowles, G. Marchesini, S. Moretti, K. Odagiri, et al., *HERWIG 6: An Event generator for hadron emission reactions with interfering gluons (including supersymmetric processes)*, JHEP **0101** (2001) 010, arXiv:hep-ph/0011363 [hep-ph].

[64] T. Gleisberg et al., *Event generation with SHERPA 1.1*, JHEP **02** (2009) 007.

[65] M. Gyulassy and X.-N. Wang, *HIJING 1.0: A Monte Carlo program for parton and particle production in high-energy hadronic and nuclear collisions*, Comput.Phys.Commun. **83** (1994) 307, arXiv:nucl-th/9502021 [nucl-th].

[66] M. L. Mangano, M. Moretti, F. Piccinini, R. Pittau, and A. D. Polosa, *ALPGEN, a generator for hard multiparton processes in hadronic collisions*, JHEP **0307** (2003) 001, arXiv:hep-ph/0206293 [hep-ph].

[67] S. Frixione and B. R. Webber, *Matching NLO QCD computations and parton shower simulations*, JHEP **0206** (2002) 029, arXiv:hep-ph/0204244 [hep-ph].

[68] B. P. Kersevan and E. Richter-Was, *The Monte Carlo event generator AcerMC version 2.0 with interfaces to PYTHIA 6.2 and HERWIG 6.5*, arXiv:hep-ph/0405247.

[69] S. Jadach, Z. Was, R. Decker, and J. H. Kuhn, *The tau decay library TAUOLA: Version 2.4*, Comput.Phys.Commun. **76** (1993) 361–380.

[70] E. Barberio and Z. Was, *PHOTOS: A Universal Monte Carlo for QED radiative corrections. Version 2.0*, Comput.Phys.Commun. **79** (1994) 291–308.

[71] D. Lange, *The EvtGen particle decay simulation package*, Nucl.Instrum.Meth. **A462** (2001) 152–155.

[72] T. Sjostrand, S. Mrenna, and P. Z. Skands, *A Brief Introduction to PYTHIA 8.1*, Comput.Phys.Commun. **178** (2008) 852–867, arXiv:0710.3820 [hep-ph].

[73] M. Bahr, S. Gieseke, M. Gigg, D. Grellscheid, K. Hamilton, et al., *Herwig++ Physics and Manual*, Eur.Phys.J. **C58** (2008) 639–707, arXiv:0803.0883 [hep-ph].

[74] GEANT4 Collaboration, S. Agostinelli et al., *GEANT4: A Simulation toolkit*, Nucl.Instrum.Meth. **A506** (2003) 250–303.

[75] I. Pshenichnov, I. Mishustin, , and W. Greiner, *Comparative study of depthdose distributions for beams of lightand heavy nuclei in tissue-like media*, Nucl.Instrum.Meth **B 266** (2008) 1094–1098.

[76] R. Freudenberg, M. Wendisch, and J. Kotzerke, *Geant4-Simulations for cellular dosimetry in nuclear medicine*, Z. Med. Phys. **21** (2010) 281–289.

[77] ATLAS Collaboration, *Search for the Standard Model Higgs boson in the H to $\tau^+\tau^-$ decay mode in $\sqrt{s}$ = 7 TeV pp collisions with ATLAS*, JHEP **1209** (2012) 070, arXiv:1206.5971 [hep-ex].

[78] ATLAS Collaboration, *Search for charged Higgs bosons decaying via $H^+ \to \tau\nu$ in top quark pair events using pp collision data at $\sqrt{s}$ = 7 TeV with the ATLAS detector*, JHEP **1206** (2012) 039, arXiv:1204.2760 [hep-ex].

[79] R. Reece and H. H. Williams, *A search for new physics in high-mass ditau events in the ATLAS detector*. PhD thesis, Pennsylvania U., Jul, 2013. Presented 12 Jun 2013.

[80] Y. Sakurai, *The ATLAS Tau Trigger Performance during LHC Run 1 and Prospects for Run 2*, arXiv:1409.2699 [hep-ex].

[81] M. Heldmann and D. Cavalli, *An improved tau-Identification for the ATLAS experiment*, Tech. Rep. ATL-PHYS-PUB-2006-008, ATL-COM-PHYS-2006-010, 2005.

[82] E. Richter-Was and T. Szymocha, *Hadronic tau identification with track based approach*, Tech. Rep. ATL-PHYS-PUB-2005-005, ATL-COM-PHYS-2004-080, 2004.

[83] ATLAS Collaboration, *Identification of the Hadronic Decays of Tau Leptons in 2012 Data with the ATLAS Detector*, Tech. Rep. ATLAS-CONF-2013-064, CERN, Geneva, Jul, 2013.

[84] M. Cacciari, G. P. Salam, and G. Soyez, *The Anti-k(t) jet clustering algorithm*, JHEP **0804** (2008) 063, arXiv:0802.1189 [hep-ph].

[85] W. Lampl, S. Laplace, D. Lelas, P. Loch, H. Ma, S. Menke, S. Rajagopalan, D. Rousseau, S. Snyder, and G. Unal, *Calorimeter Clustering Algorithms: Description and Performance*, Tech. Rep. ATL-LARG-PUB-2008-002. ATL-COM-LARG-2008-003, CERN, Geneva, Apr, 2008.

[86] ATLAS Collaboration, *Performance of the Reconstruction and Identification of Hadronic Tau Decays in ATLAS with 2011 Data*, Tech. Rep. ATLAS-CONF-2012-142, CERN, Geneva, Oct, 2012.

[87] A. Elagin, P. Murat, A. Pranko, and A. Safonov, *A New Mass Reconstruction Technique for Resonances Decaying to di-tau*, arXiv:1012.4686 [hep-ex].

[88] ATLAS Collaboration, G. Aad et al., *Search for a CP-odd Higgs boson decaying to Zh in pp collisions at $\sqrt{s} = 8$ TeV with the ATLAS detector*, arXiv:1502.04478 [hep-ex].

[89] J. Alwall, M. Herquet, F. Maltoni, O. Mattelaer, and T. Stelzer, *MadGraph 5 : Going Beyond*, JHEP **1106** (2011) 128, arXiv:1106.0522 [hep-ph].

[90] ATLAS Collaboration, *Improved luminosity determination in pp collisions at $\sqrt{s} = 7$ TeV using the ATLAS detector at the LHC*, arXiv:1302.4393 [hep-ex].

[91] ATLAS Collaboration, *Electron reconstruction and identification efficiency measurements with the ATLAS detector using the 2011 LHC proton-proton collision data*, Eur.Phys.J. **C74** (2014) no. 7, 2941, arXiv:1404.2240 [hep-ex].

[92] ATLAS Collaboration, *Performance of Missing Transverse Momentum Reconstruction in Proton-Proton Collisions at 7 TeV with ATLAS*, Eur.Phys.J. **C72** (2012) 1844, arXiv:1108.5602 [hep-ex].

[93] A. Hoecker et al., *TMVA - Toolkit for Multivariate Data Analysis*, arXiv:0703039v5 [physics.data-an].

[94] ATLAS Collaboration, *Determination of the tau energy scale and the associated systematic uncertainty in proton-proton collisions at $\sqrt{s} = 8$ TeV with the ATLAS detector at the LHC in 2012*, Tech. Rep. ATLAS-CONF-2013-044, CERN, Geneva, Apr, 2013.

[95] G. Cowan, K. Cranmer, E. Gross and O. Vitells, *Asymptotic formulae for likelihood-based tests of new physics*, Eur.Phys.J. **C71** (2011) 1554, arXiv:1007.1727 [physics.data-an].

[96] A. L. Read, *Presentation of search results: the CL_s technique*, J.Phys. **G28** (2002) 2693–2704.

[97] R. Harlander, M. Kramer, and M. Schumacher, *Bottom-quark associated Higgs-boson production: reconciling the four- and five-flavour scheme approach*, arXiv:1112.3478 [hep-ph].

[98] S. Dawson, C. Jackson, L. Reina, and D. Wackeroth, *Exclusive Higgs boson production with bottom quarks at hadron colliders*, Phys.Rev. **D69** (2004) 074027, arXiv:hep-ph/0311067 [hep-ph].

[99] S. Dittmaier et al., *Higgs radiation off bottom quarks at the Tevatron and the CERN LHC*, Phys.Rev. **D70** (2004) 074010, arXiv:hep-ph/0309204 [hep-ph].